FINAL REPORT

Project Title: U_3Si_2 Fabrication and Testing for Implementation into the BISON Fuel Performance Code

Principal Investigator: Dr. Travis W. Knight, Professor and Director, Nuclear Engineering, University of South Carolina, 300 Main Street, Columbia, SC 29208; 803-777-1465, twknight@sc.edu

Co-PI: Dr. Xinyu Huang (USC), Dr. Elwyn Roberts (USC), Dr. Jason Harp (INL), Dr. Mitch Meyer (INL)

Institution: University of South Carolina (USC)

Collaborators: Idaho National Laboratory (INL)

Workscope: FC-2.2

PICSNE Workpackage #: Project13-5346

Contract: DE-NE0000725

Table of Contents:

Acknowledgement

This research was performed using funding received from the DOE Office of Nuclear Energy's Nuclear Energy University Programs.

This work produced one dissertation and three Master's theses and supported research of four graduate students, Kathryn Metzger, Ray Austin Freeman, Coleman Terrapin, and Emil Mercado.

The samples used in this work were expertly prepared and fabricated at Idaho National Laboratory by Rita Hoggan, Adrian Wagner, and Michael Chapple.

1. Objectives and Milestones

- A creep test stand was designed and constructed for compressive creep testing of U_3Si_2 pellets. This is described in Chapter 3.
- Creep testing of U_3Si_2 pellets was completed. In total, 13 compressive creep tests of U_3Si_2 pellets was successfully completed. This is reported in Chapter 3.
- Secondary creep model of U_3Si_2 was developed and implemented in BISON. This is described in Chapter 4.
- Properties of U_3Si_2 were implemented in BISON. This is described in Chapter 4.
- A resonant frequency and damping analyzer (RFDA) using impulse excitation technique (IET) was setup, tested, and used to analyze U_3Si_2 samples to measure Young's and Shear Moduli which were then used to calculate the Poisson ratio for U_3Si_2. This is described in Chapter 5.
- Characterization of U_3Si_2 samples was completed. Samples were prepared and analyzed by XRD, SEM, and optical microscopy. Grain size analysis was conducted on images. SEM with EDS was used to analyze second phase precipitates. Impulse excitation technique was used to determine the Young's and Shear Moduli of a tile specimen which allowed for the determination of the Poisson ratio. Helium pycnometry and mercury intrusion porosimetry was performed and used with image analysis to determine porosity size distribution. Vickers microindentation characterization method was used to evaluate the mechanical properties of U_3Si_2 including toughness, hardness, and Vickers hardness. Electrical resistivity measurement was done using the four-point probe method. This is reported in Chapter 5.

2. Publications

For this work, one journal publication, two conference papers, three theses, and one dissertation has been produced. In addition, at the time of this final report, three journal papers are in preparation for submission describing the final results of testing, characterization, and modeling.

Freeman, R. A., T. Martin, E. Roberts, and T.W. Knight, Analysis of Thermal Creep for Uranium Silicide Fuel Using BISON, *Proceedings of International Conference on Advances in Nuclear Power Plants (ICAPP 2018),* Charlotte, USA, April 8-11, 2018

Metzger, Kathryn E.; T. W. Knight, E. Roberts, X. Huang; "Determination of Mechanical Behavior of U_3Si_2 Nuclear Fuel by Microindentation Method", *Progress in Nuclear Energy*, 99, 2017, pages 147-154

Metzger, K. E., T.W. Knight, and R.L. Williamson, Model of U_3Si_2 Fuel System Using Bison Fuel Code, Proceedings of International Conference on Advances in Nuclear Power Plants (ICAPP 2014), Charlotte, USA, April 6-9, 2014

Kathryn E Metzger. Analysis of pellet cladding interaction and creep of U_3Si_2 fuel for use in light water reactors. PhD thesis, University of South Carolina, 2016.

Ray Austin Freeman. Analysis of Pellet-Cladding Mechanical Interaction on U_3Si_2 Fuel with A Multi-Layer SiC Cladding Using BISON. Master's thesis, University of South Carolina, 2018.

Coleman Terrapin. Analysis of U_3Si_2 Fuel and The Effects of Creep on Microstructure. Master's thesis, University of South Carolina, 2018.

Emil Mercado. U_3Si_2 compressive creep testing under various stresses and temperatures. Master's thesis, University of South Carolina, 2018.

3. Experimental Setup and Testing

Pellets were received from Idaho National Laboratory (INL) for characterization and testing (see Table 3.1). Extensive characterization was carried out on pellets as described in Chapter 5. Five pellets from batches 3 and 4 were subjected to 13 creep tests at different stress levels and temperatures as described in Section 3.4 below. Details of pellet fabrication are discussed in Chapter 5 but are summarized below.

Table 3.1. Description of the pellet batches used in testing.

Batch Fabrication				
Batch #	Batch 1	Batch 2	Batch 3	Batch 4
ID #	ID 1005 (Pellet C)	ID 1135	ID 1169	ID 1419
Creep tested pellets			150813a 150813b	161214a 161214b 161214c
Particle Size Distribution	Reference distribution for "pellet C"	Reference distribution for "pellet C"	Reference distribution for "pellet C"	Reference distribution for "pellet C"
Sintering heat up	Sintered at 600˚C for 2 hours to remove binders	Sintered at 600˚C for 2 hours to remove binders	Ramped up at 2.5˚C per minute to 600˚C then left for 2 hours to remove binders	Ramped up at 2.5˚C per minute to 600˚C then left for 2 hours to remove binders
Sintering temperature	1500˚C	1400˚C	Ramped up at 30C per minute to 1500˚C	Ramped up at 30˚C per minute to 1500˚C
Sintering atmosphere	Argon	Vacuum	Vacuum	Vacuum
Sintering time at peak temperature	4 hours	8 hours	4 hours	4 hours
U/Si stoichiometry	Higher Si content	Stoichiometric amounts of U and Si	Stoichiometric amounts of U and Si	Stoichiometric amounts of U and Si
Additional Notes			Powder sat in glovebox for a longer period of time (few weeks) before pressing	Powder was pressed within two weeks

3.1 Introduction to Testing Procedures

3.1.1 Telecentric Strain Measurement

A telecentric lens and illuminator setup is used due to the low distortion of the image it provides. Telecentric setups allow for an orthographic projection of the object in the field of view with little distortion. When used in combination with an illuminator, an object placed in between the camera and the illuminator will appear to the camera as a shadow of the object. Due to the collimated and parallel nature of the light rays coming from the illuminator and the properties of the telecentric lens, the shadow that is cast is a high contrast silhouette. Any changes in the objects shadow outline (such as shrinking in height or expansion in the width) will be captured via the changes in the shadow images. [5]

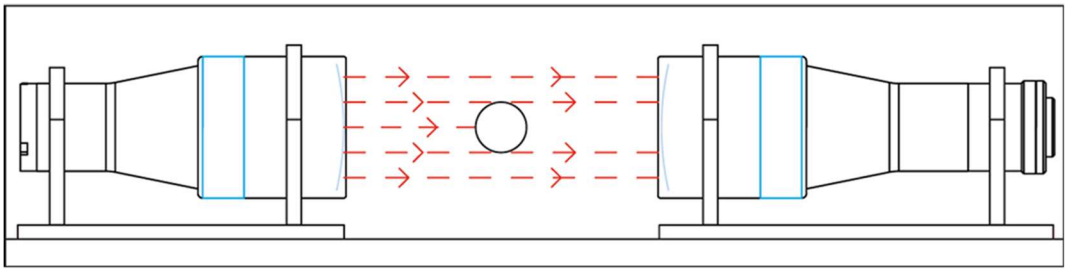

Figure 3.1: Parallel rays from the telecentric illuminator (left) project a shadow to the telecentric lens (right)

3.1.2. Image Processing and Strain Measurement

The captured shadow images are processed using ImageJ and the cvMatch template plugin [13]. The cvMatch plugin takes two images: a template image to match [B] and an initial reference image to search [A].

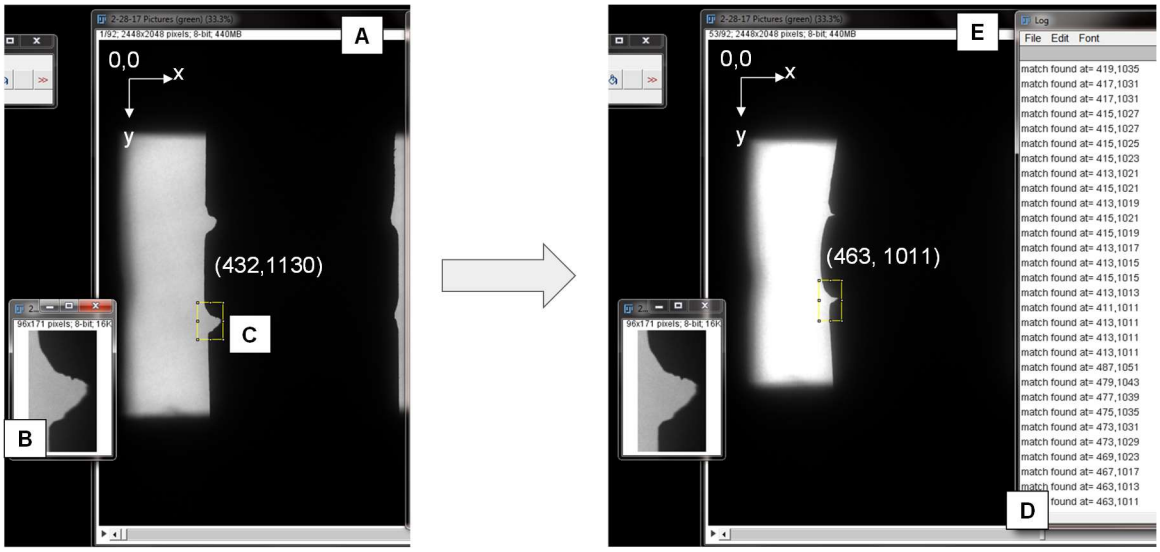

Figure 3.2: ImageJ notch tracking. The initial image is on the left and deformed image is on the right (Sample 150813a)

The pellets are machined with notches to aid in strain tracking. The notches are less than one millimeter deep and are located in the middle third of the pellets height.

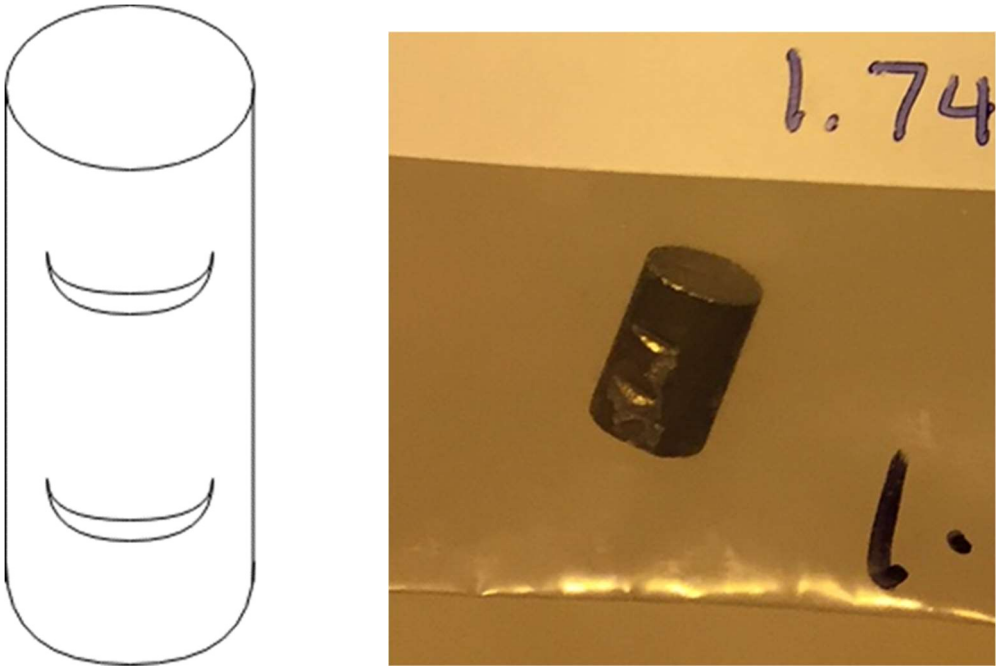

Figure 3.3: Sketch of a notched sample (left) with a typical creep sample (150813a) on the right

In Figure 3.2, the image of a notch [C] is chosen as the template and the test images are used as the reference images. As the pellet deforms, the notch moves and the cvMatch plugin will track the notch in the deformed image [E]. When a match is made, the x and y pixel coordinate positions of the notch are saved [D].

3.1.3 Data Analysis

After processing the images in ImageJ, the x and y pixel coordinates of all four notches are mapped throughout the stack of test images. Axial length (along the height of the pellet) is calculated as the average of the distance between the notches on the left and the right. Diametral length (across the width of the pellet) is calculated as the average of the lengths between the top and bottom notches. The data has been smoothed for better representation with the assumption that the strain is continuous and does not jump back down. The jumps in the original data are likely due to the automated template matching algorithm having problems with the camera and lighting noise in the images. However, general trends are still inferred from the data.

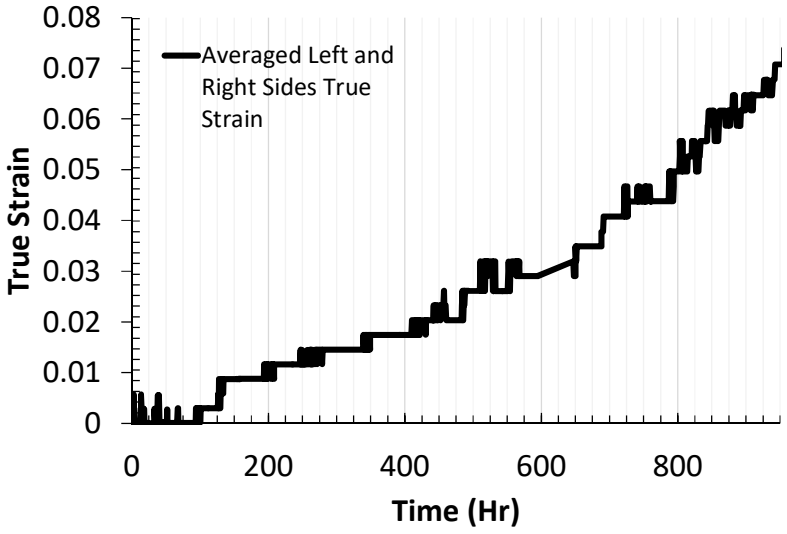

Figure 3.4: Vertical strain time history 161214a (unsmoothed)

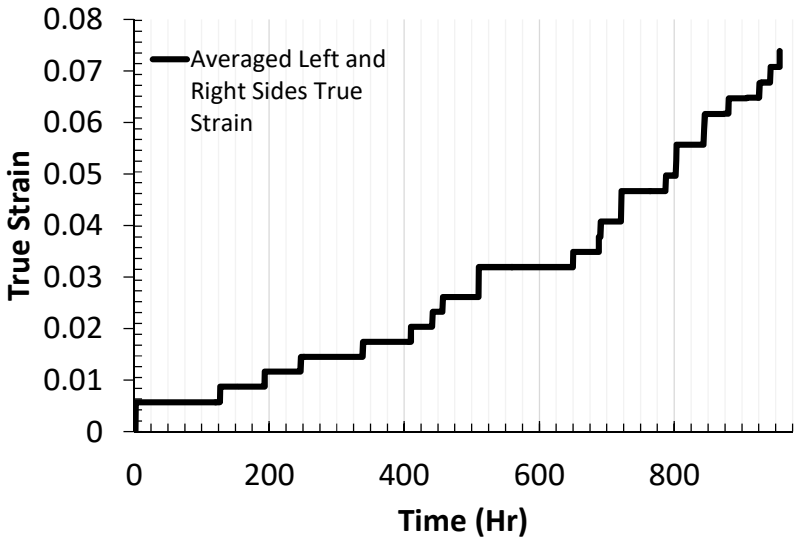

Figure 3.5: Vertical Strain time history 161214a - Smoothed

Each image's time stamp is then correlated with the DAQ time stamp to match the testing conditions with the image time. Steady state strain rates chosen are at a minimum of 100 hours of testing data and are representative of the trends seen in the strain-time history data of the pellets.

3.1.4 True Stress Calculation

To account for changes in sample diameter, instantaneous area is calculated from the axial strain and used for reported stress levels. With a constant volume assumption before and after a deformation

$$A_o l_o = A_f l_f \qquad \text{Equation 1}$$

And with engineering strain equals to

$$\epsilon_{engr} = (l_f/l_o - 1)$$ Equation 2

Finally, with true stress equal to applied load divided by instantaneous (final) area and inserting above equations leads to

$$\sigma_T = F/A_f = F(\epsilon_{engr} + 1)/A_o$$ Equation 3

Engineering strain is obtained from the deformation images with ImageJ and original area is measured before the test begins.

True strain is related to the instantaneous deformation and is calculated with the following equation [16]

$$\epsilon_{True} = \ln(l_f/l_o)$$ Equation 4

The results from this method was checked against a method that uses measurements from the widest area of the pellet image to calculate the stress in the sample. A set of images from pellet 150813b was chosen for analysis.

For a pellet before deformation (dashed line) undergoing a compressive force and experiencing a barreling shape change after deformation (solid line), the dimensions are shown below.

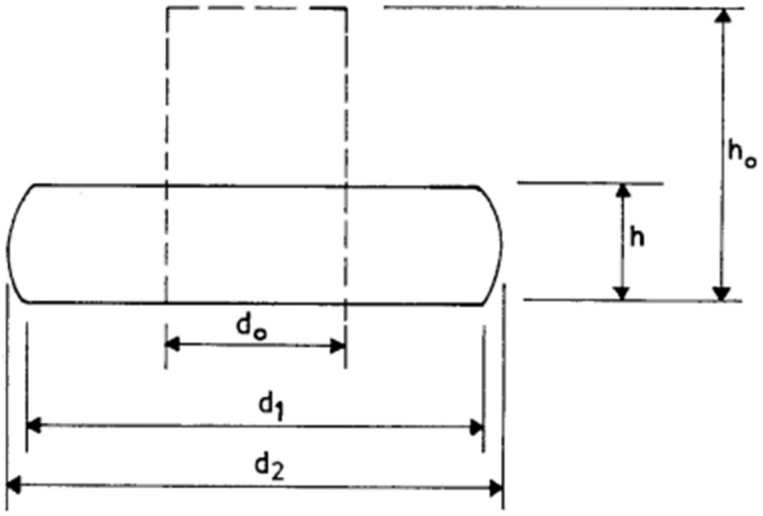

Figure 3.6: Barreling Dimensions Used [17]

Where d1 is the minimum diameter

d2 is the maximum diameter of the specimen

do is the original diameter

h is the height

ho is the original height

The average stress of the barreling specimen is shown in equation 5 [17] below

$$\sigma_{barrelling} = \left(\frac{4L}{\pi d_2^2}\right)\left(1 - \frac{4R}{d_2}\right) ln\left(1 - \frac{d_2}{4R}\right)^{-1} \quad \text{Equation 5}$$

Where R is the radius of curvature [17] is shown below

$$R = h^2 + \frac{(d_2 - d_1)^2}{4(d_1 - d_2)} \quad \text{Equation 6}$$

The stresses obtained from the barreling correction method vs the true strain constant volume method are shown below.

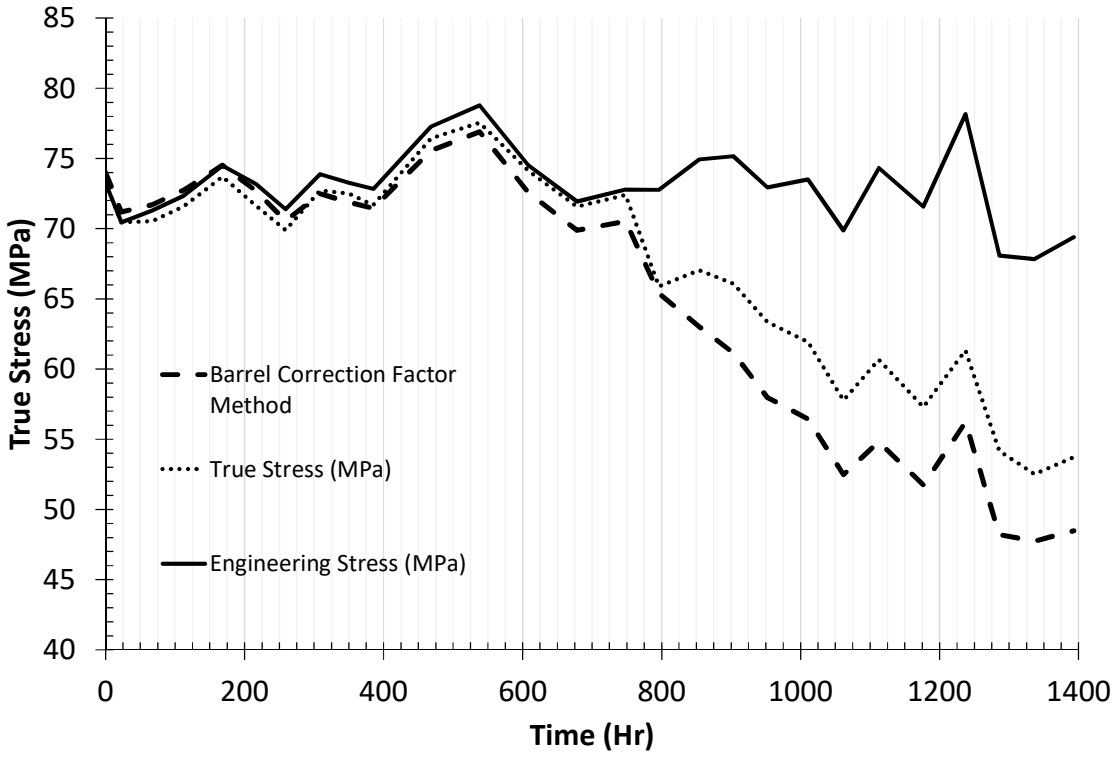

Figure 3.7: Constant Volume Method vs Barrel Correction Factor Method Stress Values (Sample 150813b)

The true stress as developed from the constant volume assumption and the barrel correction factor method [17] are in reasonable agreement within 5 MPa difference. As the maximum diameter is difficult for the automated template matching program to match and that not all samples have their total height captured through the tests (only the notched parts are captured for all samples), the constant volume method will be used for the rest of the report.

3.1.5 Heating Scheme

Direct joule heating is used as the main source of temperature generation in the pellet. High amperage, low voltage, alternating current is chosen due to the relation below where low pellet resistance (10^{-4} ohm-cm) necessitates the high amperage.

$$P = I^2R \qquad \text{Equation 7}$$

3.2 Experimental Setup

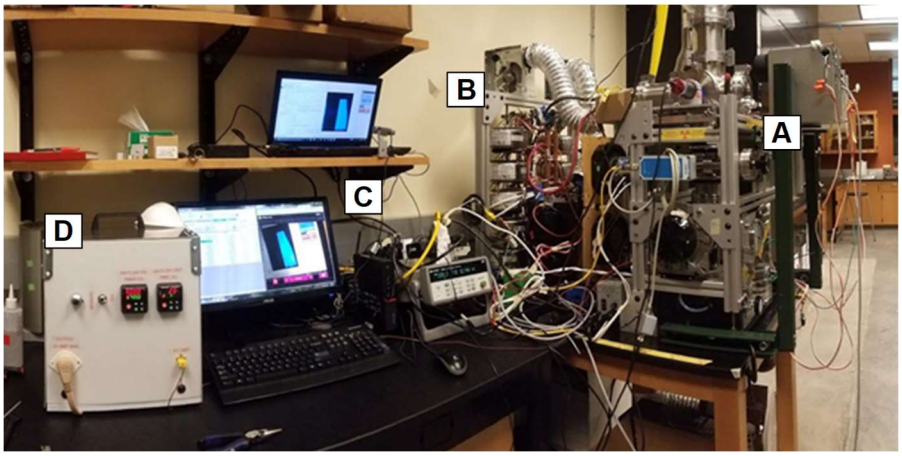

Figure 3.8: Overview of experimental setup

To measure the creep of U3Si2, a test rig was designed and created. It uses a combination of pre-made parts as well as a mixture of fabricated pieces. The description is split into multiple systems:

- Main test chamber and frame
- Electrical power bank
- Temperature controller box
- Data acquisition

3.2.1 Test Chamber and Frame

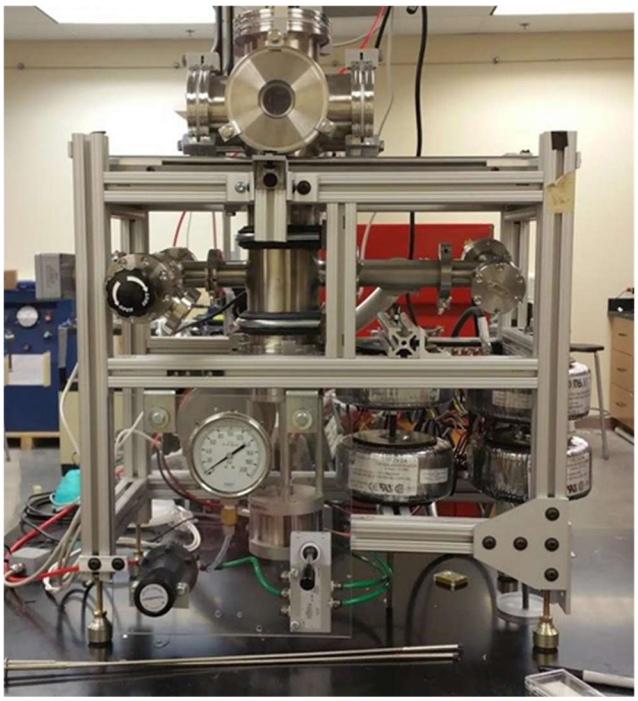

Figure 3.9: Test chamber and frame side view

Frame

An 80/20 extruded aluminum frame was designed and assembled to hold the vacuum chamber and testing equipment. The frame height and level is adjustable via adjustable feet on each of the four legs.

Vacuum Enclosures

304L Stainless steel vacuum enclosures from various manufactures make up the outer casing of the rig. Industry standard vacuum flanges, including ISO100, ISO 45, and ISO 25 flanges are used. Viton O rings and gaskets are used to seal the sealing faces.

Cooling Fans

Cooling fans actively blow air over the test rig. This is to keep the rubber gaskets from becoming too hot and losing sealing effectiveness. In addition, special care is brought to the high current wires, transformer bank, and electrical feedthrough as considerable heat builds up along these high current devices if left uncooled.

Electrical Passthrough

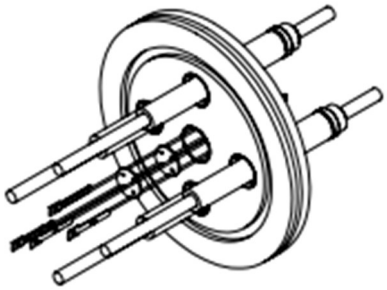

Figure 3.10: Drawing view of electrical pass-through

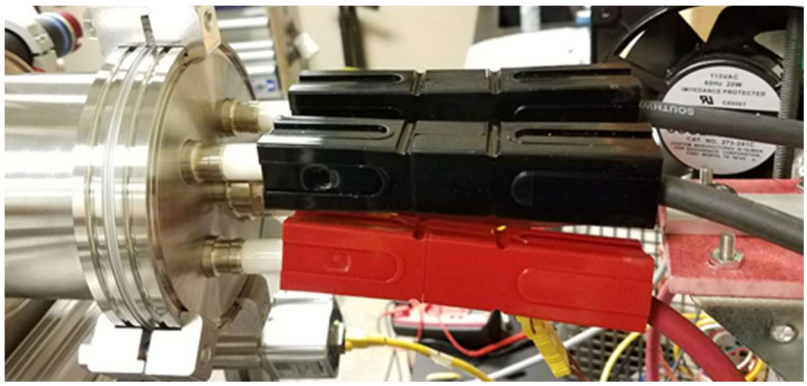

Figure 3.11: Passthrough as Installed on the testing chamber

To allow current to enter the vacuum environment of the test rig, an electrical pass-through was installed. It is comprised of four, quarter inch copper terminals (two for input current and two for output current) and two K type thermocouple slots which allow for temperature measurement inside the testing stand. The maximum amperage of each copper terminal is 180 Amps for a combined maximum heating current of 360 Amps when used in pairs.

Loading Frame

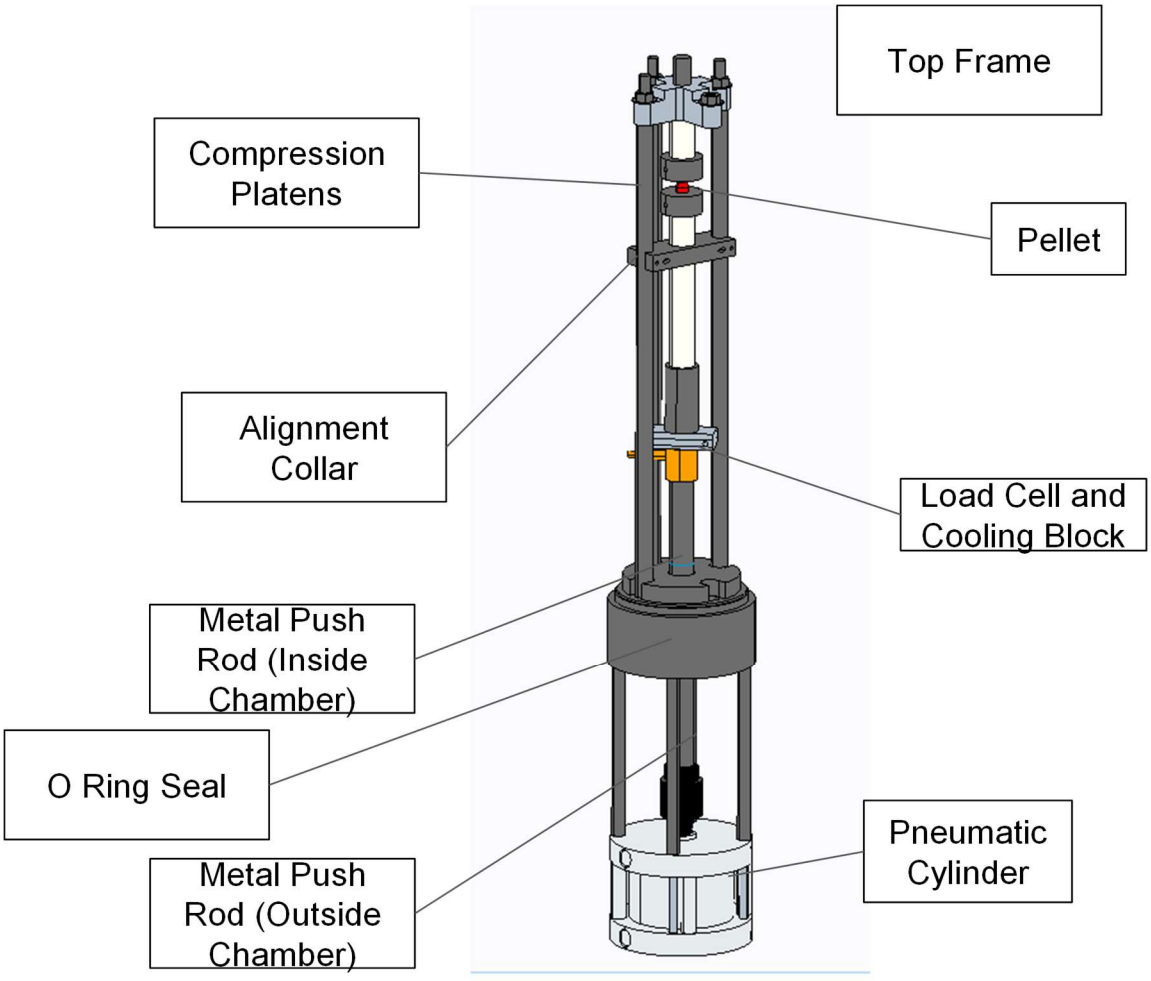

Figure 3.12: CAD Design of internal loading frame

The test pellets are compressed via the loading frame. It is comprised of multiple pieces that work together to apply force to the pellet.

Figure 3.13: As constructed internal loading frame

Pneumatic Cylinder and Regulator

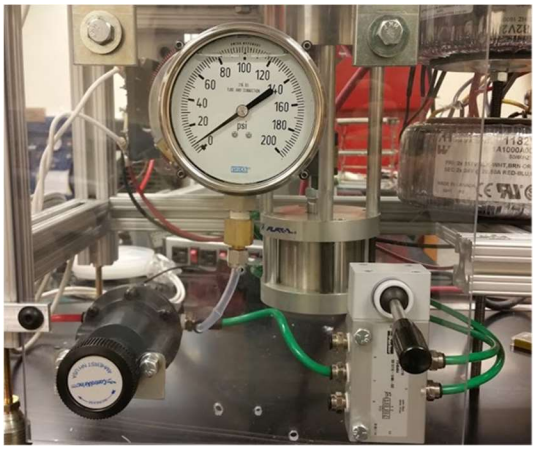

Figure 3.14: Operator panel for the pneumatic cylinder

From the bottom up, the loading frame starts at the pneumatic pancake cylinder. The cylinder accepts air pressure from the building air pressure line (at approximately 100psi) and is controlled via an air regulator. The cylinder is attached to a metal push rod which then enters the vacuum chamber to apply load to the sample. A set of O-rings seals the vacuum chamber and the metal push rod to maintain the vacuum environment.

Load Cell, Water Cooling Block and Ceramic Collar

Figure 3.15: Load cell assembly with water pass through

Attached to the push rods is a Futek load cell rated for 2000 lbf to measure the load applied to the sample. It is placed inside the testing chamber to reduce the frictional effects between the test chamber and the metal push rod.

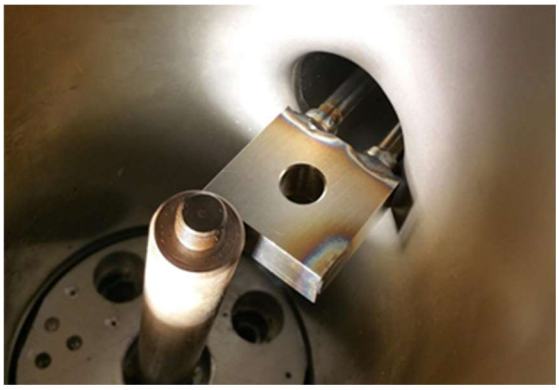

Figure 3.16: Water cooling block in test environment

A water cooling block transfers heat from the ceramic rods (which are hot due to the high temperature pellet) away from the load cell. Cool water is brought into the system via a water feedthrough and comes from the buildings water supply. A thermocouple that is attached to the load cell then monitors the temperature and effectiveness of the cooling block during the tests. It is attached to the temperature controller box and attached to the limit controller which cuts off system power if the load cell reaches a specified temperature limit.

Figure 3.17: Assembled load frame in chamber

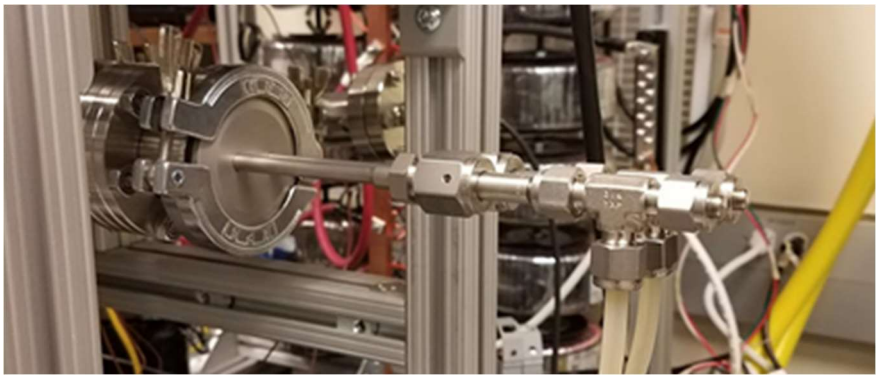

Figure 3.18: External water supply feedthrough

Adjustable Alignment Collar

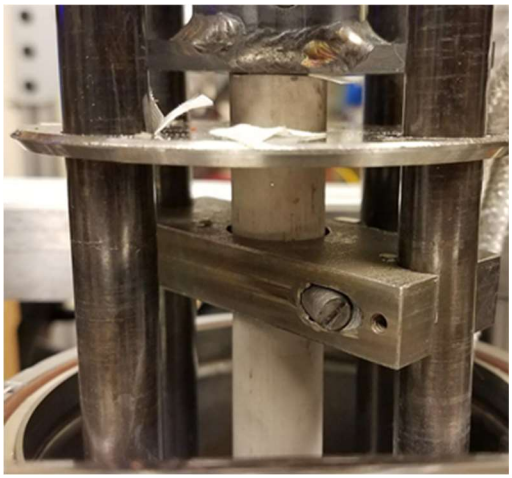

Figure 3.19: Alignment collar underneath bottom platen

To keep vertical compression alignment, an adjustable collar holds the ceramic compression tube in line. Internal ball bearings keep the rod aligned and are adjustable via a set of three set screws.

Compression Platens

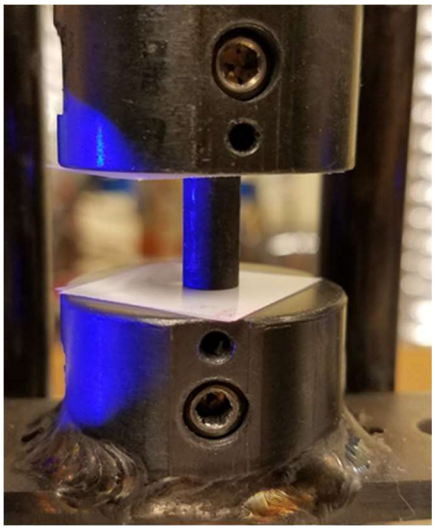

Figure 3.20: Top and bottom compression platens with a dummy graphite sample

Two Inconel platens were fabricated that attach to the ceramic tubes. [14] This bottom platen serves as the bottom platform on which the U3Si2 pellet sits on. Current flows through this bottom platen, through the U3Si2 Pellet, then leaves through the top platen for the joule heating setup. Copper Bus bars connect these platens to the power feedthrough which then connects to the electrical system.

Figure 3.21: Inconel platens as installed in testing chamber

Top Cross

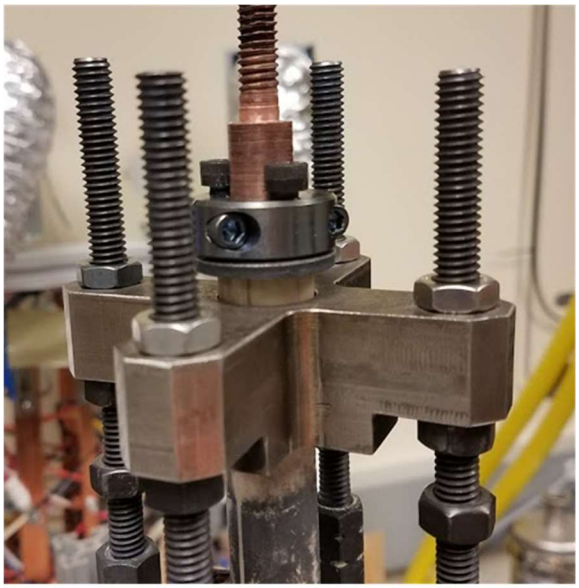

Figure 3.22: Top holding cross

The top holding frame is fixed to four posts and holds in the top loading frame ceramic tube. Using the four adjustment nuts, it is adjusted to ensure that the two platen faces are parallel with each other.

Heat Loss Reduction

Multiple pieces were created to reduce the heat loss from the pellet and to reduce the load provided electrical heating power bank. Many of these parts focused on reducing parasitic heat loss from the hot pellet.

Radiation Heat Shield

Figure 3.23: Stainless steel heat shield with viewing holes

Figure 3.24: Heat shield top view. The sample is contained in the middle

It was observed that at approximately 700°C, the pellet begins to emit a dull orange glow. As the pellet increases temperature, the glow becomes brighter and loses heat to the surrounding vacuum walls and system pieces via radiation. To reduce this radiative heat loss, a multi layered shield was designed and constructed via multiple steel sheets cut by a water jet. It is comprised of multiple layers of stainless steel foil that are concentrically arranged around the pellet. To reduce conductive heat transfer between the foil layers, ceramic screws separate each layer. The shield is slid around the pellet before the test is conducted and slides upwards when the pellet is to be removed.

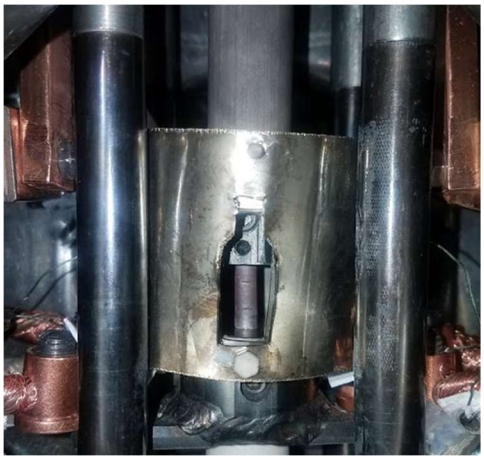

Figure 3.25: Radiation shield as installed in testing chamber

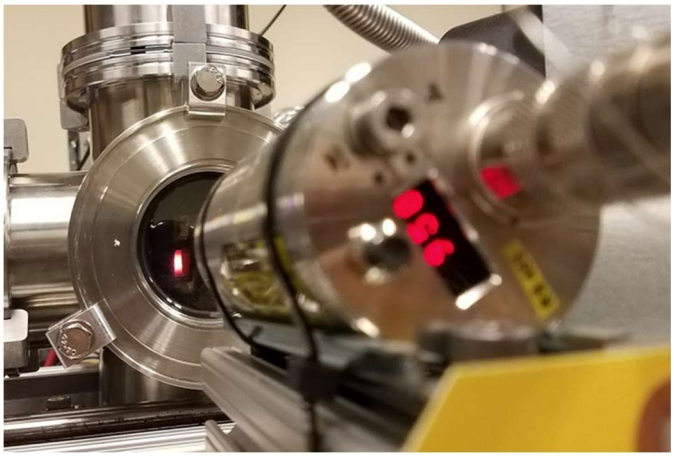

Figure 3.26: Glowing sample with pyrometer sighted on it

There are holes that allow for the telecentric optical setup to see the pellet as well as the pyrometer to sight the sample.

Ceramic Tubes

Figure 3.27: Top and bottom zirconia tubes

Mullite ceramic tubes are used to curtail the heat loss from the pellet. Compared to steel, mullite tube have a much lower thermal conductivity but are still suitable for the applied loads of the test. [15] In addition, ceramic felt washers were cut via laser cutter and inserted in between the Inconel platens and the ceramic rods to further increase thermal resistivity.

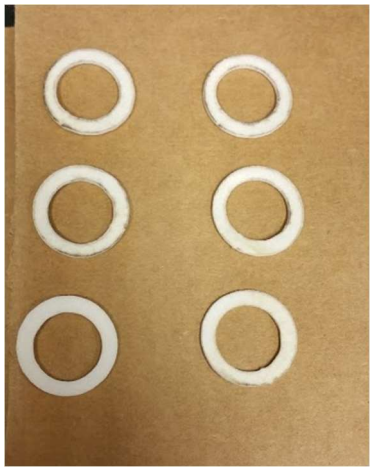

Figure 3.28: Ceramic felt washers

Active Guard Heater Cartridges

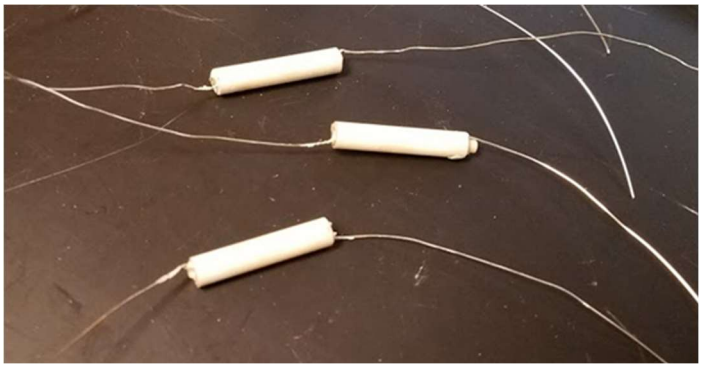

Figure 3.29: NiCr wound cartridge heaters

Figure 3.30: Cartridge heaters inserted into top platen

Cartridge heaters were sized to be inserted into holes found in the top and bottom platens. Ceramic tubes ensure that the guard heater circuit does not interfere with the main heater power supply circuit. When a voltage is applied to these cartridge heaters, the high internal resistance of the NiCr wires causes the cartridge to heat up to temperatures up to 900°C. This creates a hot zone above and below the sample which helps to reduce the conductive heat loss from the sample.

Figure 3.31: Active guard heaters in test

Vacuum Pumps

Figure 3.32: Roughing vane pump for low vacuum

To reduce oxidation effects during high temperature testing, the tests take place in a vacuumed environment. Two vacuum pumps work in tandem to bring the system down to high vacuum levels. The first stage roughing pump brings the vacuum environment to

a low vacuum (approximately 10^{-1} mBar) at which point it reaches a steady state. The second stage turbomolecular pump then takes the system to 10^{-3} mBar.

Figure 3.33: Turbomolecular pump to bring system to high vacuum

In the event of a power loss or a vacuum interruption, an automatic shutoff valve has been installed to maintain the vacuum levels and environment inside the test rig that will seal the testing environment if it detects a power loss. Uninterruptable power supplies provide shorter power for all systems and allow the system to run fully for approximately 30 minutes.

Sensing Equipment

Figure 3.34: Zirox oxygen partial pressure probe

To measure the oxygen partial pressure history, a Zirox SS-28H vacuum probe is used. The sensing electrode heats up to 700°C and measures oxygen concentration inside the testing chamber versus the oxygen environment outside the testing chamber (considering the outside environment as the baseline). Effective range is from 1E5 Pa to 1E-21Pa with less than a 5% relative error. [1]

Figure 3.35: Total vacuum gage

An Oerlikon PTR 90 vacuum gage measures total vacuum pressure. The measurement range for the total vacuum pressure is 5E-0 to 1E3 mbar with an accuracy of +/- 30%. [2]

Figure 3.36: In-line compression load cell

The Futek Lcb200 tension and compression load cell measures the force the sample is receiving. The load cell has a 2000 lbf maximum load rating and nonlinearity and hysteresis values of 0.5% of the output; the non-repeatability is 0.1% of the output. [4]

A total of four thermocouple passthroughs allow for temperature sensing inside the test rig; each allows for a K type thermocouple to be attached. Thermocouples are installed onto the load cell as a check to ensure that it does not overheat due to the high temperature test. In addition, a thermocouple is attached inside the bottom Inconel platen to get a better sense of the temperature distribution inside the testing chamber directly underneath the sample.

Figure 3.37: Lumasense ISR6 Noncontact pyrometer

A Lumasense ISR6 MB 18 Advanced Pyrometer is used to measure the sample temperature and is run in two color mode without having to touch the sample. Emissivity ratio is adjustable via the software. Previous efforts have been made to calibrate the emissivity ratio to U3Si2 to match the pyrometer temperature output to that of a thermocouple. The pyrometer is capable of measuring between 700 to 1800°C with a measurement uncertainty of up to 0.6% of the reading. In the sighting range used, the spot size was approximately 1mm. [3]

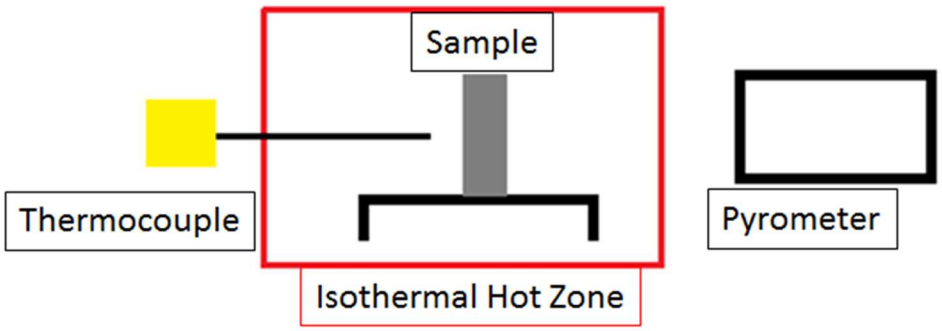

Figure 3.38: General setup of pyrometer calibration

To calibrate the pyrometer to read accurate test values, a test was conducted to match the pyrometer readings with that of a thermocouple. A U3Si2 Tile was placed into a furnace with an argon gas input. The furnace zone was assumed to be isothermal and considerable efforts were made to make it so including blocking off the heating area with ceramic insulations. The thermocouple was placed within a centimeter of the U3Si2 tile, inside the hot zone, and the pyrometer was sighted onto the sample. It was assumed that the thermocouple was reading the correct temperature value of the furnace zone and that the tile was the same temperature as the furnace zone. The furnace began a heating cycle to 1300˚C. At every 25°C, the pyrometer emissivity value was changed so that the pyrometer reading would match the thermocouple. This would allow for a calibrated

emissivity ratio value which could be used for a corresponding value of U3Si2 temperature.

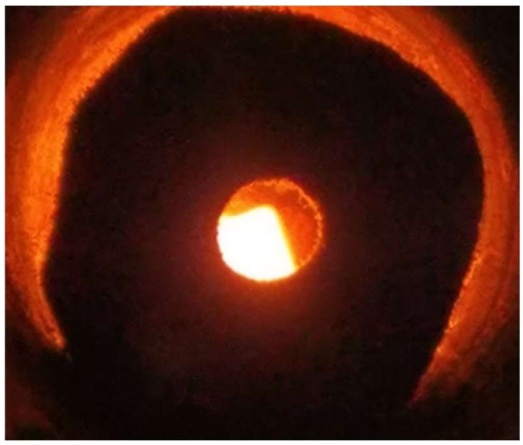

Figure 3.39: View from pyrometer port of the U3Si2 tile for calibration testing

Optical Equipment and frame

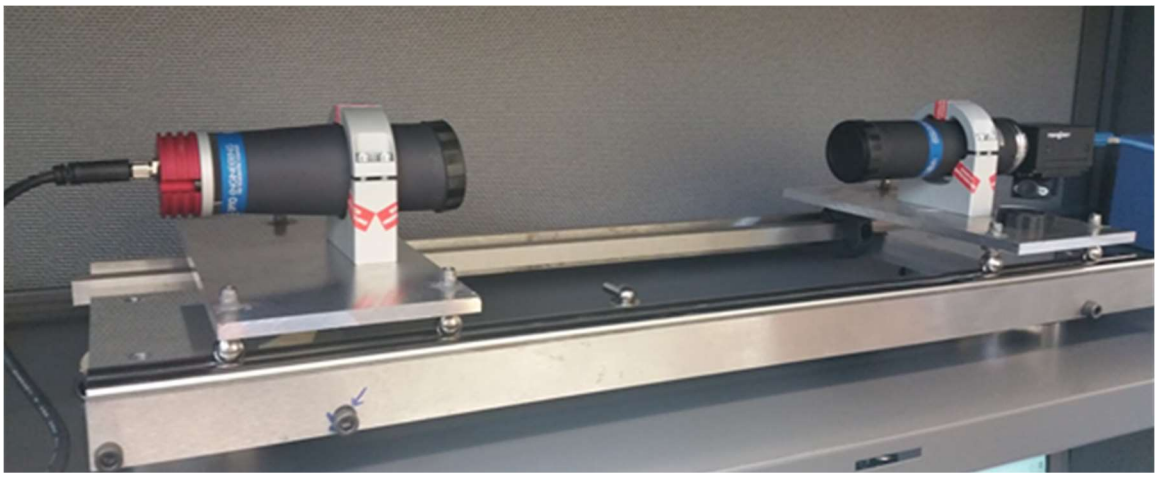

Figure 3.40: Telecentric camera and illuminator on frame

To measure visual changes in the sample, a telecentric camera lens and light source were employed. The camera used is a Grasshopper 5.0 MP Firewire Camera with a resolution of 2448x2048, a pixel size of 3.45 um. [9]

The camera is mounted to a long distance telecentric lens [7] with a working distance of 132.3mm, a maximum distortion of 0.2% and an object field of view of 16.9 x 14.1 mm x mm. The illuminator light source [8] has a blue color corresponding to a 460 nm wavelength and a working distance range of 45-90 mm and is mounted directly opposite to the camera system. All optical components are mounted on movable carts which are kept aligned through a system of precision ground rods and surfaces.

The optical frame has been assembled on a stone table to ensure a flat plane of conformity. In addition, either end of the frame has been milled from the same block of aluminum to better aid in alignment. Two ground rods and a bar stock are then slid into these block of aluminum and provide the surface on which the optical carts move along.

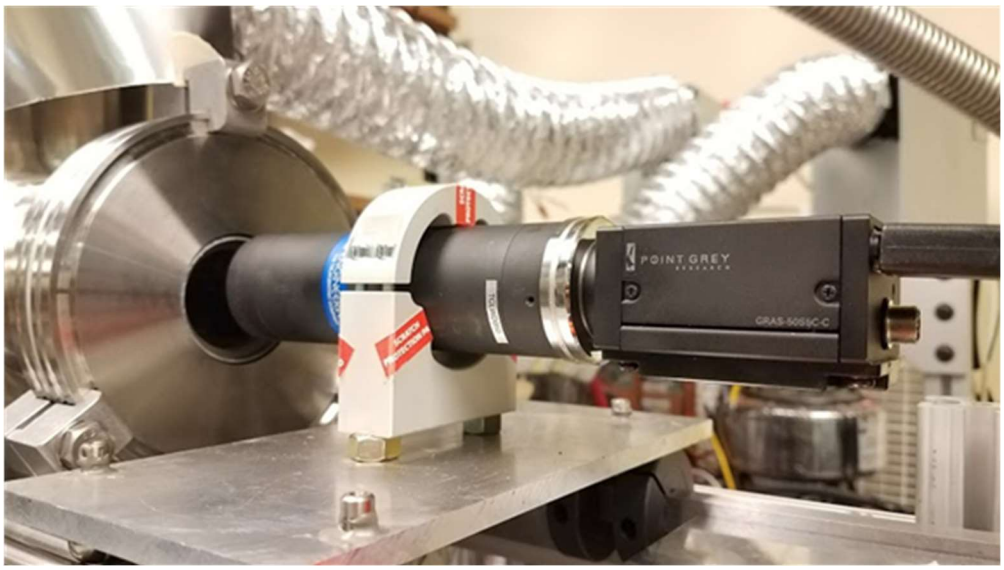

Figure 3.41: Camera as focused on the sample outside of the test rig

Borosilicate glass windows allow for viewing into the test rig. Installed on the six way vacuum chamber are three glass windows: two allow for the telecentric camera and illuminator to view the sample and one allows for the pyrometer to measure sample temperature.

3.2.2 Electrical Power Bank

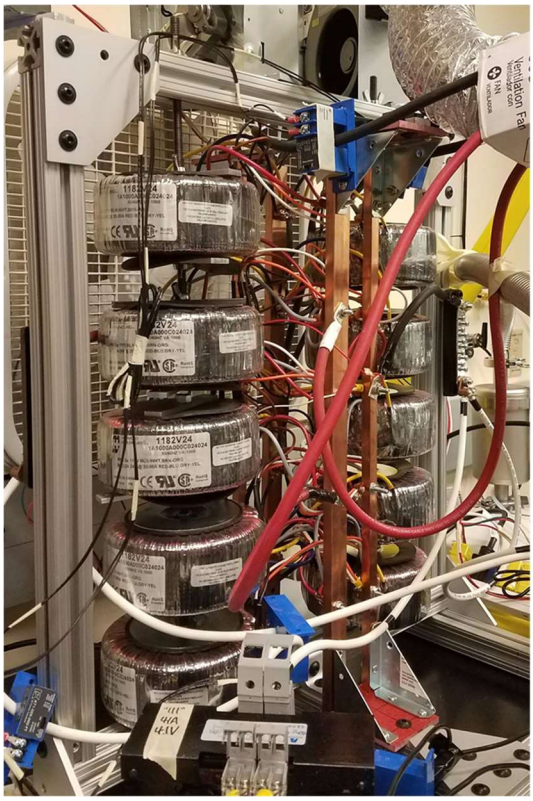

Figure 3.42: Final stage of power bank chain

A multi stage step down, AC power bank chain is used to drive the joule heating scheme. The power chain begins with an initial stage VARIAC which allows for a coarse adjustment of power input. After the first stage VARIAC, the load is then fed to an intermediate transformer bank. The intermediate transformers are a bank of four ACME FS11000 transformers [10] wired in parallel. Voltage is stepped down in this intermediate step and amperage is stepped up until it is fed to the final stage power bank. The final transformer bank is made of 10 Hammond Manufacturing 1182v24 colloidal transformers which is the last step down stage before the current enters the sample [11].

3.2.3 Temperature Controller Box

Figure 3.43: Front panel of temperature controller box

To regulate temperature fluctuations a temperature controller box is implemented using an internal Solid crystal rectifier to modulate the input power to the power bank.

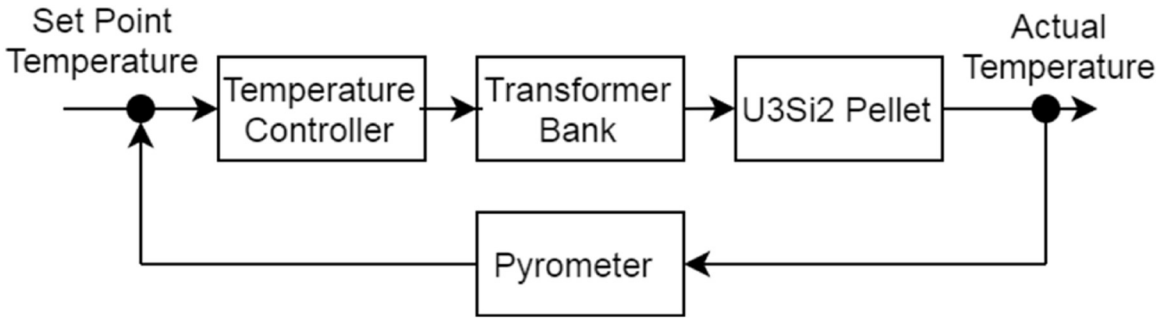

Figure 3.44: Closed loop control diagram

The temperature controller box allows for closed loop feedback control. The input temperature from the pyrometer is compared with the set temperature. The Watlow pm6rf1a PID adjusts the input power via the SCR unit to automatically match the two values. The main power bank is connected directly to the SCR unit.

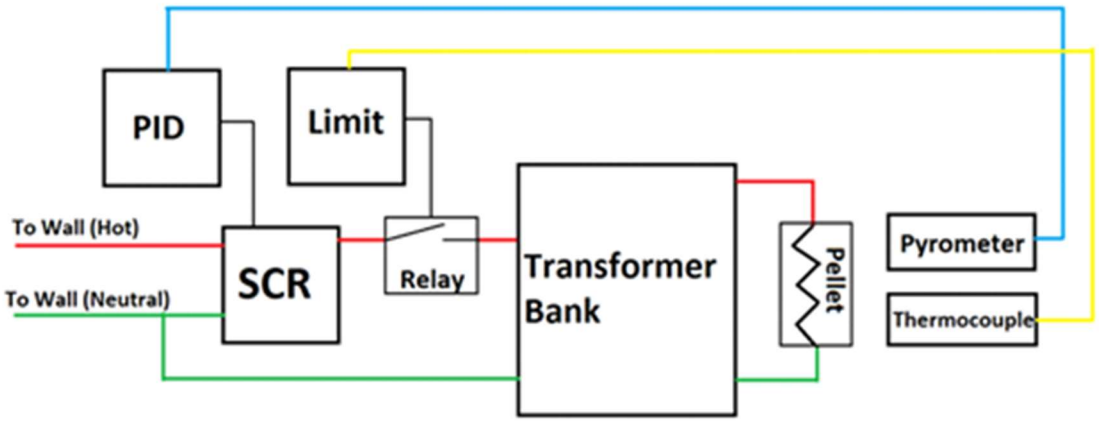

Figure 3.45: Functional diagram overview of electrical system

3.2.4 Data Acquisition and Computers

All sensors are connected to the Agilient 34972A Data Acquisition Switch Unit (DAQ). The DAQ is periodically stopped to save the data but in general, runs continuously with the camera system throughout the creep tests. The measurement accuracy of the DC voltage of the DAQ is between 0.0006 and 0.0035V. [6]

Remote monitoring is done through an automatic screen capture software to periodically check in on the status of the test.

Figure 3.46: Data acquisition unit

3.3 Testing Procedures

Platen Alignment

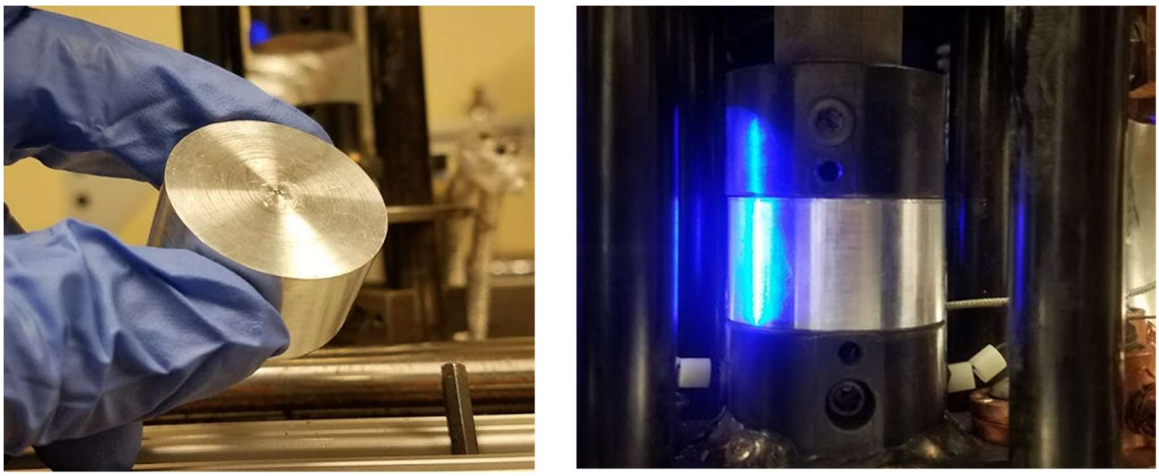

Figure 3.47: Alignment puck to keep faces of the compression platens parallel

To ensure that the top and bottom platens are aligned so that their faces are parallel with each other, alignment pucks were made. The pucks were lathed out of aluminum round bar stock and were measured with calipers to be of a uniform height (maximum of 0.5 mm difference).

The puck alignment process is as follows: It is first placed on the bottom platen. Next, the fully assembled top frame assembly is lowered so that the top platen touches the top face of the alignment puck. Finally, the top assembly is tightened onto the load frame, tightening onto the alignment puck. The bottom platen is lowered allowing it to removed, leaving the faces between the top and bottom platens parallel and aligned.

Rubber Blank and Prescale Check

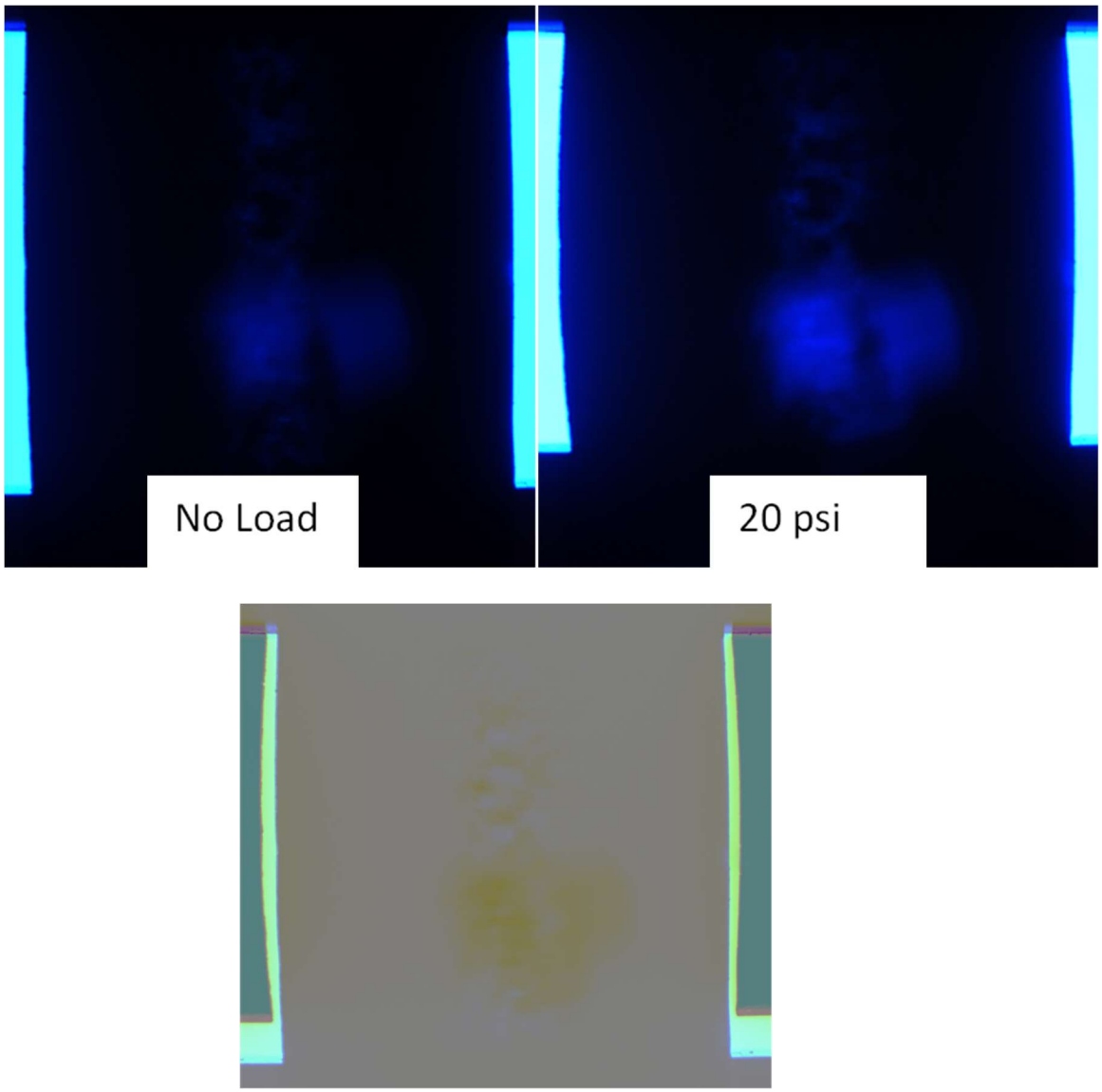

Figure 3.48: Rubber blank as viewed from the telecentric camera

To check for alignment accuracy, a rubber pellet blank roughly the size and diameter of a creep pellet sample was cut. The rubber pellet blank is centered on the pellet and compressed. The image of the blank is compared before and after and checked for symmetry.

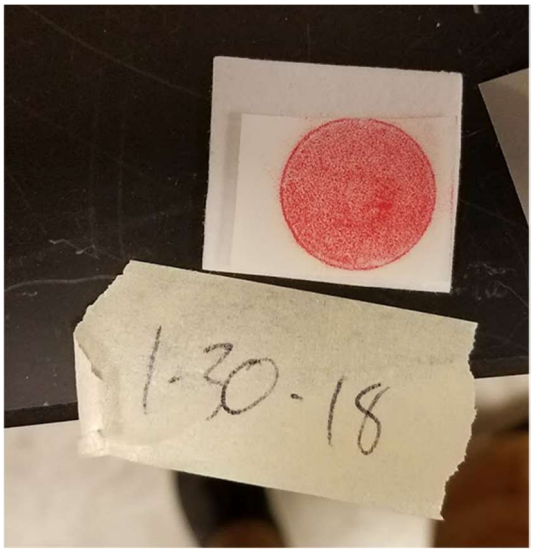

Equation 7: Prescale film results (from sample 161214a)

In addition, pressure sensitive prescale film allows for a full field measure of the pressure distribution of the compression platens. The higher the pressure in an area the deeper the color. Low pressure prescale (useful to 2.5 ~10MPa) was used. [12] The prescale is compressed by the platens and the color distribution due to the pressure from the compression is transmitted to the prescale film. The platens are aligned using the adjustable bottom collar and the top holding plate until the shadow image of the compressed rubber blank is symmetrical and the prescale color distribution is evenly red.

Sample Alignment

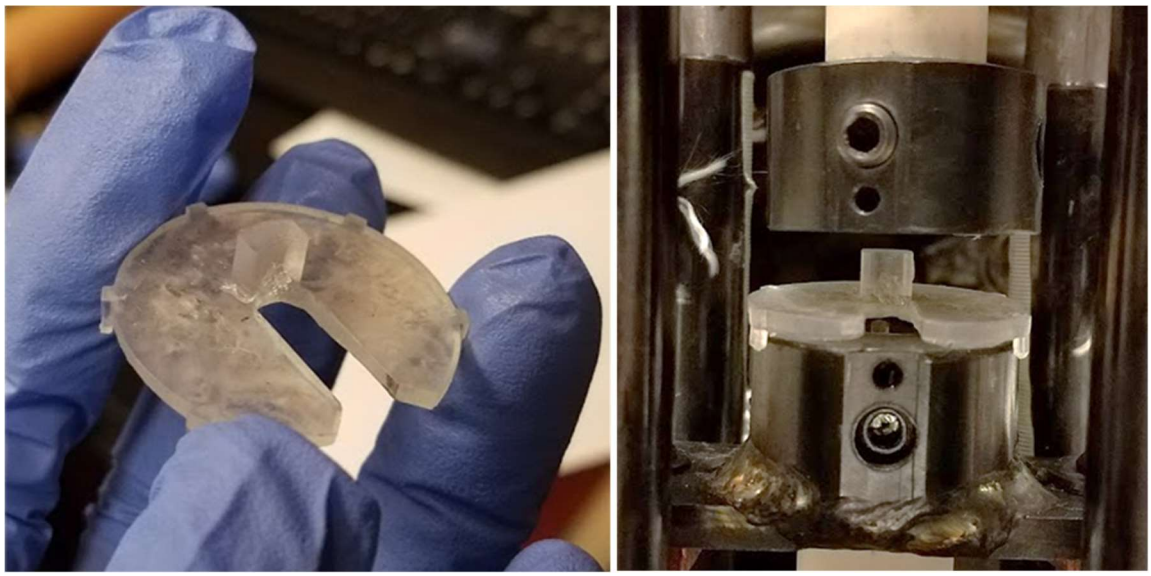

Equation 8: Pellet alignment puck

A 3D printed pellet alignment puck was created to facilitate insertion of the pellets onto the center of the platens. The pellet alignment puck is sized to the diameter of the bottom platen and allows for the pellet to be placed in the center of the platen.

General Procedures

After sample insertion, the camera is focused on the pellet and fixed in place via shaft collars. It is then connected to a PC that captures a shadow image at predefined intervals and does not move during the test. The telecentric illuminator is placed on the same track as the camera and pointed towards it. The pyrometer is sighted to the sample through the pyrometer viewing window.

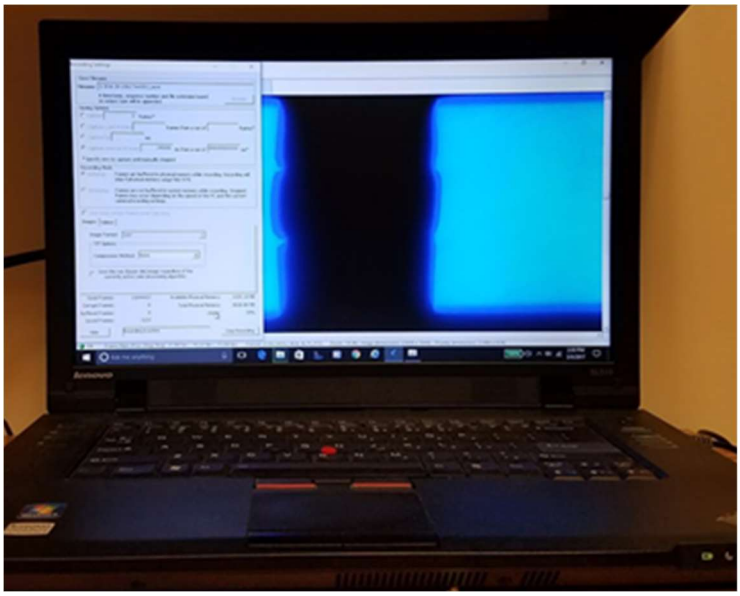

Figure 3.49: Image capture computer with camera sighted on sample (sample 150813b)

The system is sealed by closing off all ports and attaching all necessary vacuum pieces. Sensing equipment is then turned on to record the test. The DAQ is turned on and set to record until stopped and the PC that captures shadow images is triggered to take a picture at predefined intervals.

Then the vacuums are turned on. The roughing pump is the first stage vacuum that removes the majority of the atmosphere in the test chamber. An automatic switch turns on the turbomolecular pump when the pressure is low enough for it to activate. The vacuums run overnight before any heating or loading takes place to reduce contaminants that remain in the test chamber.

The sample is then heated and loaded. Using the temperature controller box and the pyrometer input, the sample is automatically heated at 3 °C per minute. At the same time, the active guard heaters are turned on. The sample is then loaded at a slow rate.

Pressure is dialed in via the adjustable turn knob and some time is waited before increasing the pressure again. This process continues until the set load is achieved.

3.4 Data Collection

Data for all tests are shown. All data shown start after the sample is loaded and heated to the initial testing conditions. Representative images of the sample are shown after the strain history plots.

Sample 150813a

The strain vs history graph of sample 150813a is shown in Figure 3.50. This was the first successfully crept sample of all the tested pellets. The straight line seen between 310-370 hours on the dashed temperature line is an estimation of temperature. It was during this time the pyrometer emissivity ratio was being calibrated to the U3Si2 Tile. All values for this test, however, were back calculated and are based on that calibration.

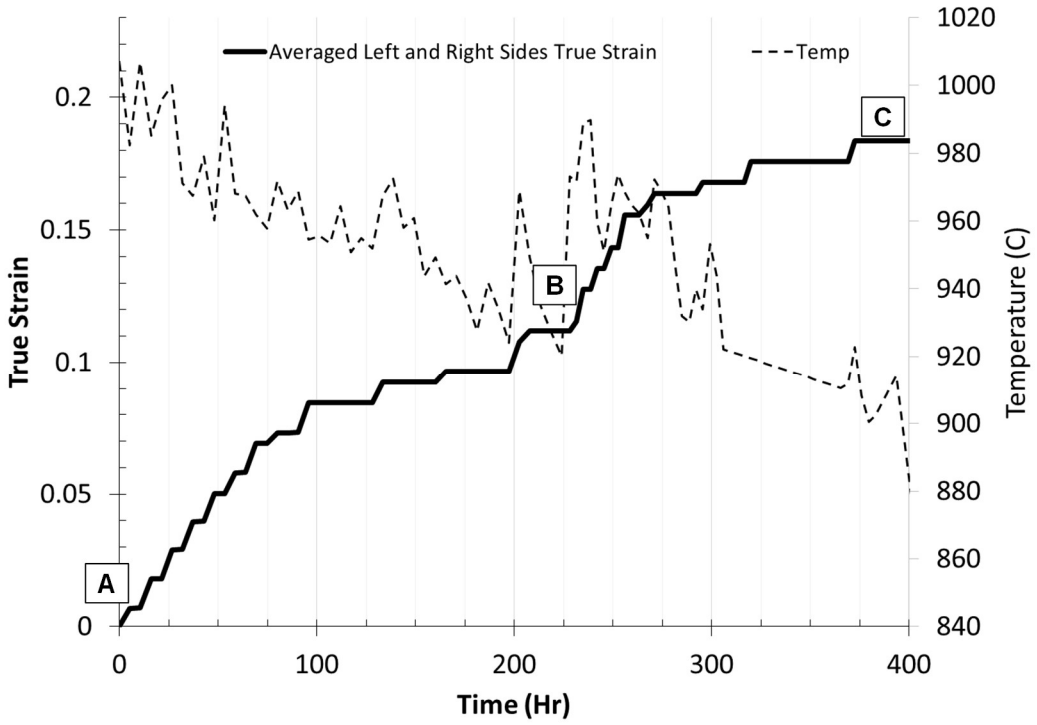

Figure 3.50: 150813a strain time and Temperature history

Sample 150813a was tested before the closed loop temperature controller was implemented. As such, the strain time history graph appears to show clear areas of primary and secondary creep but this is believed to be due to the temperature variations. A faster strain rate (the slope of the solid line) can be readily seen in hours 0-100 and 200-260 but these directly occur when the temperatures was higher at that time. It is believed that the faster strain rate is due to these higher temperatures. A more detailed analysis of this is provided later in the report.

The shadow images of 150813a are shown in Figure 3.51. The notches from this batch are differently shaped due to differences in cutting techniques.

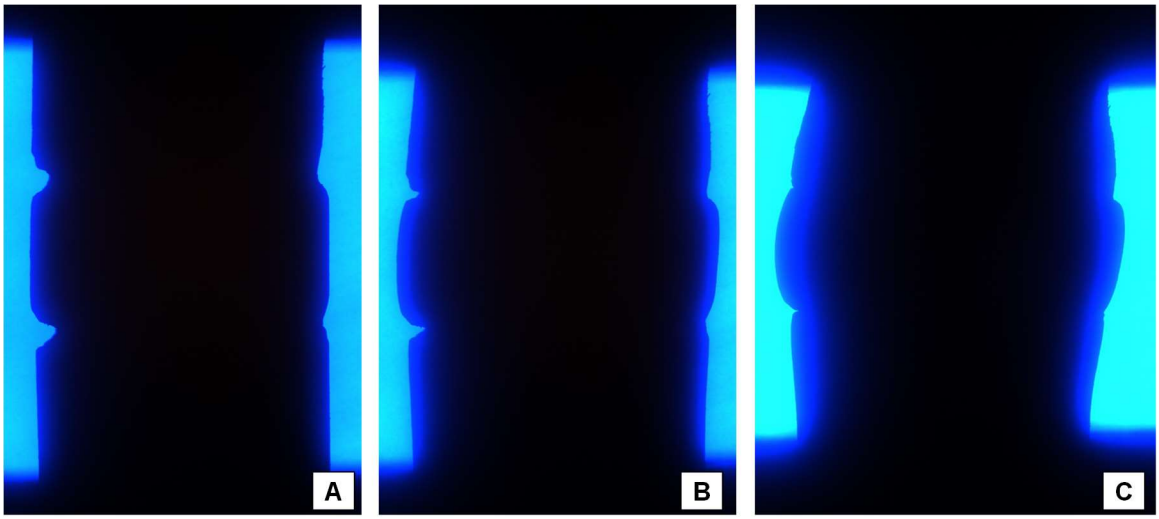

Figure 3.51: 150813a shadow images

150813a was tested at two stress states, 50 and 78 MPa, as seen below in Figure 3.52. The partial pressure of oxygen levels out at 100 hours and is likely due to the oxygen gettering effect of the hot testing environment (platens, internal copper wires, etc.).

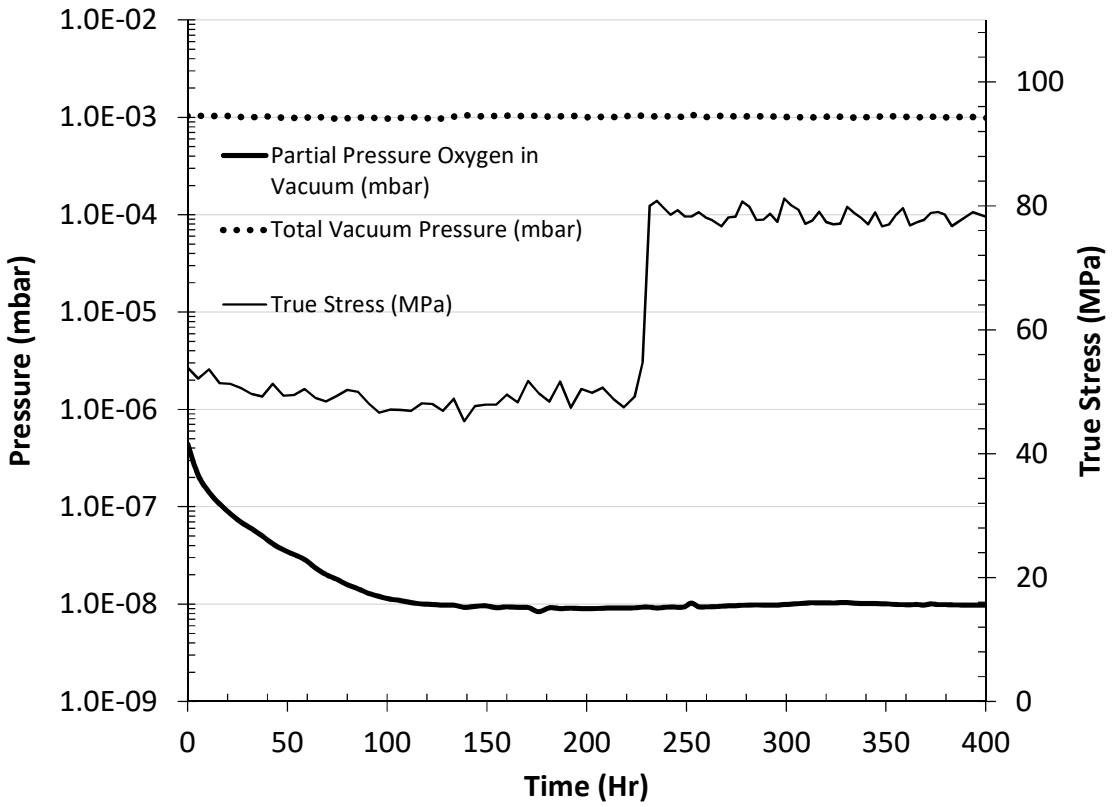

Figure 3.52: 150813a pressures and stress history

As seen in Figure 3.53, sample 150813a was strained up to 18% Vertical strain before a transformer failure abruptly stopped the test. Diametral strain rates remain below vertical strains and appear to follow the same sensitivity to temperature as described earlier.

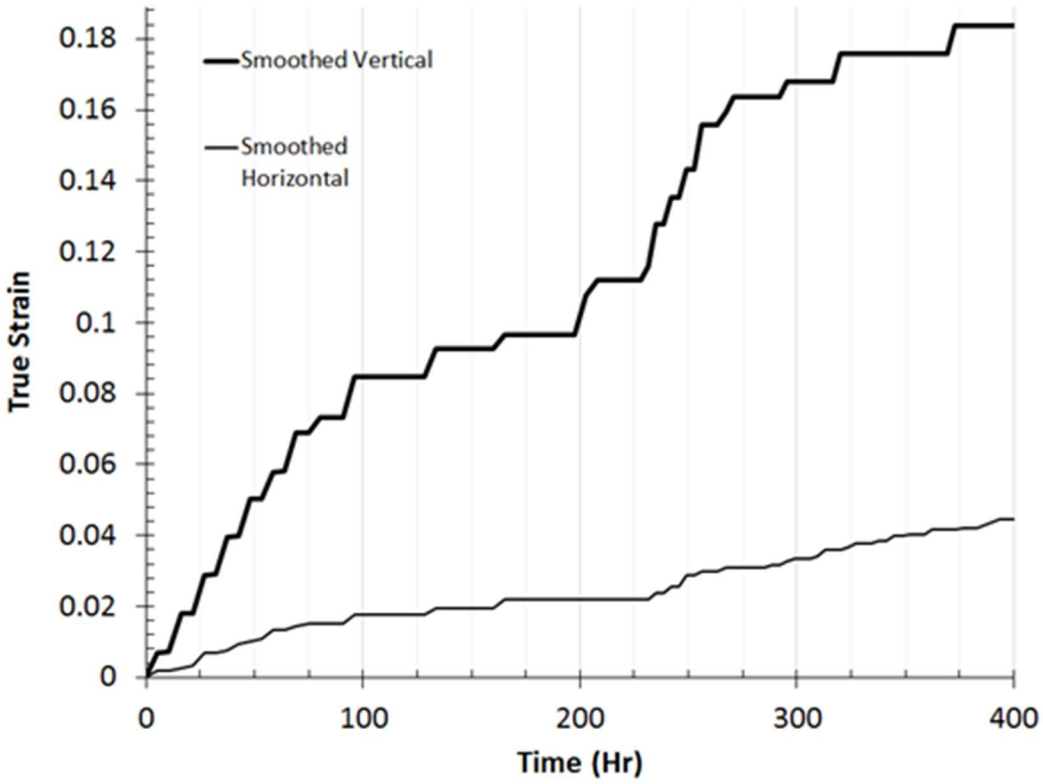

Figure 3.53: 150813a Diametral vs vertical strain history

Sample 150813b

Sample 158013b was the final creep pellet tested before the closed loop temperature controller was implemented. Similar sensitivity to the temperature transients can especially be seen between 790-830 hours. This sample was strained to the highest vertical strain of all samples tested. Low temperature (~850˚C) and high stress conditions was chosen for the first set of testing conditions as seen 0-800 hours; the flat portions of the vertical strain line (hours 300-500, 550-790) are likely due to the small deformations that could not be readily captured by the optical system. However, a general trend can still be seen for the testing conditions.

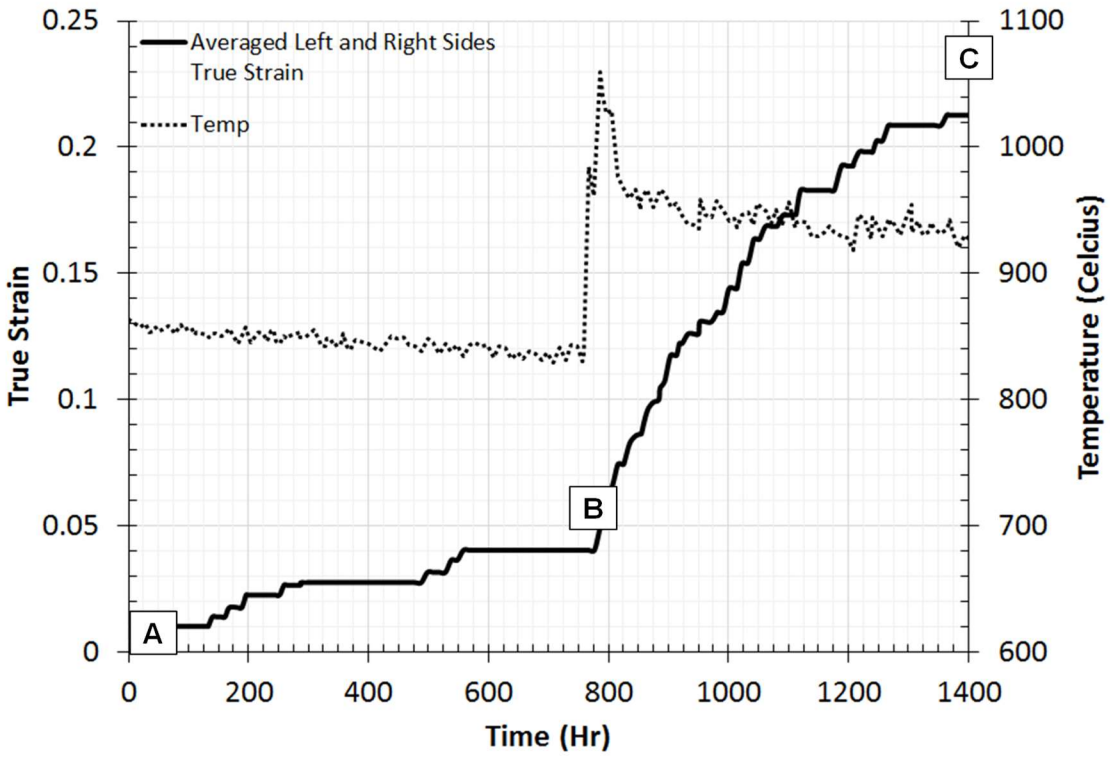

Figure 3.54: 150813b vertical strain time history

As seen in Figure 3.55, sample 150813b was imaged in its entirety (as opposed to other samples where the radiation heat shield obscured parts of the top and bottom) and was chosen to use the barreling calculations performed earlier in the report. The orange color of the sample is due to the increased temperature as the sample begins to glow at around 900˚C.

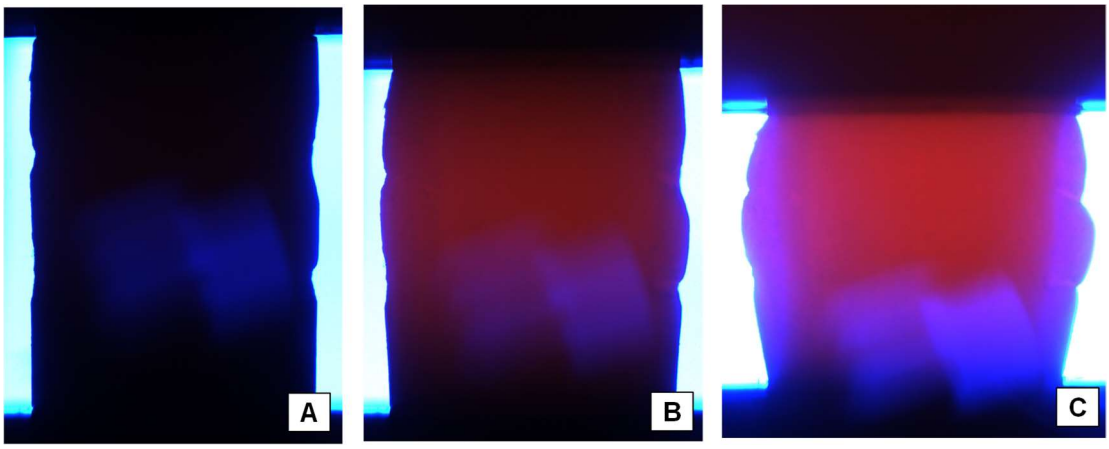

Figure 3.55: 150813b shadow images

Pressure and true stress for 150813b are shown in Figure 3.56. The decreasing stress line (solid black line) between hours 800-1400 are due to the increasing area of the sample; as the load was still kept constant, the true stress decreased.

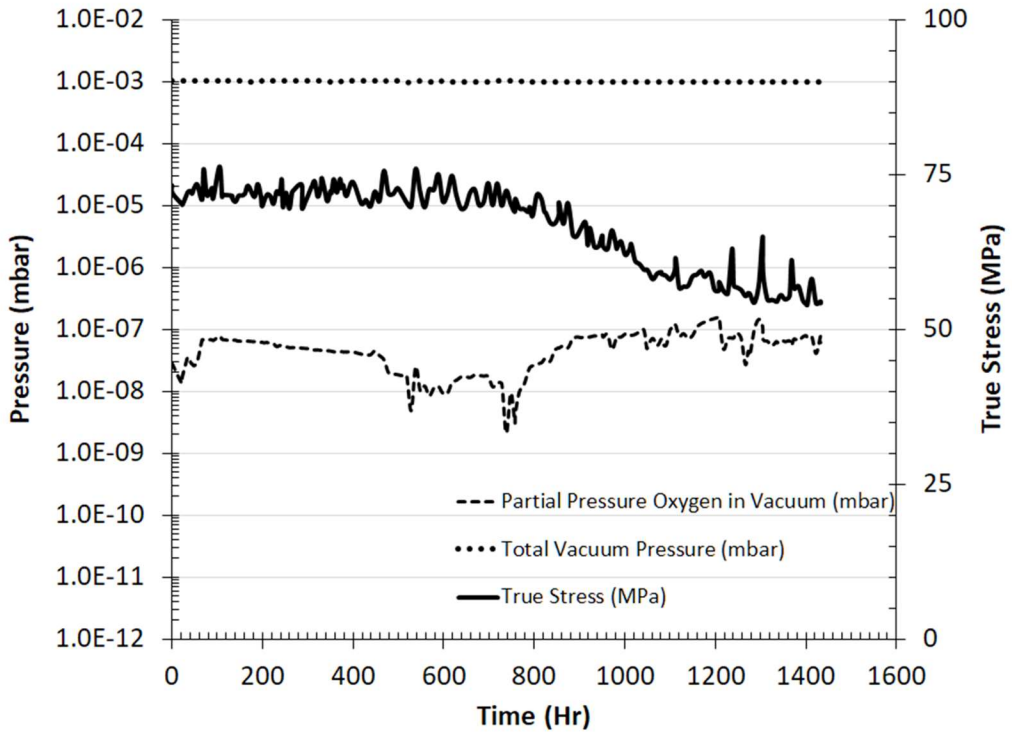

Figure 3.56: 150813b pressure history

Diametral strain vs time history is plotted with the vertical history of sample 150813b in Figure 3.57. It follows the same trends of 150813a in that it appears sensitive to temperature (as seen from the strain rate in hours 790-820).

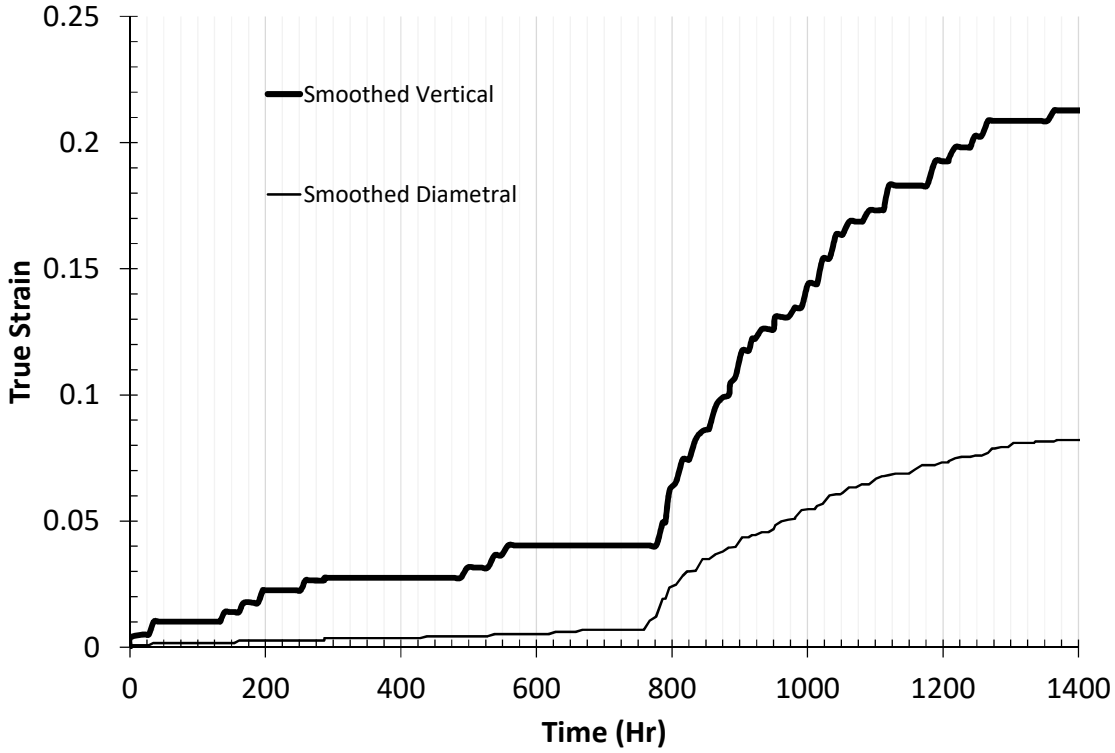

Figure 3.57: 150813b diametral and vertical strain history

This sample was ended early due to a power failure at approximately hour 1400. This was the impetus to install an uninterruptible power supply outlet for the test system.

Sample 161214b

Sample 161214b was the first sample that was tested with the closed loop temperature control installed. The temperature stability is much improved as seen Figure 3.58 via the dashed line and shows the two testing conditions: 900 and 950˚C. The strain rate (the slope of the solid black line) increases due to this change in testing conditions and can be readily seen starting at hour 540.

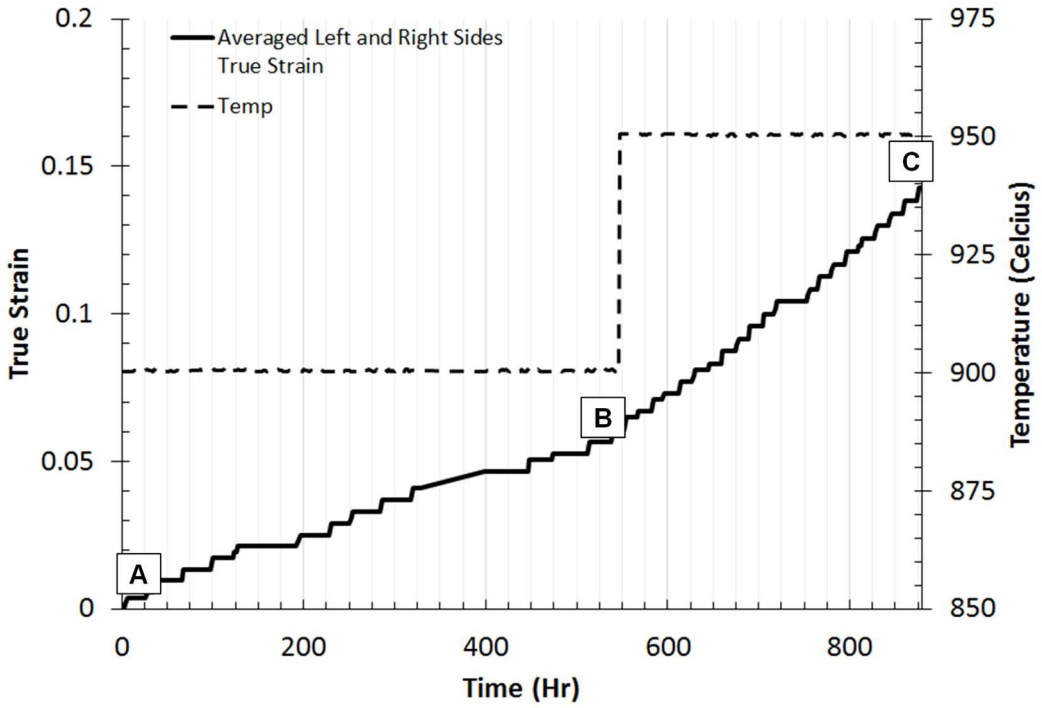

Figure 3.58: 161214b strain time history

Sample 161214b is the longest sample tested. It began to exhibit a noticeable curve as can be seen in Figure 3.59 possibly due to misalignment of the sample or testing platens. Further samples were cut shorter to reduce this effect.

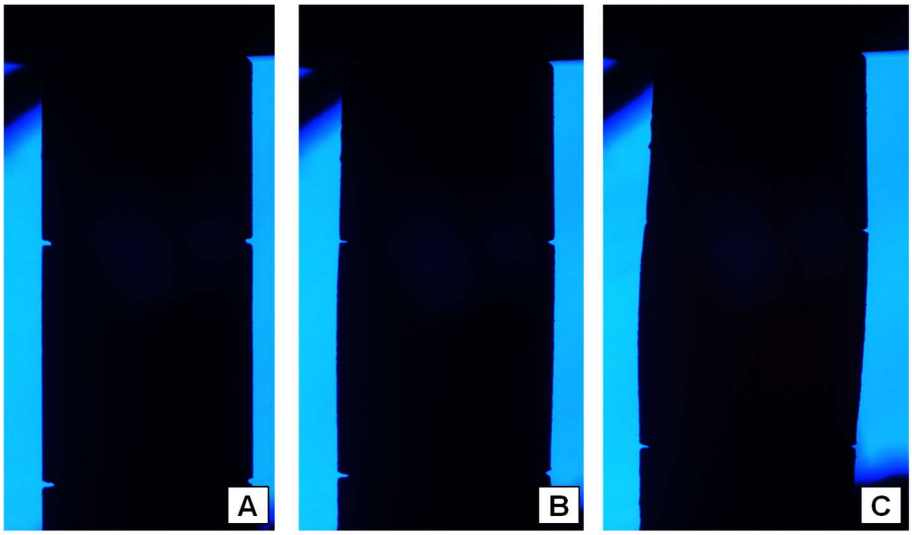

Figure 3.59: 161214b shadow images

Pressures and stress history for 161214b is shown in Figure 3.60. There was one tested stress state (50MPa) and the slow decline is due to the increasing area of the pellet.

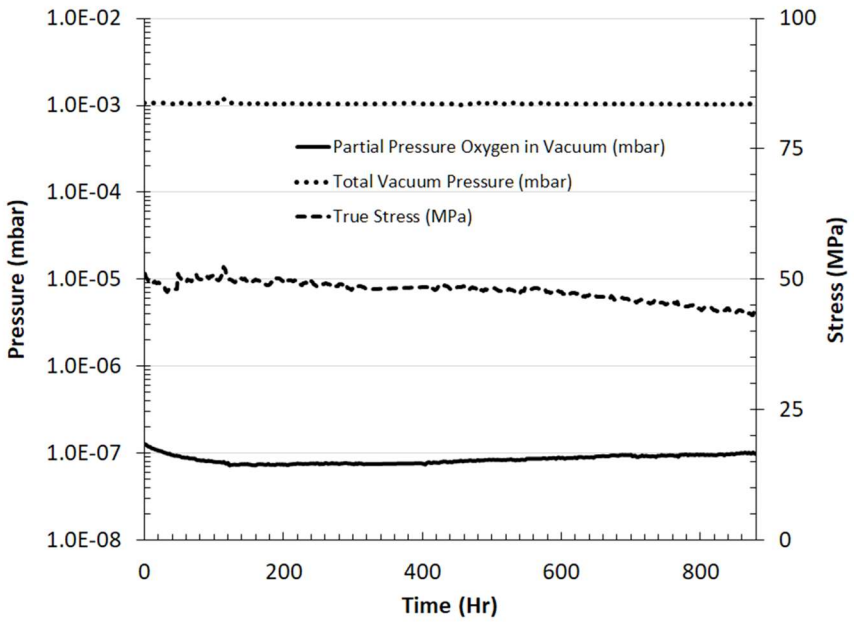

Figure 3.60: 161214b pressure history

The Diametral Strain history is plotted against the vertical history and shows similar behavior to the previous pellets.

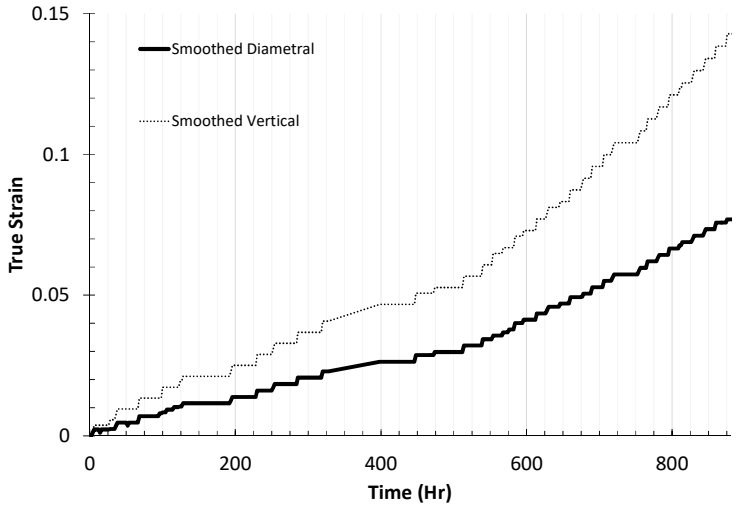

Figure 3.61:161214b Diametral vs Vertical strain history

As stated earlier, the sample began to show a large amount of curvature to it as shown in Figures 59 and 62. The test was stopped early due to concerns that the non-uniform compression state would not be accurate enough of a uniaxial compressive force.

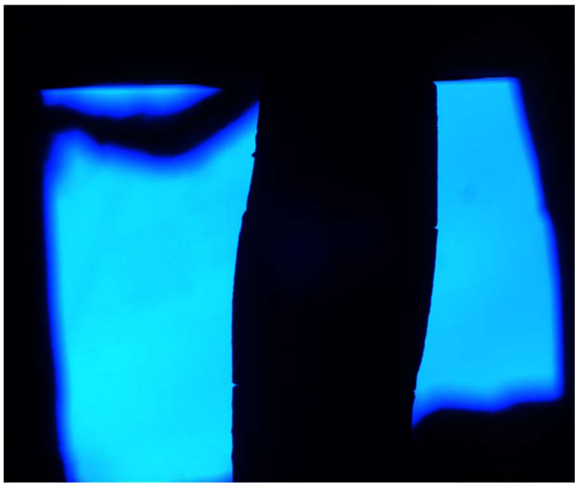

Figure 3.62: Maximum curvature in 161214b at the end of test.

Sample 161214a

Sample 161214a had multiple stress profiles as seen in Figure 3.63. The strain rate (slope of the solid black line) can be seen to readily increase with each step up in stress (dashed line) .

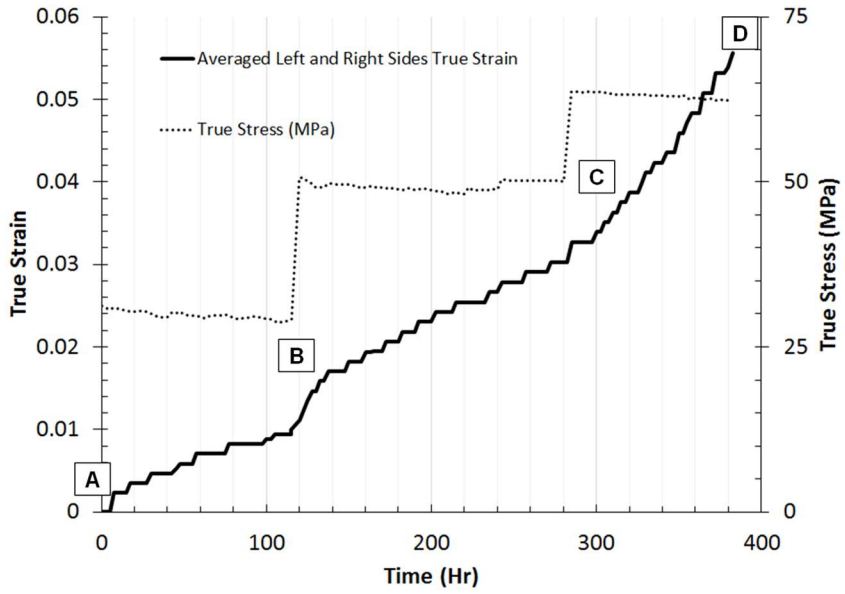

Figure 3.63: 161214a strain time history

The sample was originally longer than tested. The top of the sample was cut off to archive the microstructure of the pellet before creep testing to provide a basis for optical and SEM comparison. As such, the top face of the sample (which is in contact with the compression platen) is not completely square; this can be seen in the red box in Figure 3.64a. However, the sample begins to creep and deform into the platen, essentially seating them with each other.

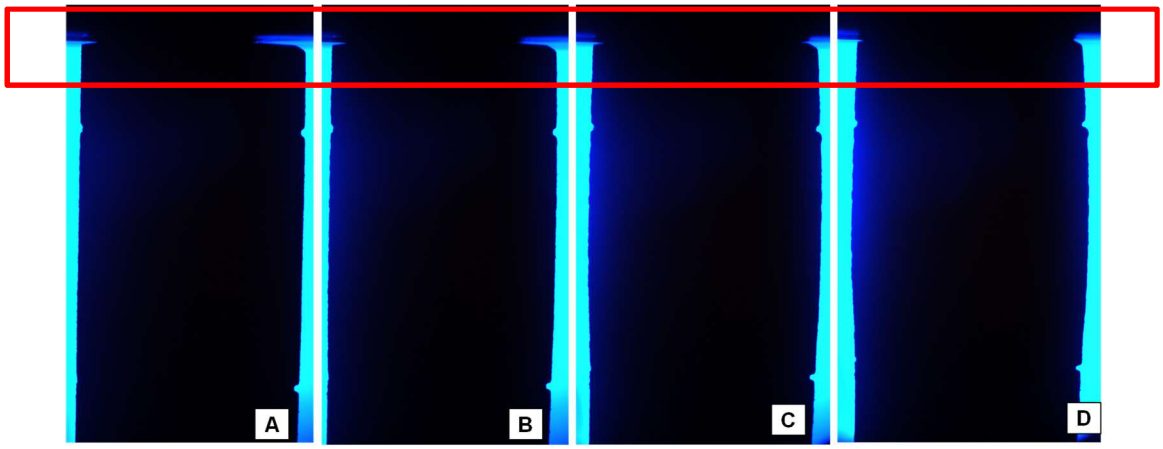

Figure 3.64: 161214a shadow images. The red box highlights the contact area between the sample and the platen

The sample was tested at one temperature, 950˚C, as can be seen in the dashed line in Figure 3.65. The oxygen partial pressure line (solid black line) appears different than previous samples because an extended (three day), high temperature seating process (in where the sample was allowed to deform into the top platen at at least 850C) was done on this pellet before applying the first stress state to account for the un-levelness of the cut face. It is expected that the high temperature environment provides a gettering effect which levels off with enough time.

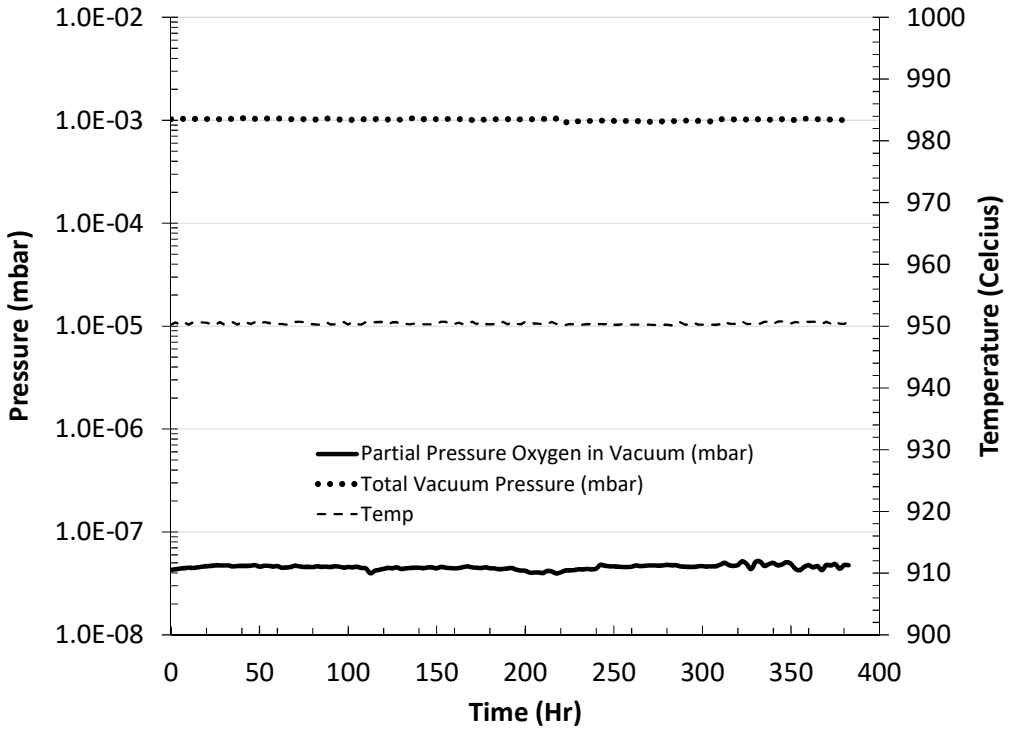

Figure 3.65: 161214a pressure history

The sample showed similar diametral strain behavior compared with the other samples tested as can be seen in Figure 3.66.

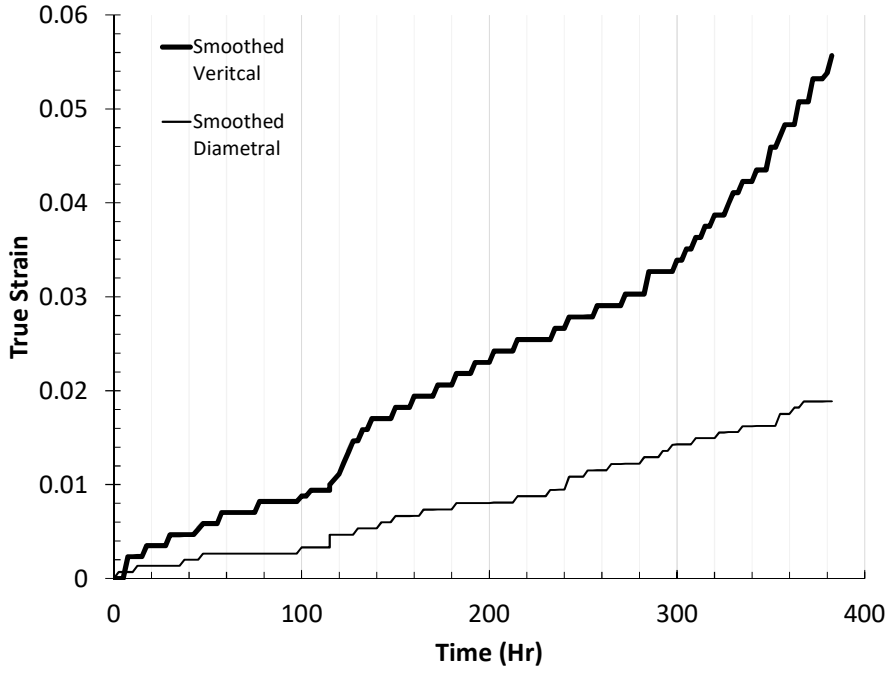

Figure 3.66: 161214a diametral and vertical strain history

A malfunction of the backup power supply installed earlier abruptly stopped the test. The sample cooled down at room temperature but was still under the 65MPa load when this was discovered. However, it was still intact upon unloading.

Sample 161214c

Sample 161214c was the final sample tested in this report. Two stress states were tested as can be seen in Figure 3.67: 28MPa and 48MPa. In addition to the two stress states, two temperature states were tested as can be seen in the dashed line in Figure 3.69, 950 and 1000˚C.

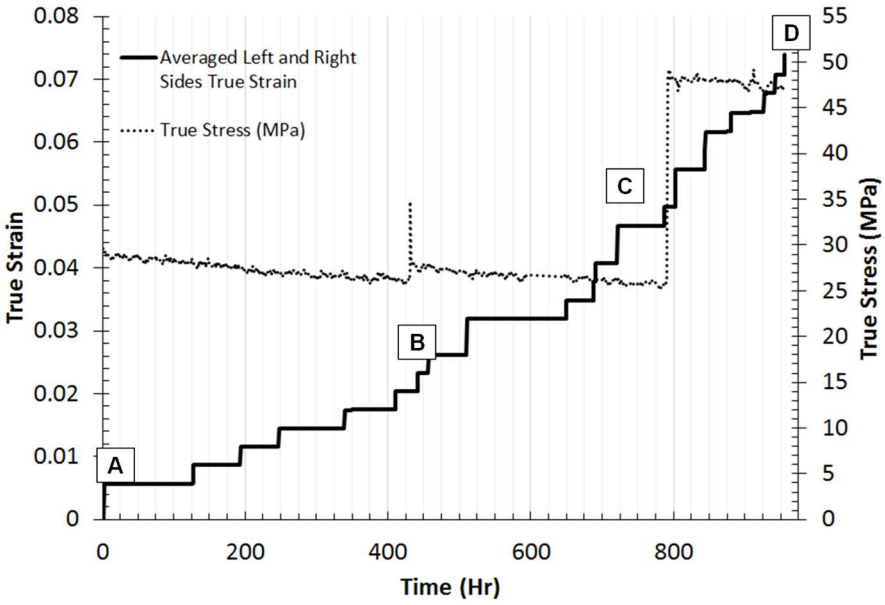

Figure 3.67: 161214c strain time history

The apparent increase in stress at hour 420 is likely due to the stick slip condition between the external metal push rod and the vacuum sealing O-rings as seen in Figure 3.12. At hour 420, the temperature was increased to 1000˚C causing the load frame inside the chamber to thermally expand. The o rings sealing the internal chamber from the outside environment would likely then resist this expansion of the internal load frame. As the load cell is positioned between the thermally expanding hot zone and the friction sealing O rings, it would sense a larger load. This was only a transient effect though because after a short time, the system returns to the previous load.

Shadow images for 161214c are shown in Figure 3.68. The notches on this sample appeared deeper than other samples from the same batch.

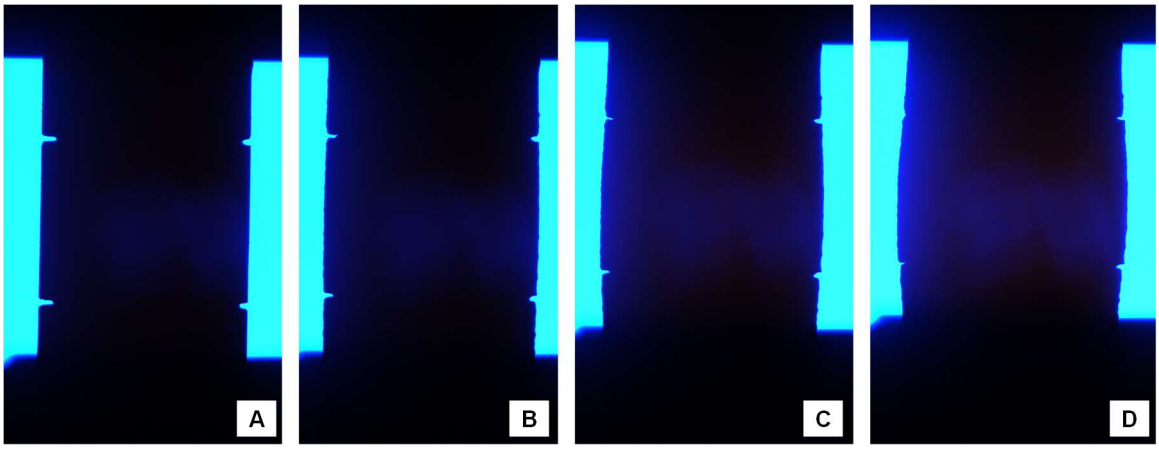

Figure 3.68: 161214c shadow images

The pressures and temperature for this sample are shown in Figure 3.69. There are two temperature conditions tested: 950 and 1000˚C.

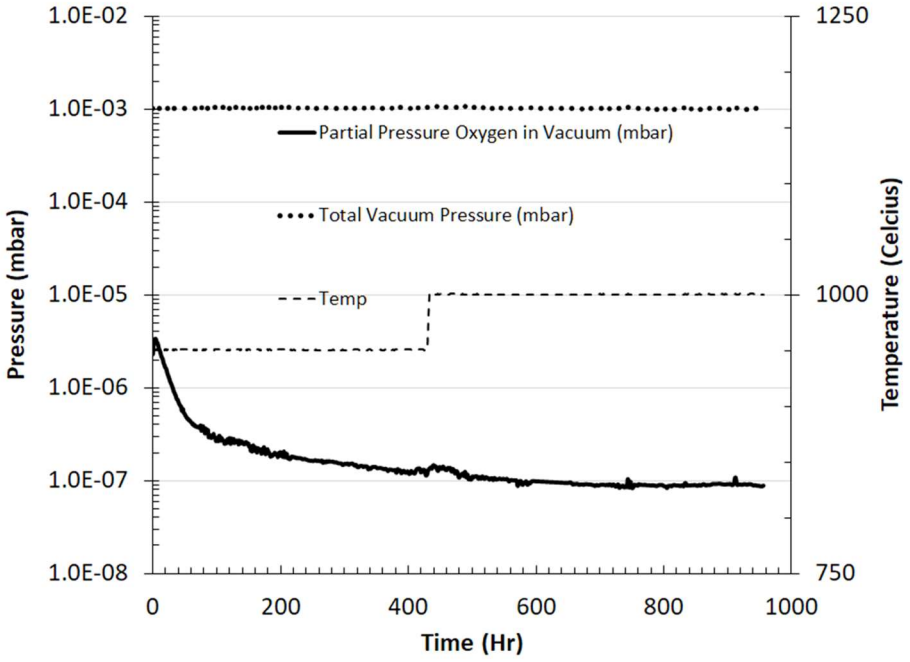

Figure 3.69: 161214c pressure history

The diametral strain vs time is plotted against the vertical strain in Figure 3.70. The diametral strain appears to flat line for the majority of the test even though the vertical strain continues. This may be influenced by the deep notches as seen in the shadow images in Figure 3.68. It appears that the sample first deforms into these notches before expanding outward. However, the very middle of the sample continues to expand but as the automated tracking program relies on the notches as a template, this diametral deformation was not readily captured.

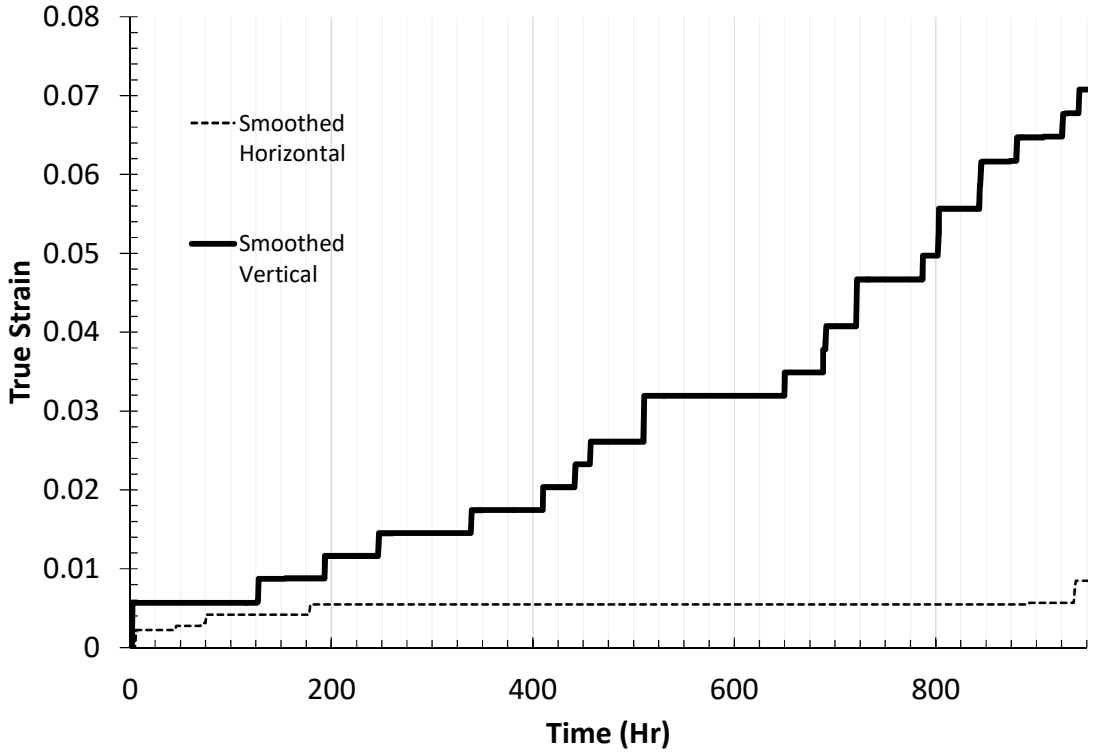

Figure 3.70: 161214c diametral vs vertical strain history

Closed Loop Temperature Control Effect

Closed loop temperature control was not yet implemented for pellets 150813a and 150813b. As such, for the strain-time history data, it appears that there are clear demarcations between primary creep and steady state creep. However, this is believed to be due to the steady drop in temperature after setting an initial temperature. Detailed views of the open loop temperature pellets are shown below.

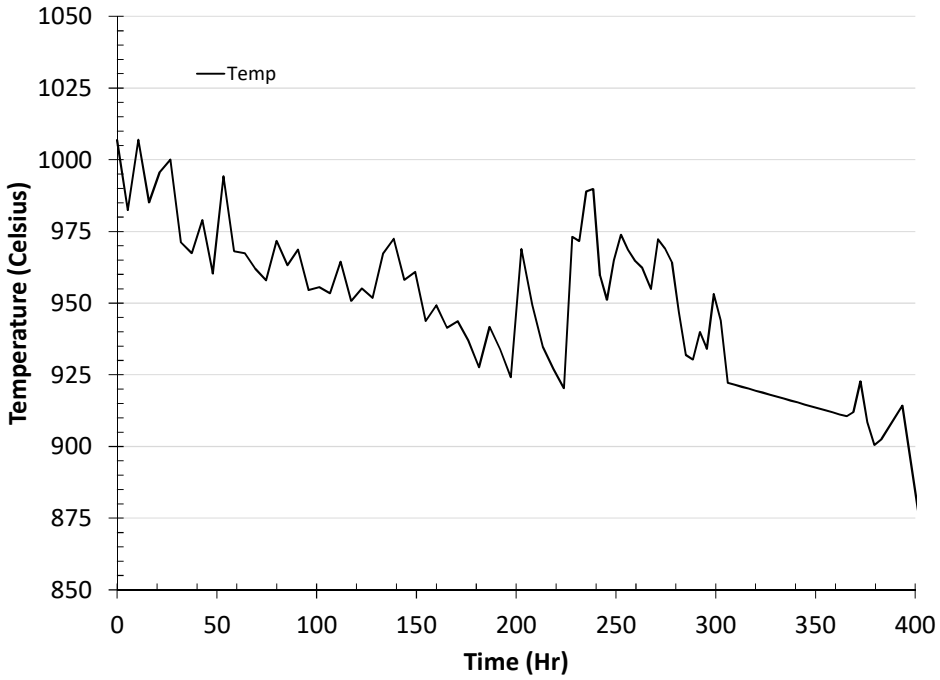

Figure 3.71: 150813a Temperature Detail

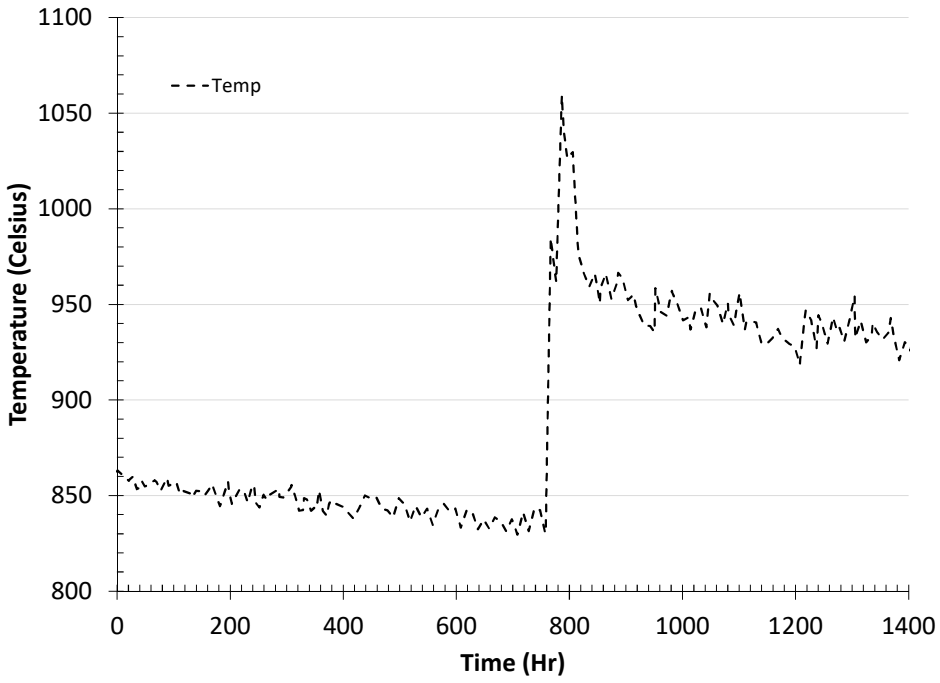

Figure 3.72: 150813b Temperature Detail

Before the implementation of the closed loop controller, temperature conditions were coarsely set via a VARIAC variable transformer. After setting the initial temperature condition, it was observed that the temperature would slowly decrease (~2°C per day) until it reached a steady state temperature. It would then oscillate around this temperature. This steady drop in temperature and oscillation was the impetus to build and implement the temperature controller. However, to account for these effects, the temperature was set to a higher value than the target temperature so that the system would "settle" into the set temperature condition. This effect can be readily seen in Figure 3.73 at hour 800 where the target temperature was 950°C but the system was initially set to 1100°C with the expectation that it would settle down in the 950°C range.

These higher temperature conditions were seen correlate with a faster strain rate as can be seen in the strain-time history plots for pellets 150813a and 150813b in Figures 50 and 54.

For samples 161214b, 161214a, 161214c, the closed loop temperature controller was implemented and provided a more stable temperature testing conditions as seen in Figure 3.74.

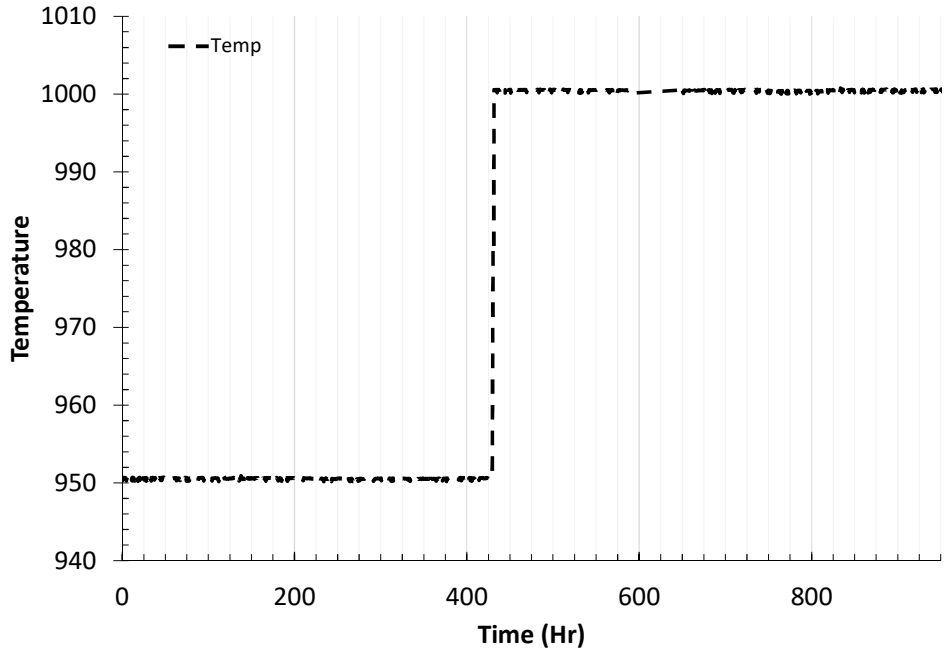

Figure 3.73: 161214c Closed Loop Temperature Detail

All changes in temperature testing conditions with the closed loop temperature box occur at 3°C/minute.

REFERENCES

[1] Zirox Vacuum Probe. http://www.zirox.de/fileadmin/user_upload/datasheets/probes/PI_Vak_eng.pdf

[2] Oerlikon Total Vacuum Probe. http://www.idealvac.com/files/manuals/Leybold-PTR90-Gauge-Specs-Data-Manual.pdf

[3] Lumasense pyrometer. https://www.lumasenseinc.com/uploads/Products/Temperature_Measurement/Infrared_Thermometers/IMPAC_Pyrometers/Series_6/pdf/EN-ISR6-Advanced_Datasheet.pdf

[4] Futek Load Cell Spec Sheet. http://www.futek.com/files/pdf/Product%20Drawings/lcb200.pdf

[5] Edmund Optics. Telecentric Illumination: Why You need it in machine vision applications. https://www.edmundoptics.com/resources/application-notes/imaging/telecentric-illumination-why-you-need-it-in-machine-vision-applications/

[6] Agilent Guide. https://testworld.com/wp-content/uploads/user-guide-keysight-agilent-34970a-34972a-daq.pdf

[7] Opto Engineering Telecentric Lens. http://www.opto-engineering.com/products/TCLWD050

[8] Opto Engineering illuminator. http://www.opto-engineering.com/products/telecentric-HP-illuminator-LTCLHP024-B

[9] Camera Used. https://www.ptgrey.com/grasshopper-5-0-mp-color-firewire-1394b-sony-icx625-camera

[10] Acme FS11000 Transformer. http://www.temcoindustrialpower.com/products/Transformers_-_General/AT1370.html

[11] Hammond Collodial 1182v24 transformer. https://www.hammfg.com/part/1182V24

[12] Prescale pressure film. http://www.fujifilm.com/products/prescale/prescalefilm/\

[13] cvmatvh template plugin. https://sites.google.com/site/qingzongtseng/template-matching-ij-plugin

[14] Inconel Rods. https://www.mcmaster.com/#=1c2yck7

[15] Ceramic Thermal Conduction. https://global.kyocera.com/fcworld/charact/heat/thermalcond.html

[16] True Stress/Strain. http://web.adanabtu.edu.tr/Files/iyilmaz/Duyuru/dosya/ME%20207%20%E2%80%93%20Chapter%203_P3.pdf

[17] Barreling Compression Study. http://research.me.mtu.edu/pubs/Aluko-%20Warm%20Compression%20Tests%20of%20Aluminum%20Alloy.pdf

4. Modeling and Incorporation into BISON

Using data acquired from thirteen compressive creep tests on U_3Si_2, a model of secondary creep was developed. This model was then introduced to the fuel performance code BISON [1] and used in a test case representative of a fuel rod consisting of a U_3Si_2 fuel and composite SiC (SiC/SiC) cladding with a monolithic SiC (mSiC) environmental barrier. The addition of this model to BISON allows for the analysis of the effect of creep during normal operation and pellet-cladding mechanical interaction (PCMI). At the time of this final report, the model for creep is being prepared for submission to the BISON repository for review and addition to the available models for U_3Si_2.

4.1 Methodology

4.1.1. Material Property Models for U_3Si_2

The material properties for U_3Si_2 were first implement in BISON for this work as described in Metzger et al. [2]. These were updated in later models as described below.

Thermal Model

The thermal conductivity of U_3Si_2 is computed using a temperature dependent empirical relation. Whereas Samoilov et al. [3] give a value of 15 W/m-K for the thermal conductivity at room temperature, White et al. provide a range of thermal conductivities as a function of temperature [4]. The most conservative expression for thermal conductivity k (W/m-K) is obtained using the experimental data for White and is therefore used in the BISON thermal model [5]:

$$k = 0.0118T + 4.996$$

where T is temperature in K. This expression is valid for temperatures to 1773 K.

A relationship for the specific heat C_p (J/kg-K) of U3Si2 was also obtained from data collected by White:

$$C_p = 0.02582T + 140.5$$

where T is temperature in K. This expression is valid for temperatures to 1240 K.

Fuel Swelling and Densification Models

Because data for U_3Si_2 is limited, a cumulative burnup-swelling model is suggested. An empirical expression for the swelling of U_3Si_2 was determined using plate fuel data from Ref. 6. Finlay et al. calculated the swelling strain of fuel particles using the results of miniplate irradiation tests. To convert Finlay's data (fission density) to FIMA, a value of 10.735 g/cm^3 was used as the heavy metal density, equivalent to 95% theoretical heavy metal density. Thus, the swelling strain as function of burnup is given as:

$$\frac{V}{V_0}(\%) = 3.88008Bu^2 + 0.79811Bu$$

Within BISON, the volumetric swelling, is calculated by integrating the incremental strain over burnup. The incremental strain for a given burnup step can be written as a function of burnup:

$$\frac{dV/V_o}{dBu} = 7.76016Bu + 0.79811$$

where Bu is the instantaneous burnup in FIMA.

In the absence of data specific to U_3Si_2, the prescribed operating temperatures for U_3Si_2 fuel suggest that it will undergo densification similar to UO_2 fuel. Thus, the fuel densification is calculated using the ESCORE empirical model given by:

$$\varepsilon_D = \Delta\rho_0 \left(e^{\left(\frac{\ln(0.01)Bu}{C_D Bu_D}\right)} - 1 \right)$$

where ε_D is the densification strain, $\Delta\rho_0$ is the total densification that can occur (given as a fraction of theoretical density), Bu is the burnup, and Bu_D is the burnup at which densification is

complete [7]. For temperatures below 750 °C the parameter C_D is given by $7.2 - 0.0086(T - 25)$; above 750 °C it is 1.0 (T in °C).

4.1.2. Thermal Creep Model

Secondary Creep Rate Equation

Secondary creep is described by the standard creep rate equation [8]:

$$\dot{\varepsilon} = A\sigma^n e^{-Q/RT},$$

where A is a material constant, σ is stress, n is the stress exponent, Q is the activation energy, R is the gas constant, and T is absolute temperature. The variables n and Q depend on the creep regime in which the tests are conducted. To obtain A, n, and Q for U_3Si_2, a minimum of three tests must be performed.

Stress Exponent, n

To find the stress exponent n, two creep tests that differ only by the stress applied are needed. Applying the standard creep rate equation to both tests and taking the ratio of the creep rates, an expression for n is obtained:

$$n = \frac{\ln\left(\frac{\dot{\varepsilon}_2}{\dot{\varepsilon}_1}\right)}{\ln\left(\frac{\sigma_2}{\sigma_1}\right)}$$

Activation Energy, Q

To find the activation energy Q, two creep tests that differ only by the temperature of the sample during testing are needed. The ratio of the creep rates gives an expression for Q:

$$Q = \frac{RT_1T_2\ln\left(\frac{\dot{\varepsilon}_2}{\dot{\varepsilon}_1}\right)}{T_2 - T_1}$$

Material Constant, A

The final unknown variable *A* can be solved for by fitting the standard creep rate equation to any of the data points while using the new values for *n* and *Q*.

BISON Test Case

To analyze the effect creep has on the fuel and the cladding during normal operation and PCMI, a test case was created in BISON. The parameters for the test case are outlined in Table 4.1. Here SiC/SiC refers to the ceramic matrix composite of SiC with SiC fibers and mSiC refers to monolithic SiC.

Table 4.1: Parameters for BISON test case

Fuel	U_3Si_2
Cladding	SiC/SiC and mSiC
Pellet Height [2]	11.9 mm
Pellet Diameter	8.2 mm
# of Pellets	10
Pellet Modeling	Smeared
Pellet-Cladding Gap Width	80 μm
Cladding ID	8.36 mm
Cladding OD	10.36 mm
SiC/SiC Thickness [9]	0.8 mm
mSiC Thickness[9]	0.2 mm
Length of Initial Ramp to Power	1.0E4 s
Linear Heating Rate Over 54 Months[9]	36.1-25.9 kW/m
Coolant Pressure [9]	15.0 MPa
Coolant Temperature [9]	589.0 K
Initial Plenum Pressure [9]	2.0 MPa

4.2 Results

The results from the compressive creep testing are outlined in Table 4.2.

Table 4.2: Results from compressive creep testing (* denotes tests that failed to meet the requirements that were set for analysis)

Creep Test	Pellet ID	True Stress (MPa)	Temperature (K)	Creep Rate (1/s)
1	150813a	44.10	1218.37	8.7327×10^{-8}
2	150813a	71.77	1205.18	1.1134×10^{-7}
3*	150813a	N/A	N/A	N/A
4	150813b	77.68	1122.24	1.9769×10^{-8}
5	150813b	57.69	1210.10	5.2848×10^{-8}
6	161214b	46.81	1173.58	1.9071×10^{-8}
7	161214b	45.65	1223.59	4.6836×10^{-8}
8*	161214a	N/A	N/A	N/A
9	161214a	49.43	1223.56	2.8543×10^{-8}
10*	161214a	N/A	N/A	N/A
11	161214c	27.36	1223.70	1.1998×10^{-8}
12	161214c	26.40	1273.60	1.8869×10^{-8}
13	161214c	47.77	1273.61	2.9740×10^{-8}

To determine which tests meet the criteria to calculate n and Q, a standard was created that considers temperatures to be equal when they differ by less than 20 K and stresses to be equal when they differ by less than 15 MPa. Using the methods outlined in the previous section, the following average values for A, n, and Q were obtained:

Table 4.3: Calculated values for A, n, and Q.

A	n	Q (kJ/mol)
2.5544×10^{-22}	2.3480	88.87

Figure 4.1 shows the values projected by the creep model compared to the measured values. Points that lie on, or close to, the black line on the figure show that the model agrees with the measured data.

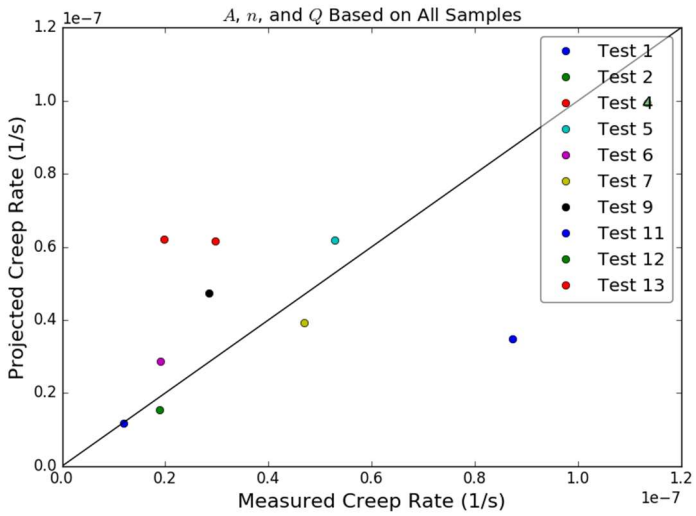

Figure 4.1: Projected versus measured creep rate.

Using an earlier model based on a smaller sample of data that provides values for A, n, and Q of 2.0386×10^{-4}, 1.2063, and 295.55 kJ/mol, the results from the case outlined in Table 4.1 were compared to those of the same run without creep. These results can be seen in Figures 4.2-4.7.

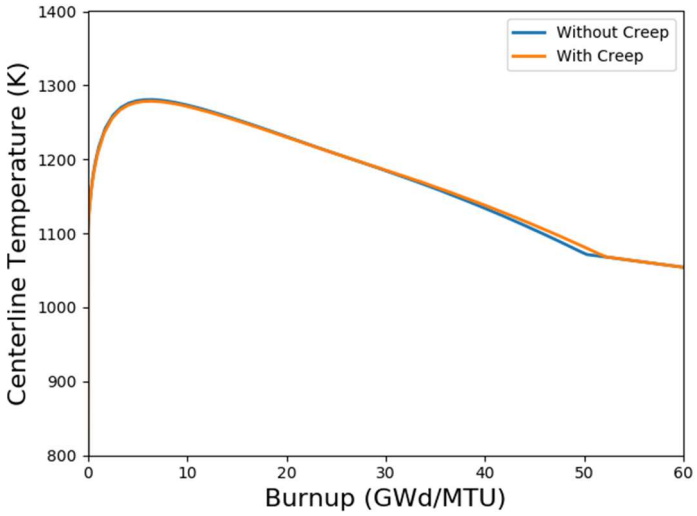

Figure 4.2: Centerline temperature for U_3Si_2/SiC with and without creep.

Figure 4.2 shows the centerline temperature of U_3Si_2 for both cases. The temperature reaches a maximum value at the end of the initial ramp to power, then begins to decrease due to

the decreasing linear heat rate and the closure of the pellet-cladding gap due to the volumetric swelling of the fuel. At roughly 50-52 GWd/MTU, a bend can be seen in the temperature profile. This occurs when the fuel has come into contact with the cladding, which is typically referred to as pellet-cladding mechanical interaction (PCMI). During PCMI, there is direct heat transfer from the fuel to the cladding due to the absence of the gap. The continued decrease in temperature beyond PCMI is solely due to the constantly decreasing linear heat rate. Figure 4.2 also shows there is only a slight difference in the two cases at the point of contact. This difference can be explained by the divergence of fuel surface radial displacement as seen in Figure 4.4. At ~30 GWd/MTU, the fuel begins to creep inward, causing the gap to remain open longer. As a result of the gap staying open longer, PCMI is postponed and the heat from the fuel cannot be directly transferred to the cladding.

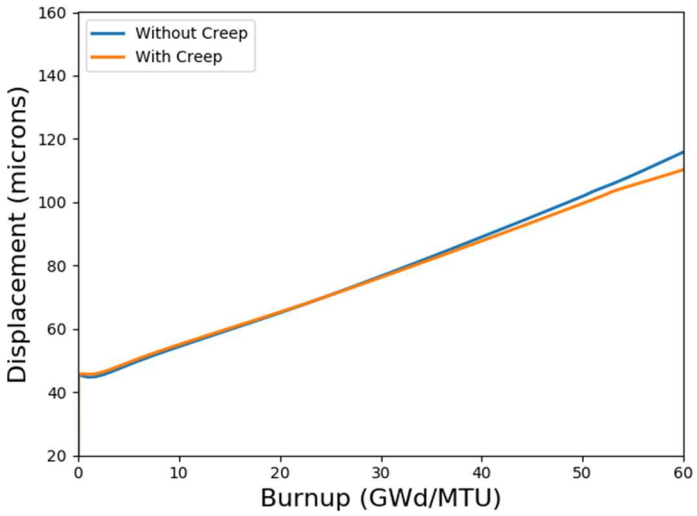

Figure 4.3: Radial fuel surface displacement for U_3Si_2/SiC with and without creep.

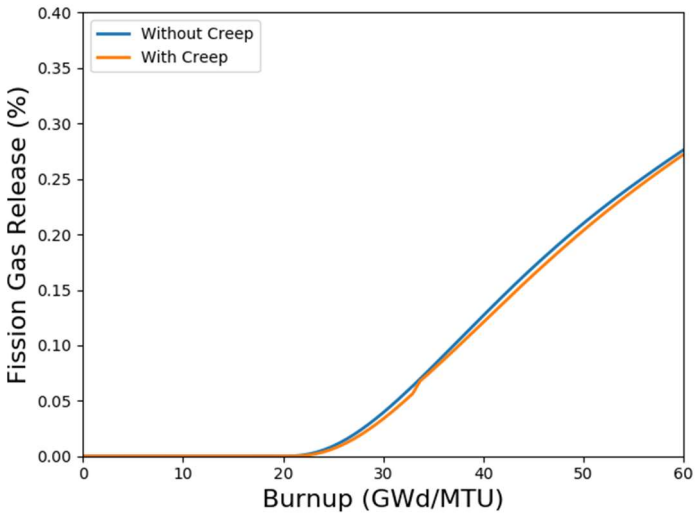

Figure 4.4: Fission gas release for U_3Si_2/SiC with and without creep.

Figure 4.4 shows that the amount of fission gas release remains relatively small (< 0.3%), which means the increase in internal pressure of the fuel rod in Figure 4.5 is due mostly to the volumetric swelling of the fuel closing the plenum. Since the fuel is extending further into the plenum due to creep, there is a significant reduction in plenum volume which causes the increase in internal pressure seen in Figure 4.5.

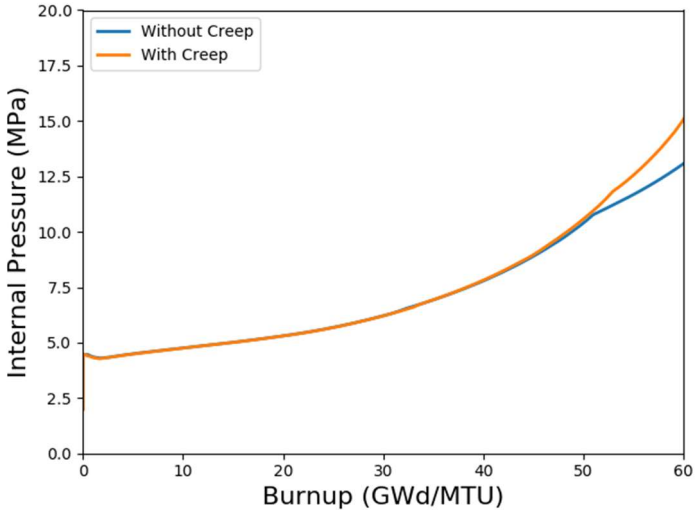

Figure 4.5: Internal pressure for U_3Si_2/SiC with and without creep.

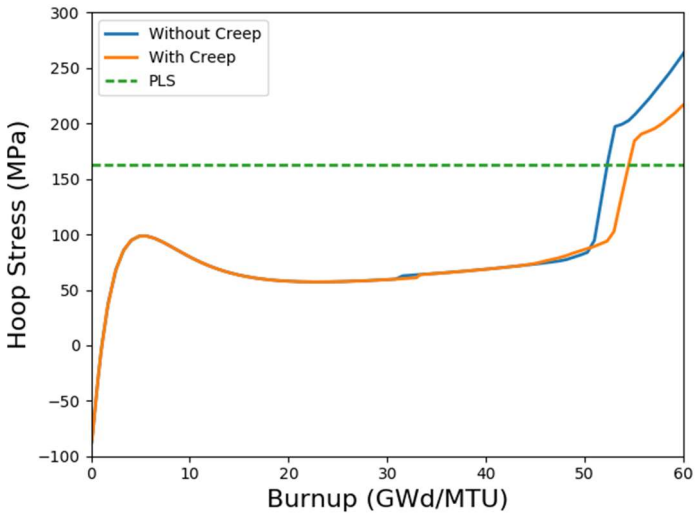

Figure 4.6: Average hoop stress in the composite portion for U_3Si_2/SiC with and without creep.

One of the most significant impacts of creep can be seen in Figures 4.6 and 4.7. Due to the high stresses that are present during PCMI, the stress dependent creep rate increases greatly. The fuel creeping inward reduces the stresses on the cladding, allowing the fuel to reach 60 GWd/MTU without reaching the fracture stress of the monolithic portion of the cladding, as can be seen in Figure 4.7. Since the composite portion of the cladding is very porous, a fracture in the monolithic layer will provide an unobstructed path between the fuel and the coolant.

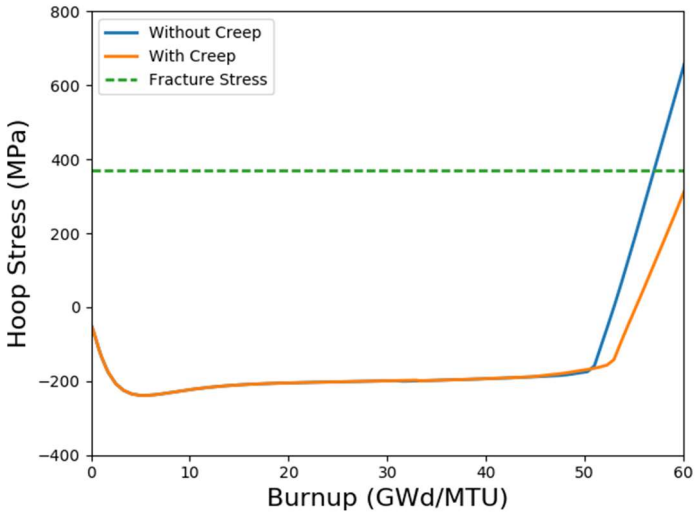

Figure 4.7: Average hoop stress in the monolithic portion for U_3Si_2/SiC with and without creep.

4.3 References

[1] Williamson, R. L., Gamble, K. A., Perez, D. M., Novascone, S. R., Pastore, G., Gardner, R. J., Hales, Liu, W., J. D, Mai, (2016). Validating the BISON fuel performance code to integral LWR experiments. *Nuclear Engineering and Design*, *301*, 232-244.

[2] Metzger, K. E., Knight, T. W., & Williamson, R. L. (2014). Model of U3Si2 fuel system using BISON fuel code. *ICAPP 2014, Charlotte, NC, USA, Apr. 6–9*.

[3] A. G. SAMOILOV, A. I. KASHTANOV, and V. S. VOLKOV, *Dispersion-Fuel Nuclear Reactor Elements.* Jerusalem: Israel Program for Scientific Translations. (1965). Engl. Translation: Aladjem (1968).

[4] J. T. White, A. T. Nelson, J. T. Dunwoody, D. D. Byler, D. J. Safarik, and K. J. McClellan. "Thermophysical properties of u3si2 to 1773 K". *Journal of Nuclear Materials*, **464**, 275-280 (2015).

[5] K. Gamble and J. Hales. "Development and validation of accident models for u3si2." *Technical Report*, Idaho National Laboratory (2016)

[6] M. R. FINLAY, G. L. HOFMAN, and J. L. SNELGROVE. "Irradiation behaviour of uranium silicide compounds". *Journal of Nuclear Materials*, **325**, *Issues 2-3,* 118–128 (2004).

[7] Y. RASHID, R. DUNHAM, and R. MONTGOMERY. "Fuel analysis and licensing code: FALCON MOD01." *Technical Report EPRI 1011308*, Electric Power Research Institute, February (1987).

[8] Murty, K. L. (Ed.). (2013). *Materials Ageing and Degradation in Light Water Reactors: Mechanisms and Management*. Elsevier.

[9] Stone, J. G., Schleicher, R., Deck, C. P., Jacobsen, G. M., Khalifa, H. E., & Back, C. A. (2015). Stress analysis and probabilistic assessment of multi-layer SiC-based accident tolerant nuclear fuel cladding. *Journal of Nuclear Materials*, *466*, 682-697.

5. CHARACTERIZATION OF U_3Si_2 SAMPLES

5.1 INTRODUCTION:

The University of South Carolina (USC) has completed characterization on U_3Si_2 produced at Idaho National Laboratory (INL). Completed characterization includes; optical microscopy with pore and grain size analysis, helium pycnometry for density determination, mercury intrusion porosimetry, compositional analysis in the form of XRD, second phase identification using EDX, electrical resistance measurement via four-point probe, determination of hardness and toughness through Vickers indentation testing, and determination of elastic properties using the impulse excitation method.

5.2 U3SI2 SAMPLES

The U_3Si_2 samples used in characterization and testing came from one of three different lots (Figure 5.1). The sample dimensions are summarized in Table 1 and Sintering details are provided in Table 5.2. The pressed U_3Si_2 green bodies were first heated to 600°C in order to burn off binders. Any differences in microstructure between the U_3Si_2 samples should be attributed to differences in the temperature and duration of second sintering step as well as the feedstock particle size distribution.

The first lot was comprised of Pellets A, B, and C. The pellets were fabricated with varying feed stock particle size distributions and sintering conditions in order to study the effect on microstructure. The feedstock particle size distributions for each

pellet are shown in Figure 5.2 (adapted from [Harp 2015]). Pellet C has a microstructure representative of the U_3Si_2 pellets that will be used in the first round of experimental testing within the advanced test reactor (ATR) and was the basis for U_3Si_2 samples used in this work. All pellets were sintered in an Argon atmosphere furnace. Additional fabrication details are provided in [Harp 2015]. Pellets A, B, and C were used for optical grain and pore size analysis, gas pycnometry, XRD and EDX. Following all other characterization, the pellets were mounted in epoxy and used for indentation testing as well as 4-point probe resistivity testing. A summary of all characterization and testing performed on each sample time is provided in Table 5.3.

The second lot of samples was comprised of three tile specimens. These tiles were fabricated using the same feed stock particle size distribution as that of Pellet C but were sintered in a vacuum furnace. Of the three specimens, only one tile remained intact during shipment. This sample was used for impulse excitation testing. Of the two remaining tile samples, one was broken in half and the other had a chip in it. The fractured sample was cut into quarters, mounted in epoxy, and used for grain size analysis, pore size analysis, and indentation testing. SEM imaging of the indentations allowed for additional EDX analysis. The chipped tile was mounted in epoxy and used for 4-point probe resistivity testing.

The final lot of samples consisted of eight pellets of varying length (all same diameter) supplied for compression creep testing. The creep pellets were fabricated using the same feed stock particle size distribution as that of Pellet C and tile samples and were sintered in a vacuum furnace. These pellets were notched on the sides using an EDM in order to produce topographical features to aid in strain detection during creep testing. One of these pellets was used for grain and pore size analysis, gas pycnometry, and mercury intrusion porosimetry.

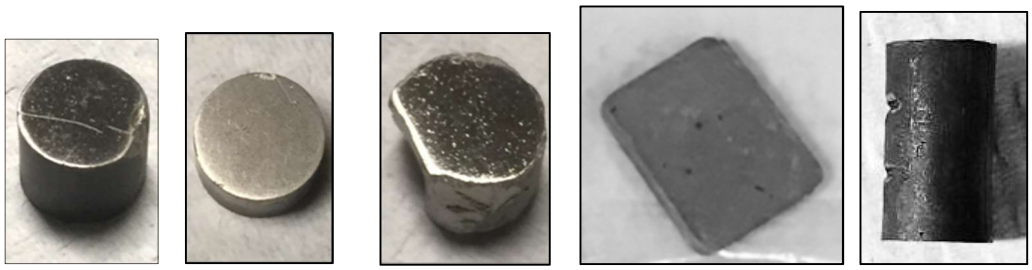

Figure 5.1: (Left to Right) Pellet A, B, and C, U_3Si_2 tile, and creep pellet.

Table 5.1: Sample dimensions

	As-Received Dimensions (mm)
Pellets A, B, C	length= 6.5 mm, diameter = 8.0 mm
Tile Samples	length= 20.5 mm, width = 15.7 mm, thickness = 3.0 mm
Creep Pellet	length= 9.9 mm, diameter = 5.5 mm

Table 5.2: Sintering details and conditions

	Sintering Conditions
Pellet A	sintered at 600°C for 2 hours & 1450 °C for 4 hours (Argon furnace)
Pellet B	sintered at 600°C for 2 hours & 1450 °C for 4 hours (Argon furnace)
Pellet C	sintered at 600°C for 2 hours & 1500 °C for 4 hours (Argon furnace)
Tile Specimen	sintered at 600°C for 2 hours & 1400 °C for 8 hours (Vacuum furnace)
Creep Pellet	sintered at 600°C for 2 hours & 1500 °C for 4 hours (Vacuum furnace)

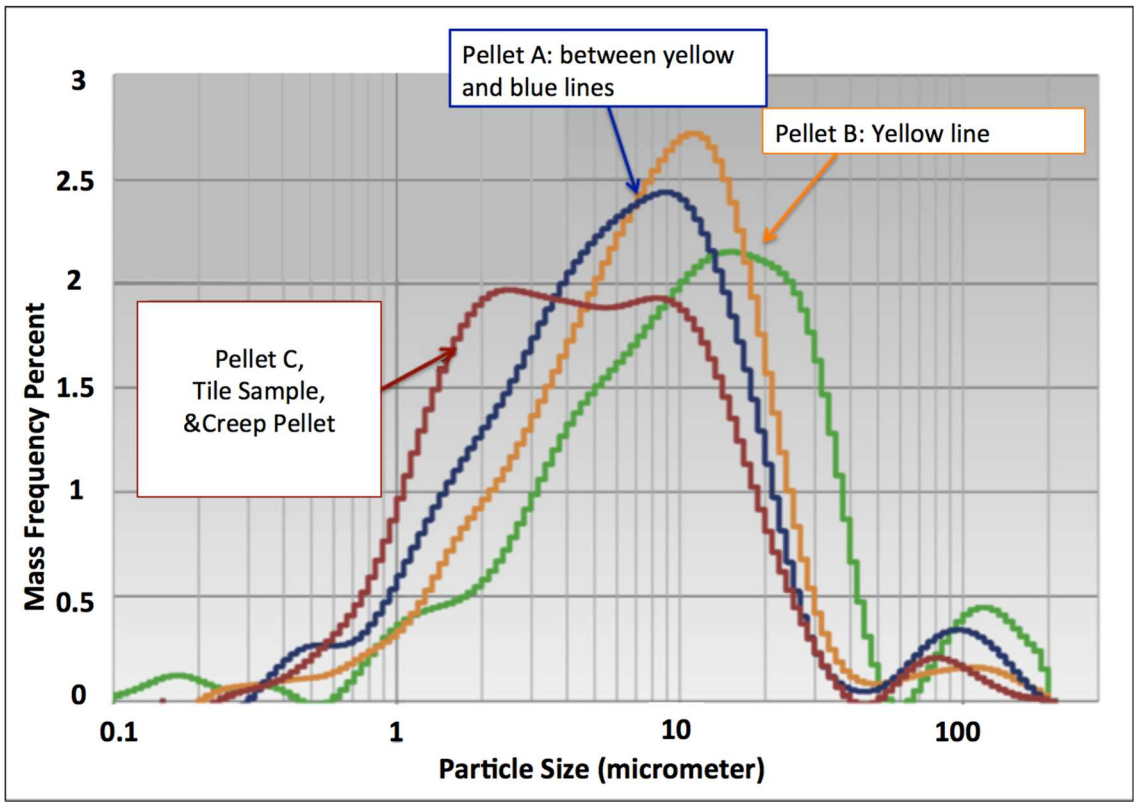

Figure 5.2: Feedstock particle size distributions for U_3Si_2 samples. Tile samples and creep pellet samples were made using the same feedstock as that of Pellet C.

Table 5.3: Summary of characterization and testing performed on each U_3Si_2 sample

	Grain Size Analysis	Porosity Analysis (Optical Microscopy)	Gas Pycnometry	Mercury Porosimetry	XRD	EDX	4-point Resistivity Testing	Vickers Indentation	Impulse Excitation Testing
Pellet A	◆	◆	◆		◆	◆	◆	◆	
Pellet B	◆	◆	◆		◆	◆	◆	◆	
Pellet C	◆	◆	◆		◆	◆	◆	◆	
Tile Sample	◆	◆				◆	◆	◆	◆
Creep Pellet	◆	◆	◆	◆		◆			

5.3 Sample Preparation:

Samples were freshly polished prior to each type of characterization.

Each sample was polished using a sequence of SiC grinding disks with progressively finer grit (240, 400, 600, 800, 1200) at 5 minutes each. Samples were then polished using 9μm, followed by 1μm diamond paste on a LeCloth polishing disk at 10 minutes each.

Samples were mounted in a high strength epoxy for resistivity and indentation testing. The tile sample was used as-sintered for impulse excitation testing.

It should be noted that Pellet C was fractured using a mortar and pestle and attempt was made to grind the fragment into powder for powder X-ray diffraction (PXRD). The fragment was pyrophoric and oxidized heavily when mechanical energy was used to crush the sample. Since the powder was oxidized, XRD was instead performed on a polished surface of each pellet sample.

5.4 Grain Size Analysis:

Los Alamos National Laboratory (LANL) was able to reveal grains of highly polished U_3Si_2 without the use of an etchant using polarized light microscopy. [White 2015] The average grain size was found to be approximately 35 μm in diameter. A polarized light contrast system (polarizer and analyzer) was acquired for the University of South Carolina's (USC) Keyence optical microscope in order to replicate LANL's imaging technique. Each pellet was polished using a1 μm diamond-polishing compound as the final step. When the pellets were examined with polarized light microscopy, grain boundaries could not be observed. This motivated the use of chemical etching to reveal grain boundaries.

Uranium silicide literature was reviewed for chemical etching techniques; however, the etching details for U_3Si_2 are limited. Taylor and McMurtry's work on refractory uranium compounds references nitric acid or a nitric acid mixture as an etchant in two separate reports. The summary report on refractory uranium compounds includes a micrograph image of grain

boundaries in U_3Si_2 [Taylor 1961]. The corresponding Figure description states that a Nitric acid-Acetic Acid-Water etchant was used. No other details concerning the etchant concentration or application technique are provided. In a related quarterly report, Taylor states, "etching with nitric acid showed what appeared to be small cracks in the U_3Si_2 grains filled with an unetched phase, presumable free silicon."[Taylor 1960] Again, no additional details concerning the concentration of the acid or application procedures are given. The Smithells Metals Reference Book discusses chemical etching of uranium and uranium alloys. [Gale 2003] The book suggests a solution of 50cc Nitric acid to 100cc water and says that etching may take between 15 and 45 minutes. Since the concentration of nitric acid is not explicitly stated in the book, it is assumed that the authors meant the standard concentration of HNO_3, 67 w/v%. Additionally, the book states that chemical etching alone does not sufficiently reveal grain boundaries in some uranium compounds. In such cases, polarized light microscopy must be used in addition to chemical etching.

Chemical Etching at USC:

Given the information in the literature, diluted nitric acid (20 w/v%) was selected to etch U_3Si_2 pellets at USC. Care was taken to prevent overetching and pitting of the pellets. The nitric acid was swabbed onto the surface and lightly massaged into the pellet surface using the end of the cotton swab. At the outset, samples were etched in increments of 30- 60 seconds before being washed with deionized water. After each application, the pellet surface was observed using polarized light microscopy. The appearance of the microstructure informed the length of time for the next incremental etching. Table 5.4 is a timeTable for the application of Nitric acid to the surface of each pellet. For a given pellet, each row indicates the incremental etching time as well as the total time.

The etching of pellets A and C proceeded reasonably well and after approximately 20 minutes, each pellet was sufficiently etched to the point that grain boundaries were clearly visible with polarized light microscopy. On the other hand, after 10.5 minutes of etching Pellet B (a final application of 5 minutes), the surface began to develop a bluish tint. It was determined that the sample had likely been overetched. For pellets A and C, the application of nitric acid for 5 minutes yielded good results and did not overetch the pellet surfaces. Given that Pellet B was the most porous of the three pellets, it is believed the nitric acid seeped into the pores and accelerated the etching process. The surface of Pellet B was repolished to remove the pitting and surface staining so that etching could be resumed in shorter increments of time.

Given that the tile shaped specimens and creep pellet samples have microstructures like that of Pellet C, those samples were etched using the etching schedule for Pellet C. The incremental etchant application time can be increased to expedite the process; however, precaution should be taken in increasing the etching time given the possibility of overetching.

Table 5.4: Etching time details for U_3Si_2 pellets

	Time etched (Increment and Total Time)					
Date of Etch	**Pellet A**		**Pellet B**		**Pellet C**	
	Etched Time	Total	Etched Time	Total	Etched Time	Total
5/28/15	**60**	**60**	**30**	**30**	**30**	**30**
	90	**150**	----	----	**30**	**60**
	90	**240**	----	----	**60**	**120**
	----	----	----	----	**60**	**180**
6/1/15	**120**	**360**	----	----	----	----
	120	**480**	----	----	----	----
	120	**600**	----	----	----	----
	150	**750**	----	----	----	----
6/2/15	**300**	**1050**	----	----	----	----
6/4/15	**60**	**1110**	**300**	**330**	**120**	**300**
	----	----	**300**	**630**	**120**	**420**
	----	----	----	----	**120**	**540**
	----	----	----	----	**120**	**660**
6/8/15	**120**	**1230**	**Polished again**		**180**	**840**
	120	**1350**	**120**	**120**	**300**	**1140**
	----	----	**120**	**240**	----	----
	----	----	**120**	**360**	----	----
	----	----	**180**	**540**	----	----
	----	----	**120**	**660**	----	----
	----	----	**180**	**840**	----	----
	----	----	**300**	**1140**	----	----
6/11/15	----	----	**120**	**1260**	----	----
	----	----	**120**	**1380**	----	----
	----	----	**60**	**1440**	----	----
	----	----	**60**	**1500**	----	----
	----	----	**60**	**1560**	----	----
	----	----	**60**	**1620**	----	----
	----	----	**60**	**1680**	----	----
	----	----	**60**	**1740**	----	----
	----	----	**60**	**1800**	----	----
	----	----	**90**	**1890**	----	----
	----	----	**90**	**1980**	----	----
	----	----	**60**	**2040**	----	----
Totals (6/11/15):	**22.5 min**		**34 min**		**19 min**	

Microscopy:

After every acid application, the pellets were imaged. The following images show the ultimate grain structure of each sample. Each image was obtained using a polarized light filter.

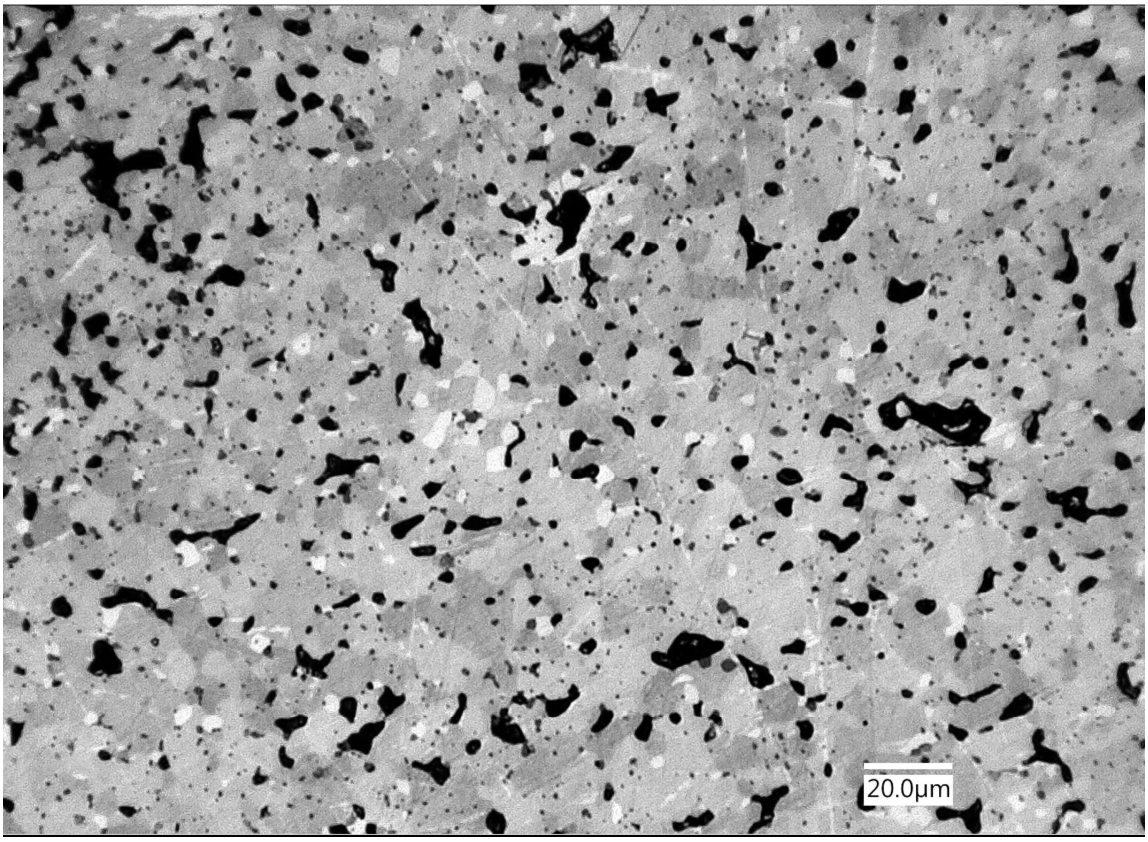

Figure 5.3: Micrograph of Pellet A at 1000x magnification. (etched 22.5 minutes)

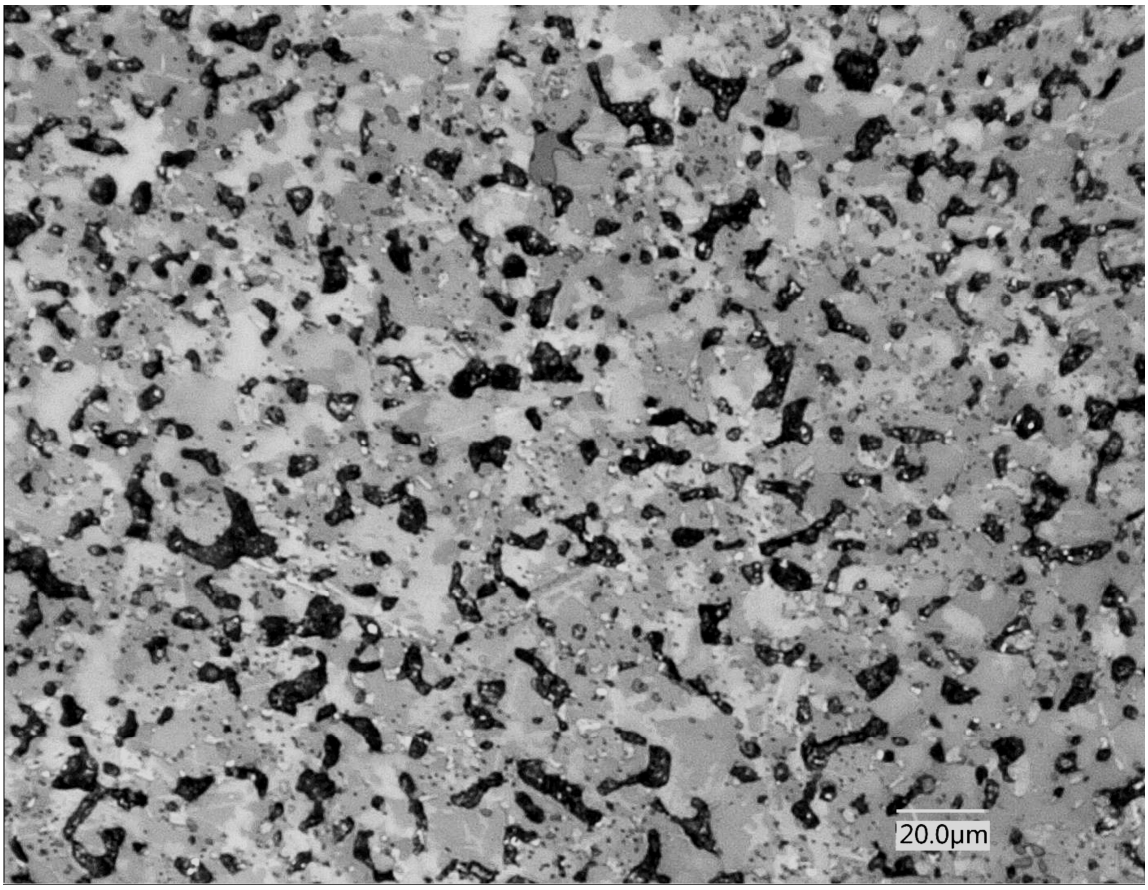

Figure 5.4: Micrograph of Pellet B at 1000x magnification. (etched 34.5 minutes)

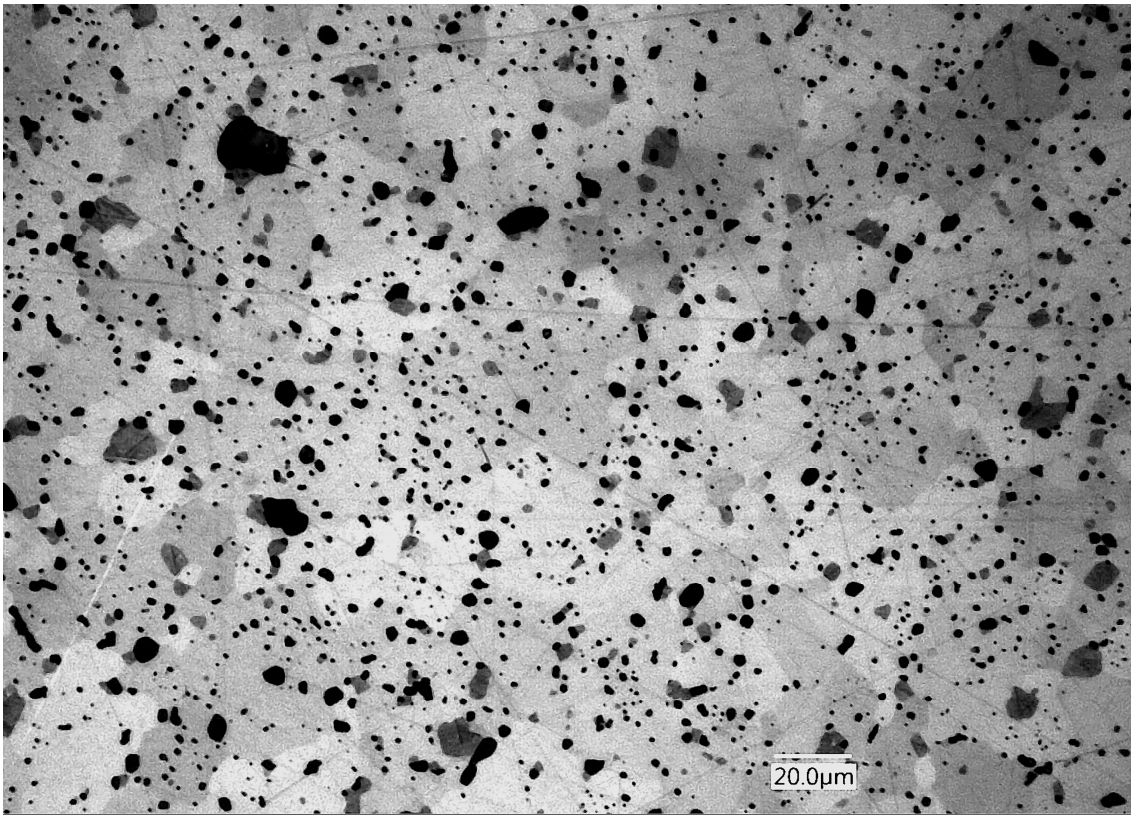

Figure 5.5: Micrograph of Pellet C at 1000x magnification. (etched 19 minutes)

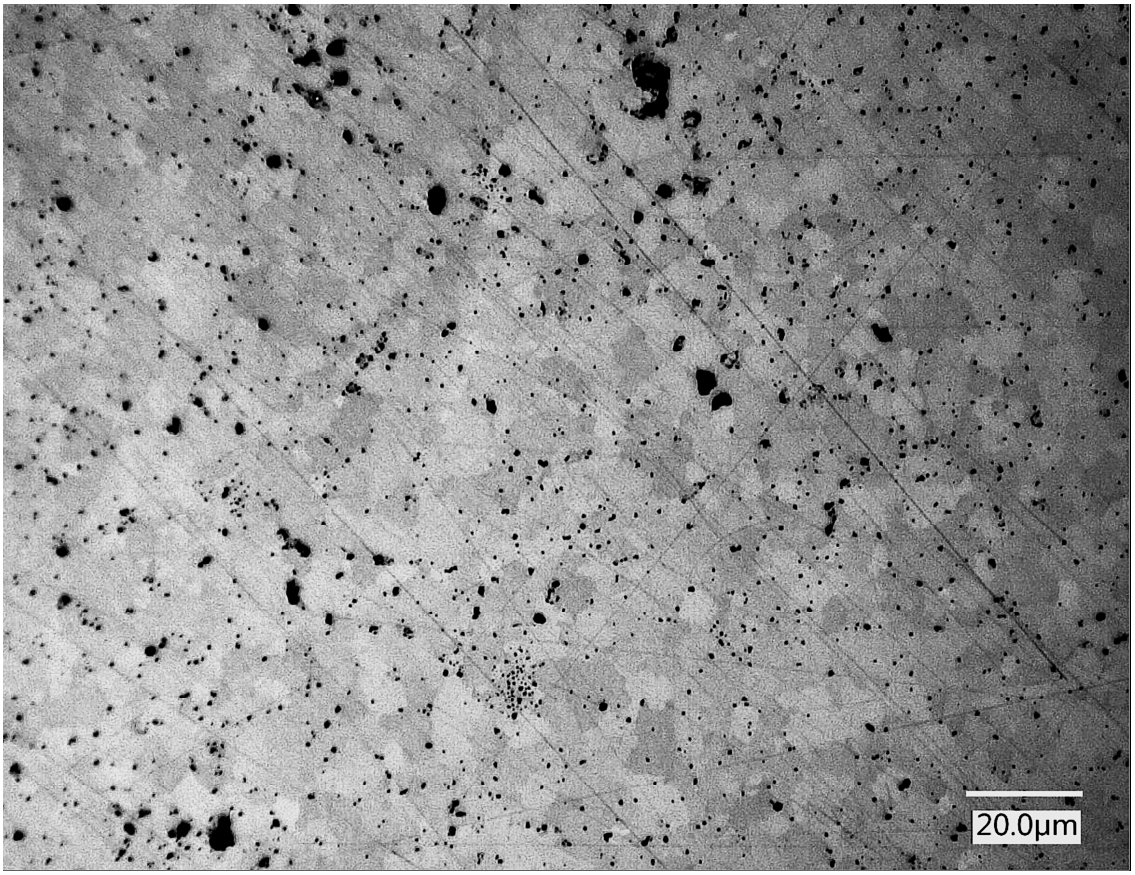

Figure 5.6: Micrograph of Tile Sample at 500x magnification. (Incremental etching times were increased so total etch time was reduced to 12 minutes)

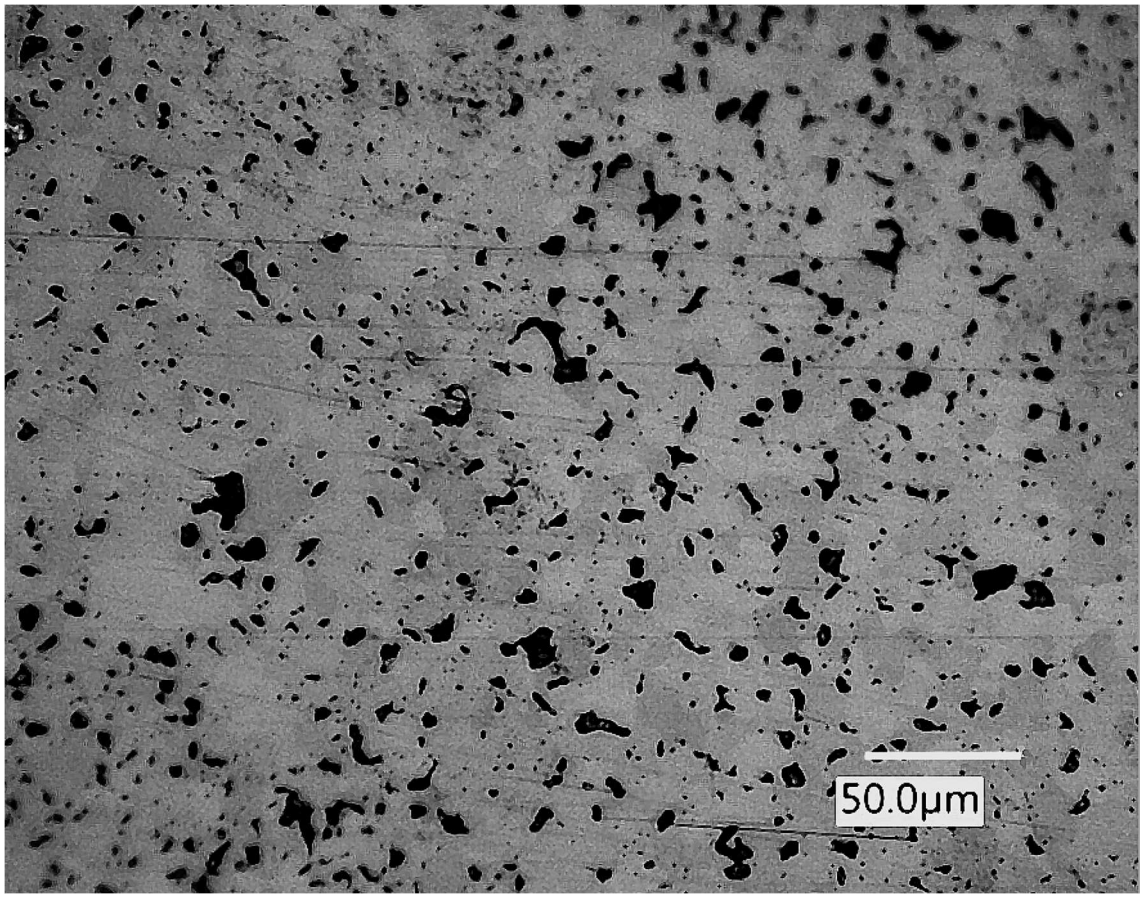

Figure 5.7: Micrograph of Creep Pellet at 1000x magnification. (Incremental etching times were increased so that the total etch time was reduced to 10 minutes)

Average Grain Size Determination:

In order to determine the average grain size for each sample, Image J software was utilized. The linear intercept method was used, which requires that a line of known length be drawn and the number of grains per unit length, counted. This process was repeated 10 times in the horizontal direction and 10 times in the vertical direction. The measurements and average grain size for each sample are provided in Tables 5.5-5.9.

Table 5.5: Average Grain Size Measurements for Pellet A

Vertical Line			**Horizontal Line**		
Length of Line:	20		Length of Line:	20	
Measurement #:	# of grains	Avg Grain Size:	Measurement # :	# of grains	Avg Grain Size:
1	2	10.00	1	1	20.00
2	3	6.67	2	2	10.00
3	2	10.00	3	3	6.67
4	2	10.00	4	2	10.00
5	1	20.00	5	3	6.67
6	3	6.67	6	2	10.00
7	2	10.00	7	4	5.00
8	3	6.67	8	3	6.67
9	2	10.00	9	2	10.00
10	3	6.67	10	1	20.00
Average:		9.67 ± 3.99	Average:		10.50 ± 5.33
Total Average:	10.08 ± 4.60				

Table 5.6 Average Grain Size Measurements for Pellet B

Vertical Line			**Horizontal Line**		
Length of Line:	20		Length of Line:	20	
Measurement #:	# of grains	Avg Grain Size:	Measurement # :	# of grains	Avg Grain Size:
1	2	10.00	1	2	10.00
2	3	6.67	2	2	10.00
3	1	20.00	3	3	6.67
4	2	10.00	4	2	10.00
5	2	10.00	5	1	20.00
6	1	20.00	6	2	10.00
7	3	6.67	7	2	10.00
8	2	10.00	8	2	10.00
9	2	10.00	9	1	20.00
10	1	20.00	10	3	6.67
Average:		12.33 ± 5.45	Average:		11.33 ± 4.76
Total Average:	11.83 ± 5.01				

Table 5.7: Average Grain Size Measurements for Pellet C

Vertical Line			**Horizontal Line**		
Length of Line:	50		Length of Line:	50	
Measurement #:	# of grains	Avg Grain Size:	Measurement # :	# of grains	Avg Grain Size:
1	3	16.67	1	2	25.00
2	3	16.67	2	3	16.67
3	2	25.00	3	2	25.00
4	3	16.67	4	2	25.00
5	3	16.67	5	3	16.67
6	2	25.00	6	3	16.67
7	3	16.67	7	2	25.00
8	3	16.67	8	4	12.50
9	2	25.00	9	3	16.67
10	3	16.67	10	3	16.67
Average:		19.17 ± 4.03	Average:		19.58 ± 4.83
Total Average:	19.38 ± 4.33				

Table 5.8: Average Grain Size Measurements for Tile Sample

Vertical Line			**Horizontal Line**		
Length of Line:	20		Length of Line:	20	
Measurement #:	# of grains	Avg Grain Size:	Measurement # :	# of grains	Avg Grain Size:
1	2	10.00	1	3	6.67
2	3	6.67	2	2	10.00
3	2	10.00	3	4	5.00
4	3	6.67	4	3	6.67
5	3	6.67	5	2	10.00
6	2	10.00	6	2	10.00
7	2	10.00	7	3	6.67
8	3	6.67	8	2	10.00
9	2	10.00	9	3	6.67
10	3	6.67	10	2	10.00
Average:		8.33 ±1.76	Average:		8.17 ± 2.00
Total Average:	8.25 ± 1.83				

Table 5.9: Average Grain Size Measurements for Creep Pellet

Vertical Line			**Horizontal Line**		
Length of Line:	50		Length of Line:	50	
Measurement #:	# of grains	Avg Grain Size:	Measurement # :	# of grains	Avg Grain Size:
1	2	25.00	1	2	25.00
2	2	25.00	2	2	25.00
3	2	25.00	3	2	25.00
4	2	25.00	4	3	16.67
5	3	16.67	5	2	25.00
6	2	25.00	6	2	25.00
7	3	16.67	7	2	25.00
8	2	25.00	8	3	16.67
9	2	25.00	9	2	25.00
10	3	16.67	10	2	25.00
Average:		22.50 ±4.03	Average:		22.33 ± 3.51
Total Average:	22.92 ± 3.70				

Discussion of Microstructure:

The average grain sizes for pellets A (10.08 μm) and B (11.83 μm) were similar. This is likely due to their similar sintering conditions (1450°C). The grains in pellet C were nearly twice the diameter of those in Pellets A and B. Pellet C's fine particle size distribution and higher sintering temperature (1500 °C) improved diffusion processes during fabrication and likely led to the formation of larger grains. The creep pellet was fabricated in identical conditions to Pellet C (same feed stock particle size distribution and sintering schedule). As a result, the Creep pellet and Pellet C have overall the same average grain, 22.92 μm and 19.38 μm, respectively. The Tile sample had the smallest grain size among the lot and was incidentally sintered at the lowest sintering temperature, 1400 °C. The tile sample was sintered for twice the

holding time as the other samples (8 hours vs. 4 hours). The fact that the tile specimen retained extremely small grains even when exposed to prolonged temperature indicates that a higher temperature is required for significant grain growth, and the activation of diffusion processes in U_3Si_2.

Examination of Figures 5.3-5.7 also reveals microstructural details about U_3Si_2 beyond grain size. Figure 5.3 (Pellet A) shows pores are angular, which means they were not fully sintered. This behavior is also seen in Pellet B (Figure 5.4), which has large interconnected pores. Both Pellet A and Pellet B were sintered at 1450°C while Pellet C, which has highly rounded pores (Figure 5.5), was sintered at 1500°C. This would suggest that a temperature of at least 1500°C is required to complete the sintering process. There is also a wide distribution of tiny pores in Pellet C, many of which appear as fabricated. In fact, some look like gas bubbles. Similar small pores are seen in the Tile sample (Figure 5.6); these pores seem to outline the grain boundaries. Much like a second phase precipitate, these small pores or gas bubbles will have the effect of pining grain boundaries and inhibiting grain growth and diffusion across grains.

5.5 Porosity Analysis:

Porosity of a solid is the percentage of void space in the solid. The porosity of the U_3Si_2 samples can be an indication of its mechanical integrity and reveal important details about the corresponding effects of the heat treatments on each sample. One of the greatest influences of the fuel's porosity will be on its thermal conductivity. The thermal conductivity of fuel decreases with increasing porosity as the pores reduce the effective area for heat transfer [Kurt, 2007]. The total porosity in a solid consists of both open and closed pores. Open pores are those that are open to a given surface into which a fluid can penetrate under pressure. Closed pores are not open to any surface and are inaccessible to penetrating fluids. Open porosity and pore size

was characterized through optical imaging and mercury intrusion porosimetry. These results agree with density results acquired through gas pycnometry.

5.5.1 Pore Size Distribution (Optical Imaging):

Optical imaging of the samples was performed using a Keyence VHX-5000 series microscope. The polished surfaces of each sample have been imaged and analyzed for pore size distribution and observed porosity.

The Keyence imaging software can provide post processing of all recorded images. The measurement module was used to analyze pore sizes in each sample. Color contrast was used to highlight pores in each image. The processing software then determines the maximum diameter, minimum diameter, area, and perimeter of each pore, which in turn, provided an estimation of porosity. The fraction of porosity is calculated by determining the surface area of each image occupied by pores. Using this technique, pores were found to be 5.5% of the image surface of Pellet A; 12.4% of the image surface of Pellet B; 2.2% of the image surface of Pellet C; 3.51% of the image surface of the tile sample; and 4.7 % of the image surface of the creep pellet. These values were confirmed using gas pycnometry for density testing.

The distributions of average pore sizes for each pellet are provided in the following graphs. Two peaks were observed in Pellets A and B; the first between 0-0.2 μm and the second between 1-2 μm. The majority of pores fell between the two peak pore sizes in Pellet A. On the other hand, Pellet B pores trended toward larger diameters beyond the 1-2 μm peak. The primary peak in Pellet C was between 0.9-1 μm. Pellet C showed the fewer small pores (below 1 μm) than Pellets A and B; likely due to the higher surface diffusion offered by a bimodal size distribution. It should be noted that at low magnifications, several prominent large pores (> 50 μm) were observed in Pellet C. No such pores were observed in Pellets A or B.

The peak pore size of the Tile specimen was similar to that of Pellets A and B, in that it showed two characteristic peaks. The Tile sample had one peak between 0-0.2 μm and another between 2-3 μm. It is believed that the high frequency of pores between 2-3 μm are due to the lower sintering temperature of the Tile relative to the sintering temperature used for Pellets A, B, and C. Higher sintering temperatures would certainly reduce pore size and would likely cause the peak of 2-3 μm to shift down towards 0.9-1 μm like the other pellets. The Creep pellet also had a large peak between 0-0.2 μm, like Pellets A and B and the Tile sample. Another broad peak was noted between 0.9 and 3 μm for the Creep Pellet. Aside from the peak between 0-0.2 μm, there were fewer small pores compared to the other samples. This is likely due to the higher density of the sample. The creep pellet was pressed in a die with smaller diameter than that used for Pellets A, B, and C. The smaller die dimensions provided more favorable pressing conditions, which resulted in a higher density green body compact. Although the tile specimen used a different die as well, the overall green body density was nearly the same as Pellets A, B, and C.

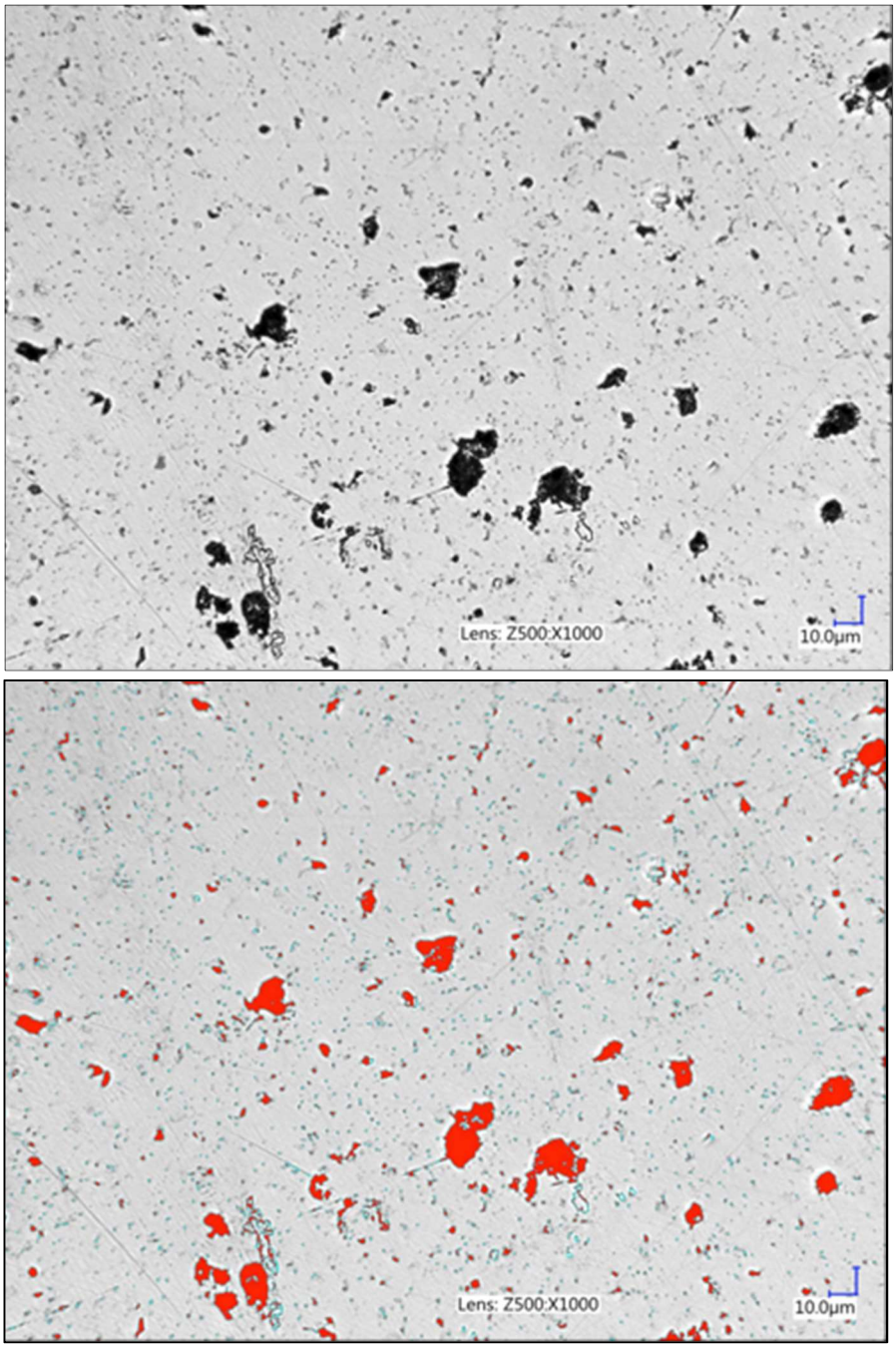

Figure 5.8: Selected pore set from pellet A (1000X magnification; 10µm scale). Pores analyzed are shown in red.

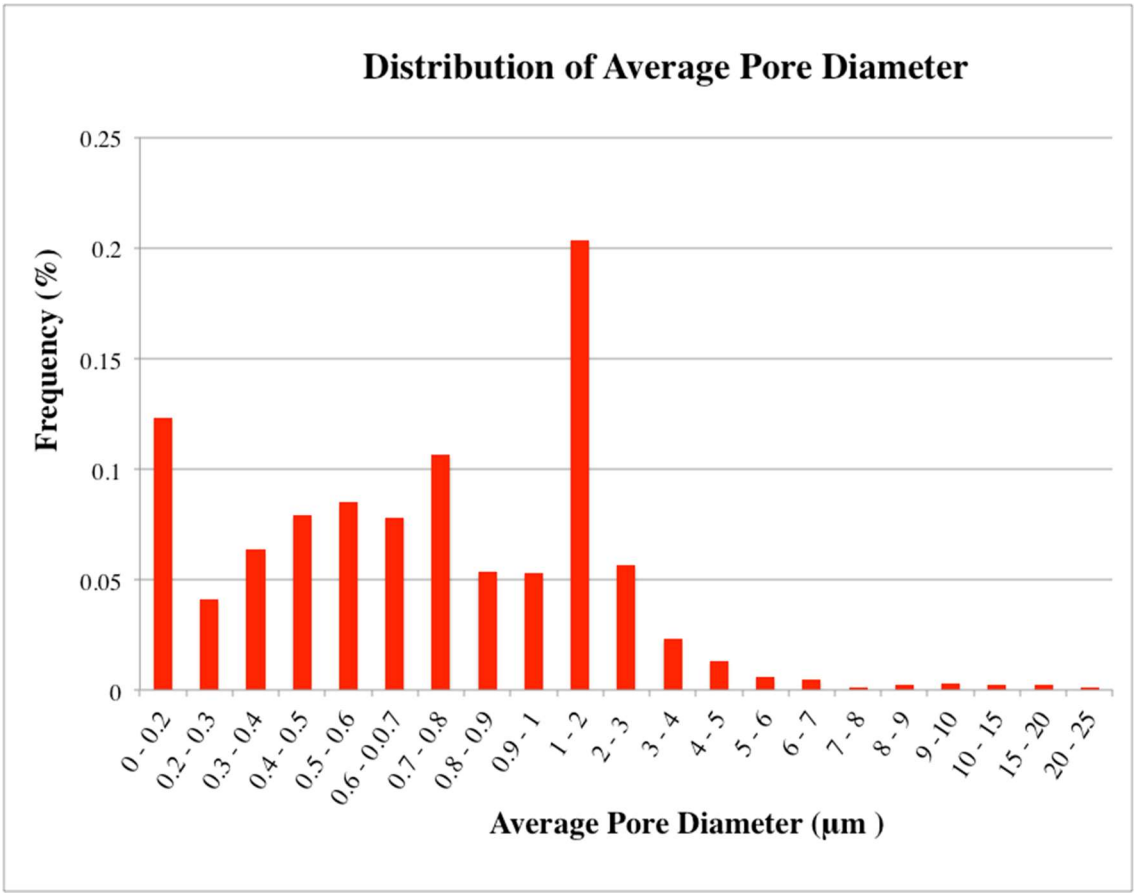

Figure 5.9: Pellet A Histogram- distribution of average pore diameters

Table 5.10: Pellet A- Statistics of Measured Pores

	Max diameter (µm)	Area (µm²)	Min diameter (µm)	Perimeter (µm)
Average	1.6	2.6	0.9	4.5
Standard Deviation	2.2	13.2	1.3	7.8
Max	36.4	277.3	18.5	140.5
Min	0.3	0.1	0.1	0.7
Total	2775.4	4567.5	1569.6	8000.7

Table 5.11: Pellet A- Calculated Area Fraction of Pores

Total pore area (µm²)	4567.5
Total region area(µm²)	82412.3
Area Fraction of Pores	5.5%

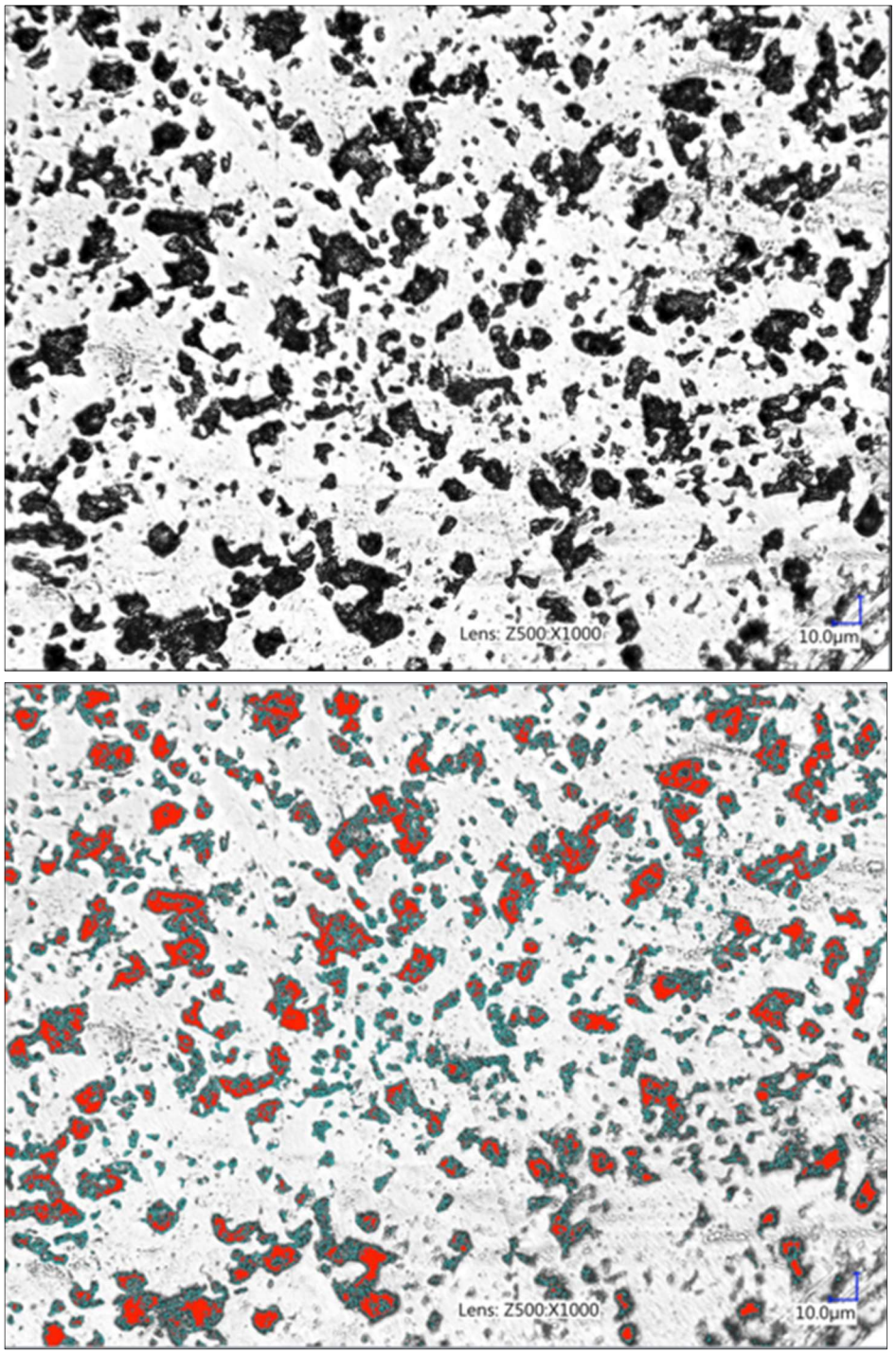

Figure 5.10: Selected pore set from pellet B (1000X magnification; 10µm scale). Pores analyzed are shown in red.

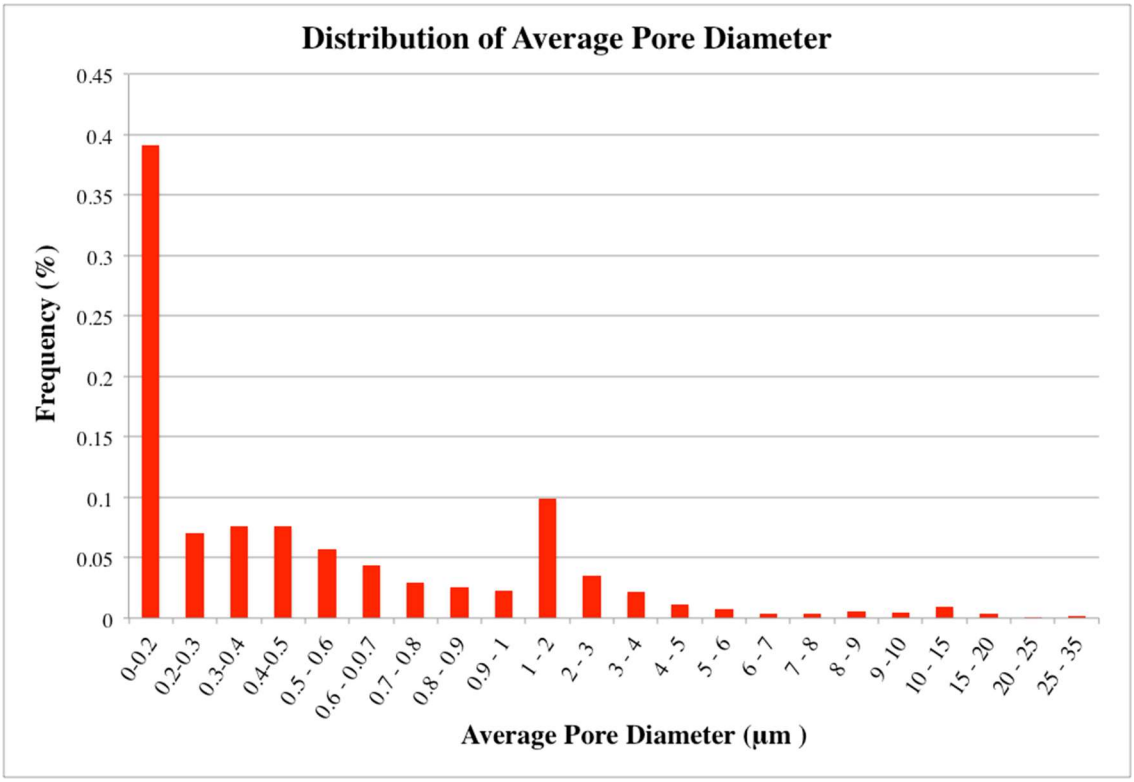

Figure 5.11: Pellet B Histogram- distribution of average pore diameters

Table 5.12: Pellet B- Statistics of Measured Pores

	Max diameter (µm)	Area (µm²)	Min diameter (µm)	Perimeter (µm)
Average	2.0	4.0	1.0	7.4
Standard Deviation	3.4	17.2	2.1	18.7
Max	35.4	296.6	28.5	281.4
Min	0.3	0.1	0.1	0.8
Total	5201.8	10234.9	2610.7	19121.6

Table 5.13: Pellet B- Calculated Area Fraction of Pores

Total pore area (µm²)	10234.9
Total region area (µm²)	82412.3
Area Fraction of Pores	12.4%

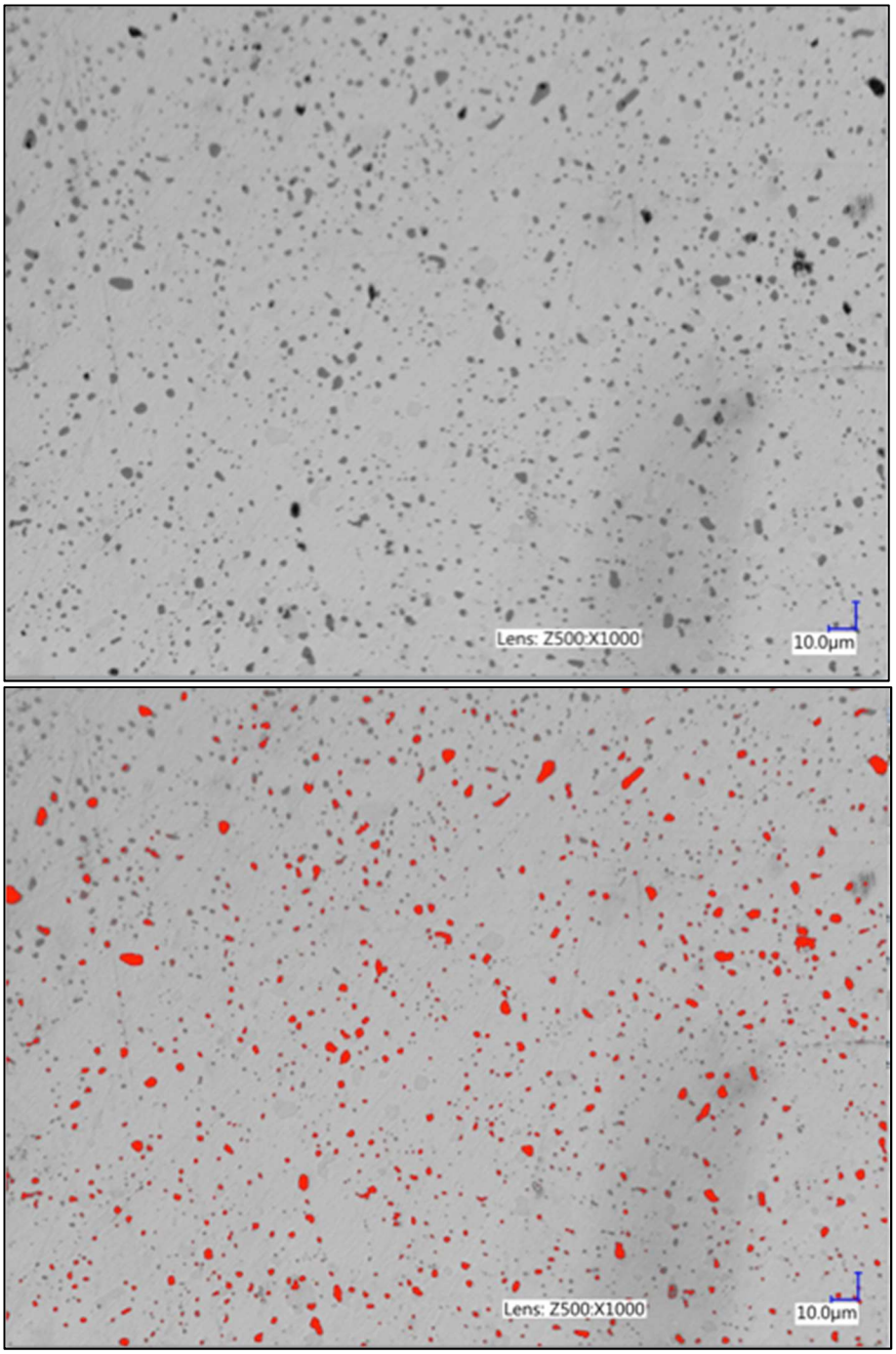

Figure 5.12: Selected pore set from Pellet C (1000X magnification; 10µm scale). Pores analyzed are shown in red.

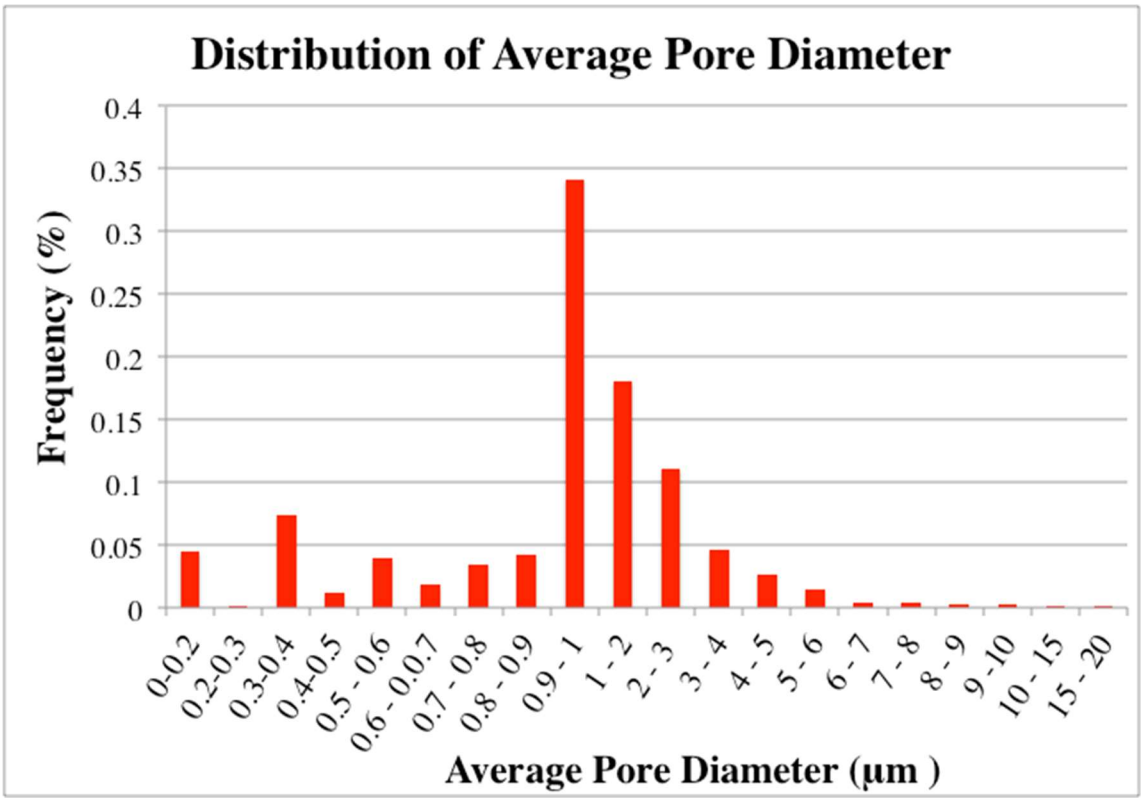

Figure 5.13: Pellet C Histogram- distribution of average pore diameters

Table 5.14: Pellet C- Statistics of Measured Pores

	Max diameter (µm)	Area (µm²)	Min diameter (µm)	Perimeter (µm)
Average	1.8	2.2	1.0	5.0
Standard Deviation	1.4	3.5	0.8	4.1
Max	10.5	30.3	5.5	32.1
Min	0.3	0.1	0.1	0.8
Total	1453.4	1836.6	842.6	4106.3

Table 5.15: Pellet C- Calculated Area Fraction of Pores

Total pore area (µm²)	1836.6
Total region area(µm²)	82412.3
Area Fraction of Pores	2.2%

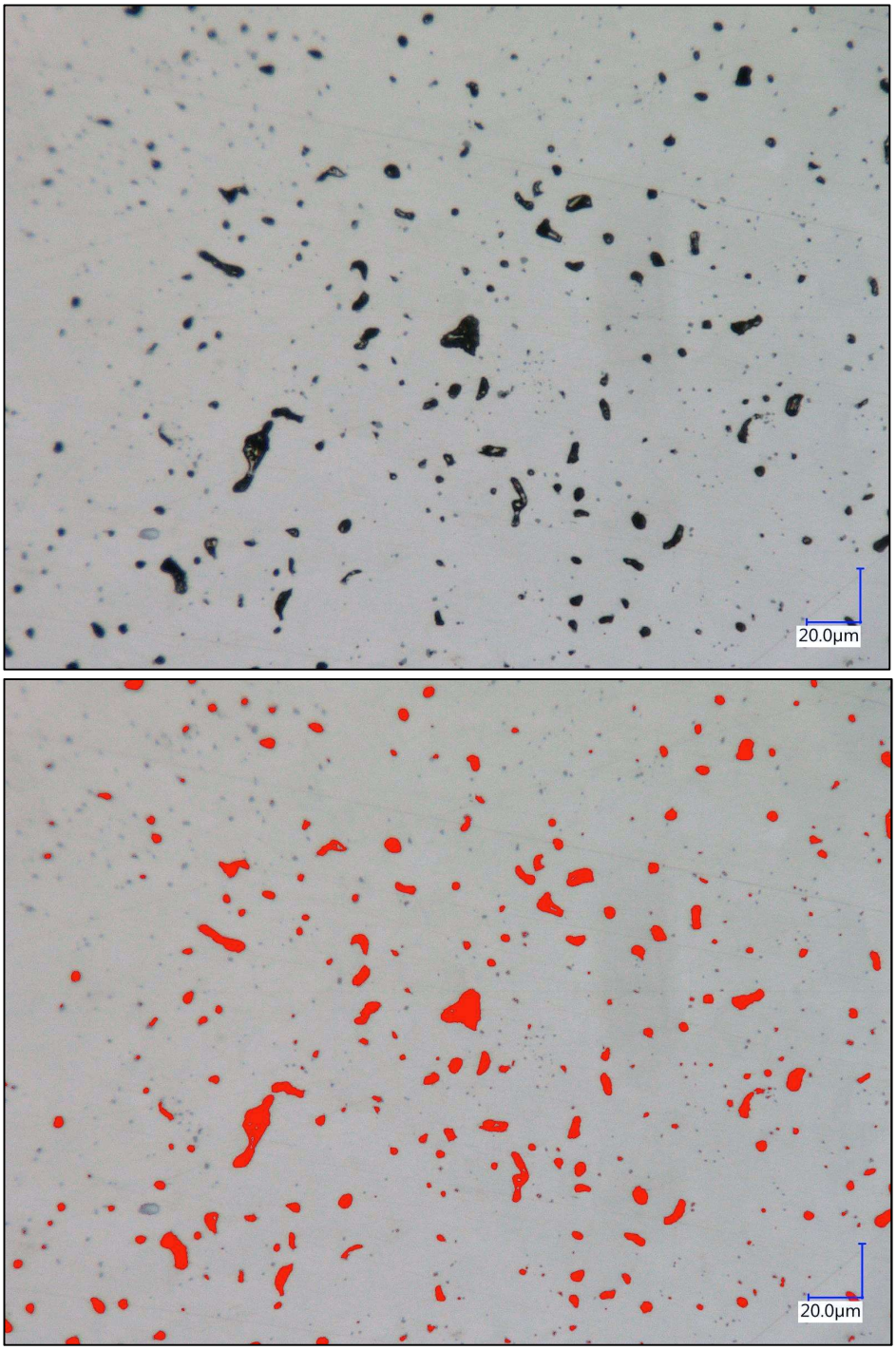

Figure 5.14: Selected pore set from Tile Sample, (1000x magnification; 20µm scale). Pores analyzed are shown in red.

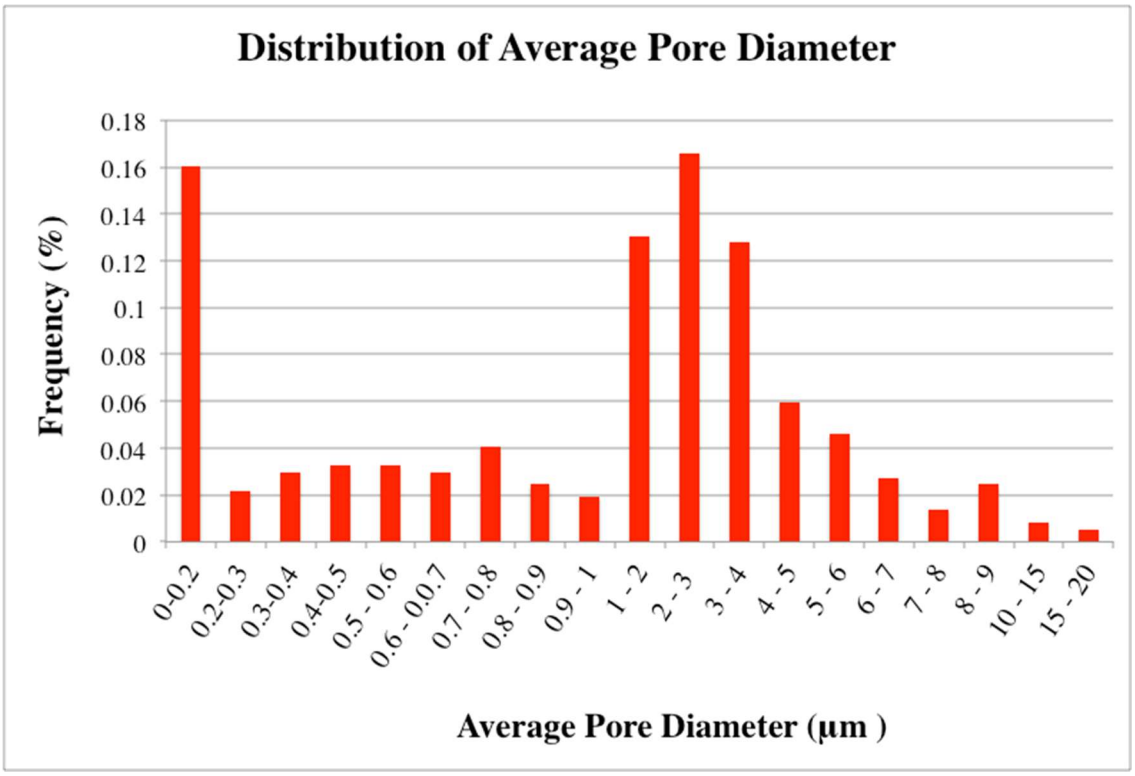

Figure 5.15: Tile Sample Histogram- distribution of average pore diameters

Table 5.16: Tile Sample- Statistics of Measured Pores

	Max diameter (µm)	Area (µm²)	Min diameter (µm)	Perimeter (µm)
Average	2.0	5	1.1	5.5
Standard Deviation	3.1	12.7	1.6	8.5
Max	30.4	157.8	13.6	76.3
Min	0.2	0.1	0.1	0.4
Total	1132.0	2895.8	653.0	3161.6

Table 5.17: Sample 4 -Calculated Area Fraction of Pores

Total pore area (µm²)	2895.8
Total region area(µm²)	82412.3
Area Fraction of Pores	3.51%

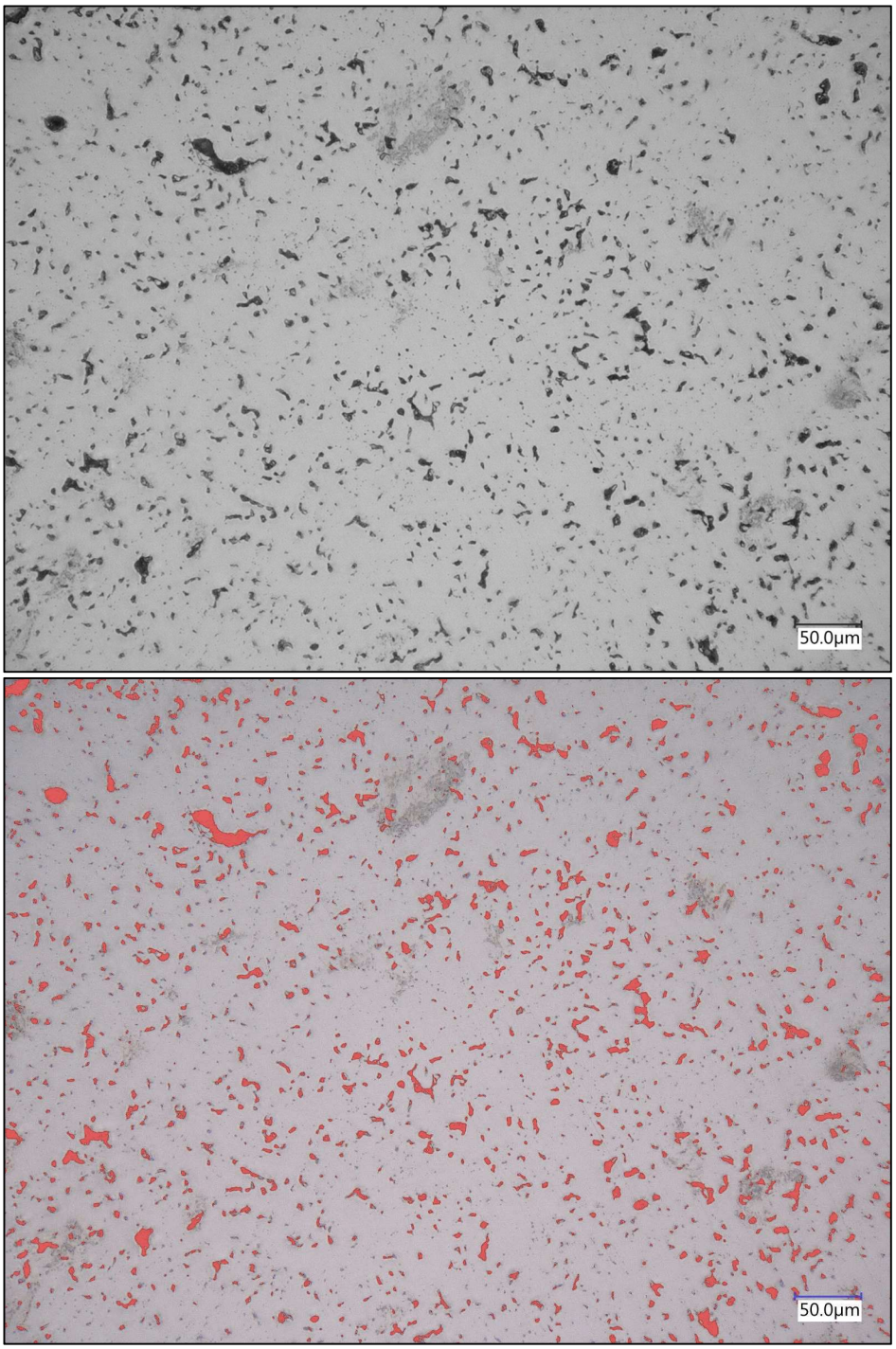

Figure 5.16: Selected pore set from creep pellet 1 (500x magnification; 50µm scale). Pores analyzed are shown in red.

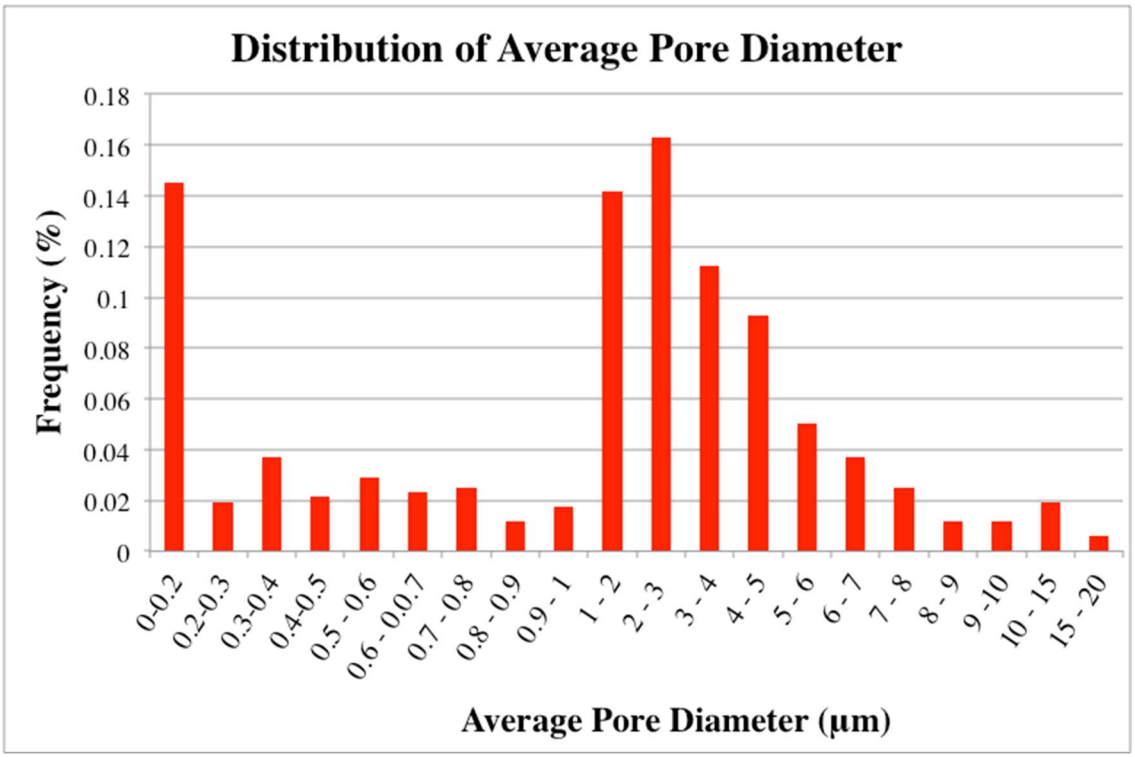

Figure 5.17: Creep Pellet 1 Histogram- distribution of average pore diameters

Table 5.18: Creep Pellet 1- Statistics of Measured Pores

	Max diameter (µm)	Area (µm²)	Min diameter (µm)	Perimeter (µm)
Average	2.9	6.9	1.4	8.1
Standard Deviation	3.9	17.3	1.8	11.4
Max	59.3	458	21	180
Min	0.4	0.2	0.1	0.8
Total	6783.6	15962.4	3299.2	18742.2

Table 5.19: Creep Pellet 1- Calculated Area Fraction of Pores

Total pore area (µm²)	15962.4
Total region area(µm²)	334382.6
Area Fraction of Pores	4.7%

5.5.2 PYCNOMETRY:

Density of the four pellet samples was measured using gas pycnometry. Pycnometry uses gas displacement to determine the volume occupied by each pellet sample. By knowing the mass of the pellets, the density and percent theoretical density can be determined. The volume of each sample was measured 10 times to insure that values were consistent and reproducible (see Table 5.20). The average volume was used in computing the density of each pellet (shown in Table 5.21). The theoretical density of U_3Si_2 is 12.2 g/cm^3. Gas pycnometry was not performed on the tile specimen because it was too large to fit in the pycnometer's sample holder.

Table 5.20: Volume each pellet using gas displacement technique

Measurement #	Volume (cm^3)			
	Pellet A	**Pellet B**	**Pellet C**	**Creep Pellet**
1	0.3274	0.3482	0.2594	0.2023
2	0.3273	0.3478	0.2592	0.2022
3	0.3274	0.3480	0.2593	0.2023
4	0.3274	0.3473	0.2591	0.2022
5	0.3273	0.3470	0.2591	0.2022
6	0.3274	0.3487	0.2593	0.2025
7	0.3273	0.3474	0.2594	0.2024
8	0.3271	0.3478	0.2591	0.2019
9	0.3272	0.3473	0.2593	0.2023
10	0.3273	0.3470	0.2591	0.2025

Table 5.21: Density of Pellets

	Mass (g)	**Volume (cm^3)**	**Density (g/cm^3)**	**%TD**
Pellet A	3.7636	0.3273 ± 0.0001	11.4982 ± 0.0035	94.25 ± 0.03 %
Pellet B	3.7815	0.3477 ± 0.0005	10.8773 ±0.0167	89.16 ± 0.14 %
Pellet C	3.1040	0.2593 ± 0.0001	11.9729 ± 0.0057	98.14 ± 0.05 %
Creep Pellet	2.4098	0.2023 ± 0.0002	11.9142 ± 0.0095	97.66 ± 0.08 %

The calculated densities of the pellets are consistent with the observed porosity determined through optical microscopy imaging. Additionally, the different particle size

distributions used in fabricating the pellets is reflected in the as-sintered porosities. The bimodal feed stock powder used for the Creep Pellet and Pellet C resulted in a much denser pellet compared to A & B. Between Pellet A and B, pellet A had a wider particle size distribution which resulted in a denser green body compact and denser as-sintered pellet. The particle size distribution of the feed stock powder used for Pellet B, featured a narrower peak of single size particles, when compared to Pellet A. Since smaller particles weren't available to fill voids in the sample, Pellet B resulted in the lowest density pellet.

5.5.3 Mercury Intrusion Porosimetry:

Mercury intrusion porosimetry was performed using a Quantachrome PoreMaster 33. The nature of the analysis prevents test specimens from being used for future characterization efforts. For this reason, only the single Creep pellet was analyzed using mercury porosimetry.

The porosimeter calculates pore size by relating the increasing volume of intruded mercury to the intrusion pressure. By acquiring data in intervals, the instrument is able to estimate a pore size distribution. The overall volume of mercury intruded in the sample can be used to determine open porosity in the sample.

Open porosity of specimens will be determined using a Quantachrome Poremaster 33 mercury porosimeter. The principle of open porosity provides that if a fluid is pressed into the pore of a given solid under pressure, the fluid will occupy the volume of the pores. The total pore volume can then be estimated using the total volume occupied by the penetrating liquid. If the V is the volume of the bulk sample and V_l is the volume of the penetrated liquid, then the open porosity can be described by the following:

$$\% \text{ Open Porosity} = 100 \times (V_l / V).$$

The mercury fluid pressure can be used to determine pore size [ASTM E1876-09, 2009]. As the pressure is increased, the fluid will penetrate pores of smaller sizes. If the pores are assumed to be cylindrical, then the work required to fill a pore whose radius is r and length l is given as:

$$W_1 = 2\pi r l \gamma \cos(\theta),$$

where γ is the surface tension of the fluid and θ is the contact angle. Additionally, it is known that the work required to force mercury into a pore whose radius is r and length l is given as:

$$W_2 = P\pi r^2 l,$$

where P is the applied pressure. Since $W_1 = W_2$, the two equations can be set equal to one another giving:

$$Pr = 2\gamma \cos(\theta) \quad [\text{psi-}\mu\text{m}],$$

where γ and $\cos(\theta)$ are constants. The typical values of γ and $\cos(\theta)$ for mercury are 480 dynes/cm and 140°, respectively. Thus, by knowing the values of γ and $\cos(\theta)$ in addition to the intrusion pressure, the pore diameter can be calculated. The pore size distribution can also be calculated using the change in intruded mercury volume and pressure at different intervals. If dV is the elemental change in the penetrated volume into pores of radii between r and $r+dr$, then

$$dV = D(r)dr,$$

where $D(r)$ is the volume pore size distribution function, given as the pore volume per unit interval of radius. Additionally, by differentiating the equation relating applied pressure, P, and radius, r, the following relation is

$$dr = -r\, dP/P.$$

When the resulting *dr* is substituted into the prior equation, the distribution can be calculated based on the incremental values of the volume at each step in pressure

$$D(r) = (P/r)dV/dP.$$

Thus, it is possible to obtain the open porosity of each sample as well as the contributing pore size distribution.

A histogram of normalized intruded volume of mercury vs. pore size is shown in Figure X. The pore size distribution features a peak between 0.5 μm and 1.0 μm. Another interesting feature is the presence of a few pores between 90 μm and 200 μm. These pores were larger than any observed on the surface of the pellet samples and could possibly be due to the porosimeter misinterpreting the EDM'd notches as pores on the creep pellet surface.

The volume of mercury intruded in the sample was 0.005 cm^3/g. This value was multiplied by the sample weight to determine the total volume of mercury intruded in the sample (0.0120 cm^3/g). This volume of mercury intruded in the sample was divided by the volume of the sample, as determined through gas pycnometry. This value provided the percent of the sample occupied by mercury. This in turn is a measurement of closed porosity in the sample. The details of the calculation are tabulated in Table 5.22. The porosity of the sample was found to be 5.96%, which means that the sample is at most 94.04% theoretical density. However, this value is much smaller than that determined from gas pycnometry (97.7%TD). To investigate the discrepancy, the weight of the sample after testing was compared to that after testing. Weight gain was attributed to trapped mercury and was used to calculate a minimum amount of mercury intruded in the sample. By multiplying the gained mercury weight by the density of mercury, the volume of trapped mercury was calculated (0.0151 cm^3). This value was then compared to the volume of the sample as determined through gas pycnometry. Using this

method, the mercury was found to be 7.46% of the sample (details shown in Table 5.23). This value was even greater than that previously calculated through porosimetry results and significantly larger than that as determined from gas pycnometry. It should be noted that the gas pycnometer is a far more accurate measure of volume and density than the mercury porosimeter. The mercury porosimeter has in fact had technical problems in the past. It's likely that some of the discrepancy is due to the instrument itself. There is still a sizable discrepancy between the gas pycnometry density results and those of the "mercury weight gained" calculation. It is possible that the specimen had microcracks, which provided a pathway for mercury. This would explain the large volume of mercury intruded relative to the porosity determined through gas pycnometry and optical microscopy.

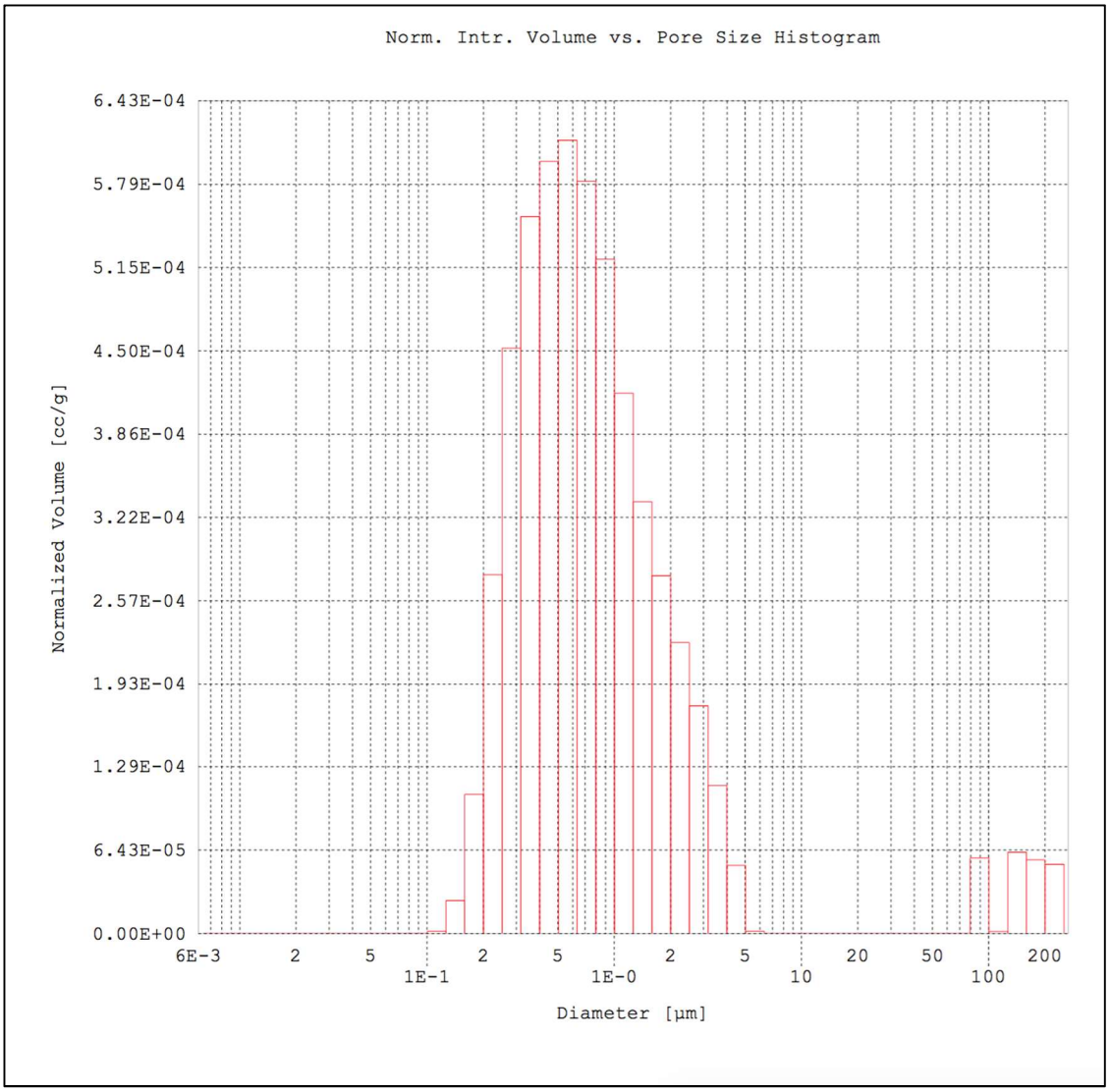

Figure 5.18: Pore Size Histogram

Table 5.22: Porosity Calculation Details (Normalized Mercury)

Intruded volume	0.005	cm^3/g
Sample weight	2.4098	g
Intruded volume in sample	0.0120	cm^3
Sample volume determined from pycnometry	0.2023	cm^3
% of volume occupied by Hg (estimation of porosity)	5.96	%
%Theoretical Density	94.04	% TD

Table 5.23: Porosity Calculation Details (Weight Gained in Mercury)

Weight of sample before porosimetry	2.40976	g
Weight of sample after porosimetry	2.61431	g
Weight Gain	0.20455	g
Density of Hg	13.546	g/cm^3
Volume of Hg	0.0151	cm^3
Volume of sample from pycnometry	0.2023	cm^3
Porosity of sample	7.46	%

5.6 XRD & Second Phase Analysis:

5.6.1XRD:

XRD was performed on polished surfaces of pellets A, B, and C in order to confirm composition. A Cu-Kα source was used over a measurement range of 5°-65° with a scanning rate of 1°/min. As can be seen in Figure 5.19, a spectrum overlay for all three pellets shows good agreement between samples.

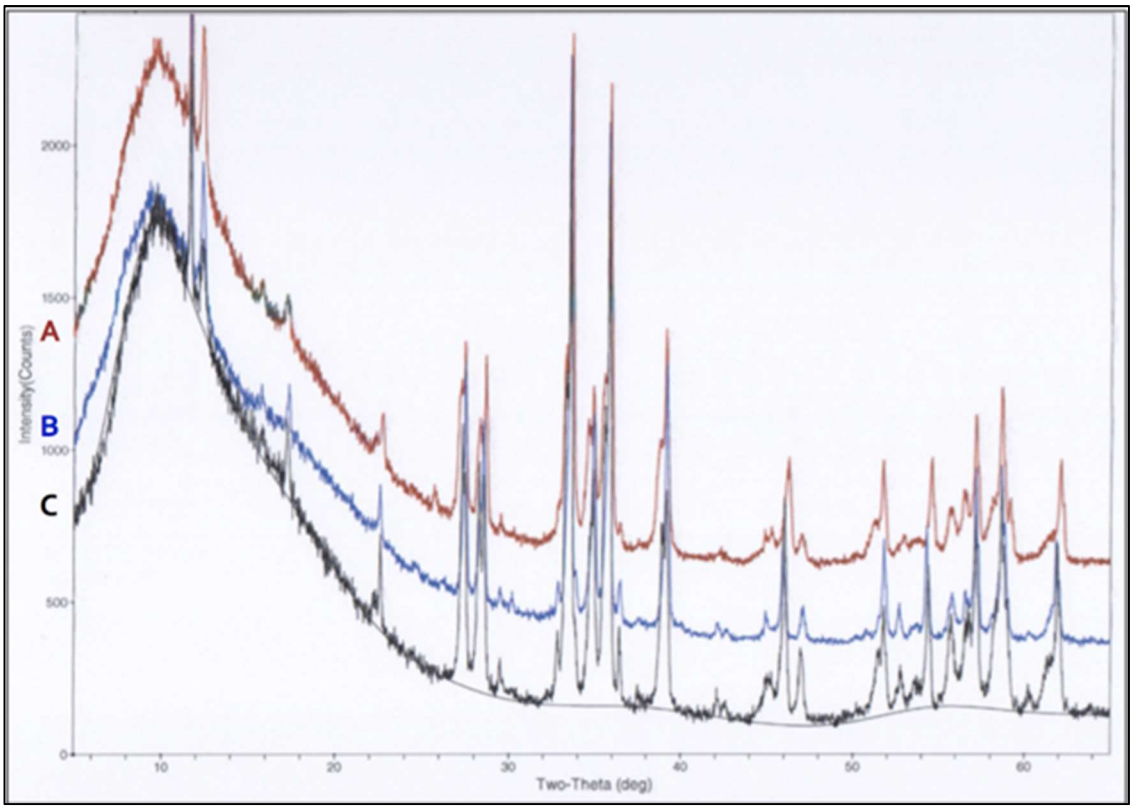

Figure 5.19: Overlay of each pellet's XRD spectrum. (Top to Bottom: A, B, & C)

JADE software was used to identify and match peaks in the XRD spectrums. The results of the peak matching indicate that each pellet is U_3Si_2 with minor deviations due to impurities. The PDF card data associated with U_3Si_2 is taken from [Zachararisen1949]. An attempt was made to find a more recent data file for U_3Si_2; however, Zachariasen is the only literature source for U_3Si_2- even the more current PDF cards reference back to the original Zachariasen article. Since the spectrums of the three samples show good agreement, the overlay of the U_3Si_2 spectrum is shown for pellet C in Figure 5.20. When peak searching was performed, no other U/Si compounds matched the spectrum of the three pellets. The spectrum shows the presence of minor impurities at the higher angles. Secondary precipitate phases were confirmed through electron backscatter imaging and electron dispersive spectroscopy and are discussed in the following section.

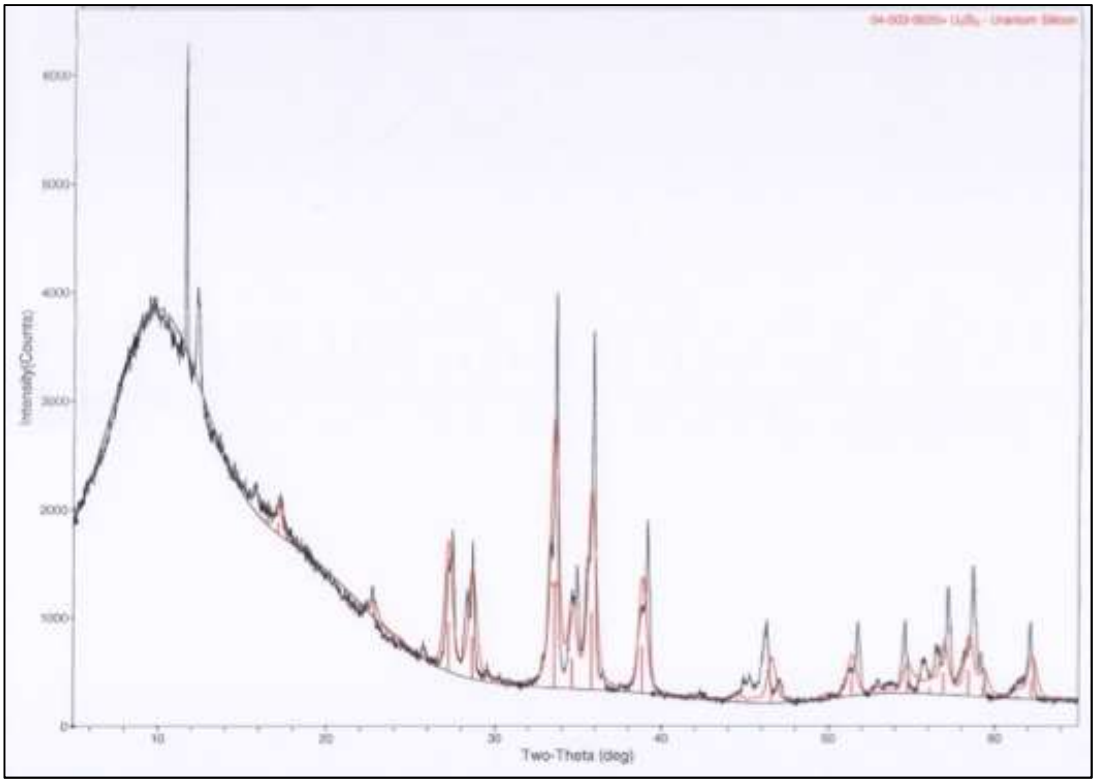

Figure 5.20: Overlay of U_3Si_2 peak spectrum over the spectrum of pellet C.

5.6.2 IDENTIFICATION OF SECOND PHASE PRECIPITATES:

Energy dispersive X-ray spectroscopy (EDS) was performed on pellets A, B, and C as well as the Tile sample. The EDX results were used to determine the composition of the samples and identify second phase precipitates. The imaged surface of each sample was ground and polished the day of microscopy. The sample was mounted to an SEM sample stub using double-sided carbon tape. SEM with BSE was used to image the samples in order to apply compositional contrasting. The beam voltage was fixed at 20kV for all images. For each scanning electron (SE) image, a corresponding BSE image was recorded. In all EDX examination, the uncertainty in the Uranium Weight % calculation was ± 3.00 %. The uncertainty in the Silicon content was negligible. In cases, where precipitate composition did not match a stoichiometric U-Si compound, the uncertainty in the U- weight% was factored in to allow for phase determination. The resulted in positive phase determination for nearly every point analyzed. The compositions of possible U-Si-O compounds are provided in the following two Tables.

Table 5.24: U-Si Compounds

Uranium Compounds by Wt %		
Compound	Wt % U	Wt% Si
U_3Si_2	92.71%	7.29%
U_3Si	96.22%	3.78%
USi	89.45%	10.55%
U_3Si_5	83.57%	16.43%
USi_2	80.91%	19.09%
USi_3	73.86%	26.14%

Table 5.25: U-O-Si Compounds

Uranium Compounds by Wt %			
Compound	Wt % U	Wt% Si	Wt % O
UO_2	88.15%	0%	11.85%
U_3Si_2O	90.82%	7.14%	2.03%
$U_3Si_2O_2$	89.01%	7.00%	3.99%
USiO	84.37%	9.96%	5.67%
$USiO_2$	79.85%	9.42%	10.73%

Pellet A:

An SE image of pellet A is shown in Figure 5.21, with the corresponding BSE image of the same region in Figure 5.22. EDX was performed on areas of the surface as shown in Figure 5.23.

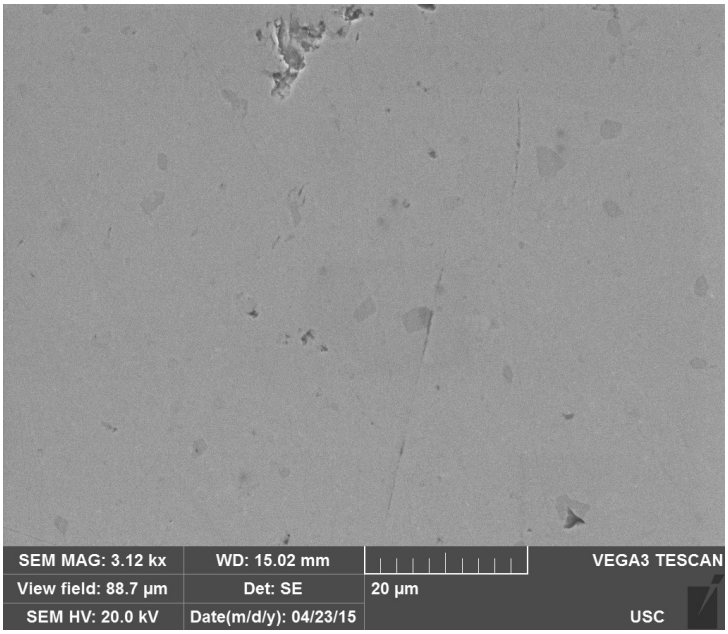

Figure 5.21: Pellet A---SE image (3120 magnification)

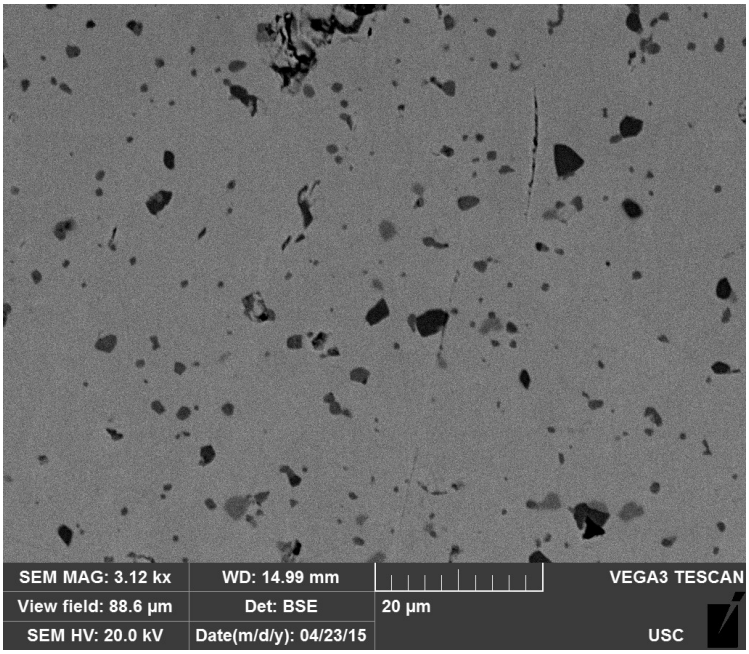

Figure 5.22: Pellet A---BSE image (x3120 magnification)

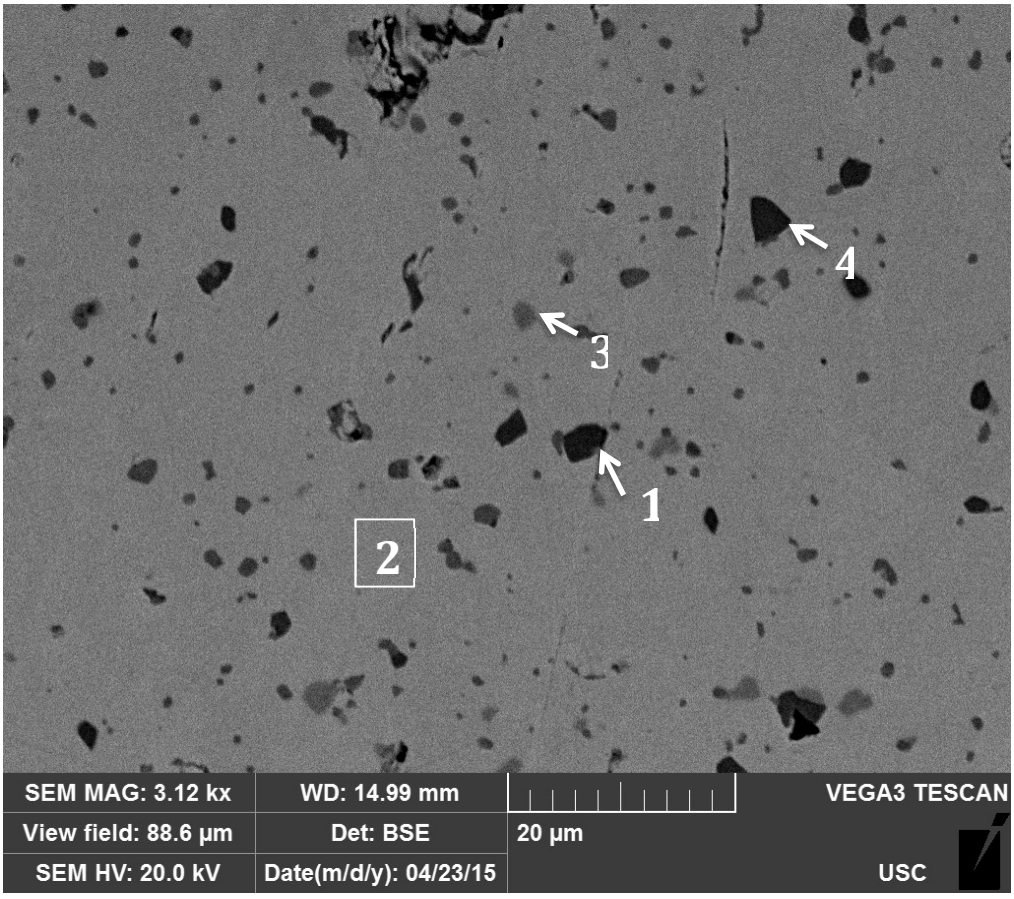

Figure 5.23: EDX was performed on four regions of Pellet A

Table 5.26: EDX composition results for the four regions shown in Figure 5.23.

	Point 1	Point 2	Point 3	Point 4
Wt % U	85.27	91.9	90.55	84.99
Wt % Si	14.73	8.1	9.45	15.01
Wt % O	0	0	0	0
Composition	U_3Si_5	U_3Si_2	USi	U_3Si_5

The bulk material in pellet A was identified at U_3Si_2. The darkest precipitates in the pellet are likely U_3Si_5. The medium grey precipitate is likely USi. No Oxygen was identified in the analysis.

Pellet B:

An SE image of pellet B is shown in Figure 5.24, with the corresponding BSE image of the same region in Figure 5.25. EDX was performed on areas of the surface as shown in Figure 5.26.

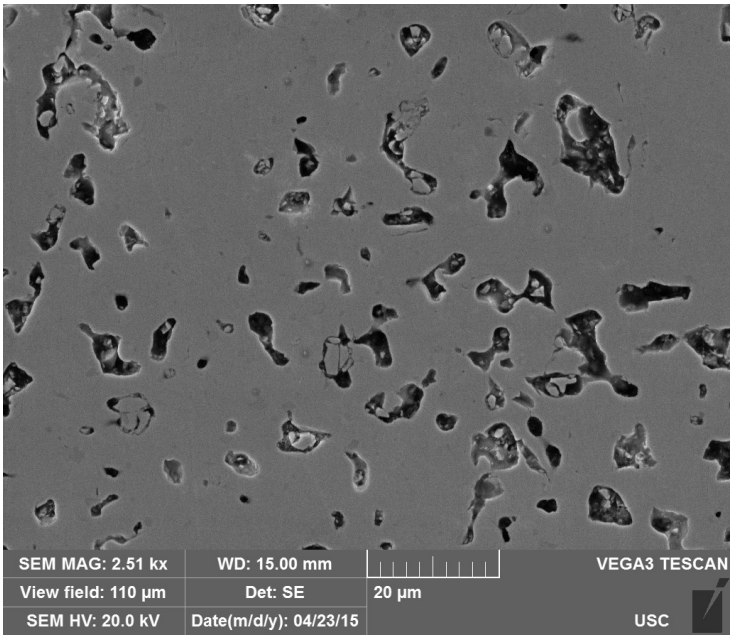

Figure 5.24: Pellet B---SE image (x2510 magnification)

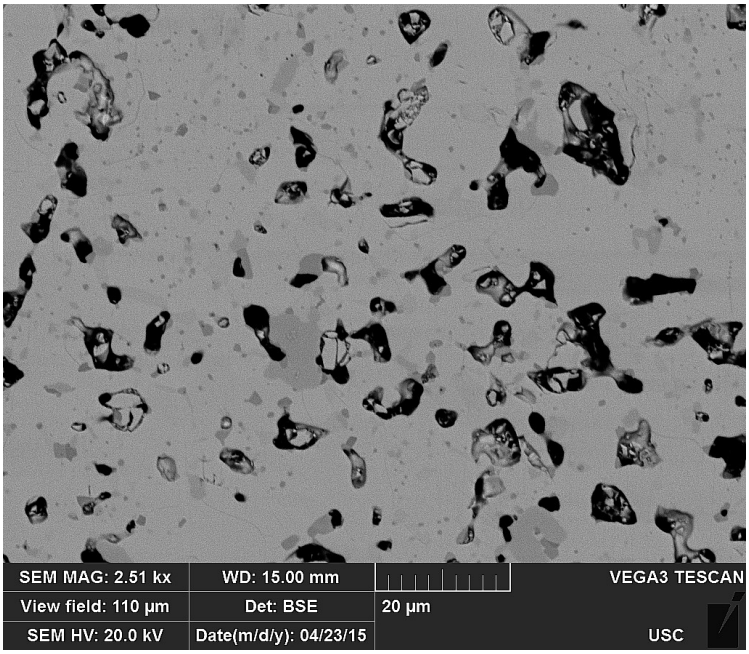

Figure 5.25: Pellet B---BSE image (x2510 magnification)

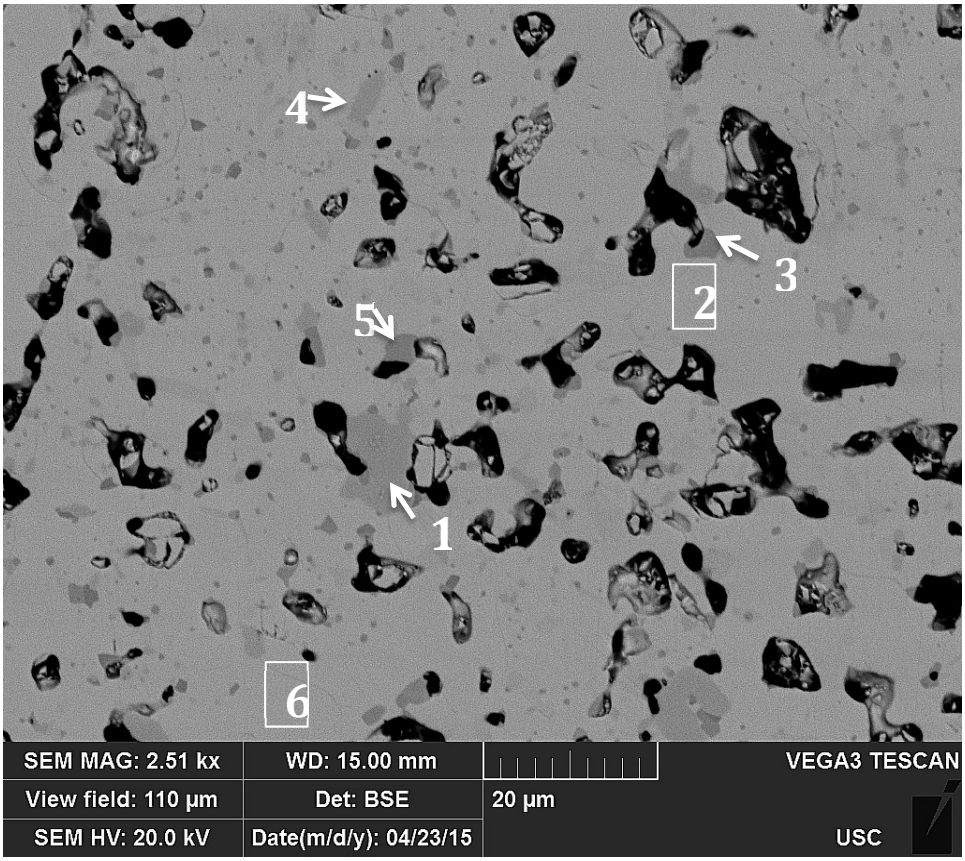

Figure 5.26: EDX was performed on six regions of Pellet B.

Table 5.27: EDX composition results for the three regions shown in Figure 26.

	Point 1	Point 2	Point 3	Point 4	Point 5	Point 6
Wt % U	75.13	91.42	92.23	75.69	90.98	91.79
Wt % Si	24.87	8.58	0.5	24.08	7.11	8.21
Wt % O	0	0	7.27	0.23	1.91	0
Composition	USi_3	U_3Si_2	UO_2	USi_3	U_3Si_2O	U_3Si_2

The SE image in Figure 5.24 shows the high degree of porosity associated with Pellet B. This is reasonable since pellet B was fabricated using the coarsest particle size distribution of the three pellets (see Figure 5.2). The bulk material in pellet B was identified at U_3Si_2. However, precipitates are present and seem to outline the U_3Si_2 grains. The large precipitate at point 1 was identified as USi_3. Point 4 was also identified as USi_3. The region at point 3 was rich in Uranium and Oxygen. Although not perfectly stoichiometric, the phase matches the composition of UO_2 if the uncertainty in uranium weight percent is taken into account. The 0.5 wt% Silicon identified at that point was likely due the bulk material and not the precipitate, itself. Point 5 had the composition of U_3Si_2, with a small wt% of O at the expense of U. This composition matches that of U3Si2O.

Pellet C:

An SE image of pellet C is shown in Figure 5.27, with the corresponding BSE image of the same region in Figure 5.28. EDX was performed on areas of the surface as shown in Figure 5.29.

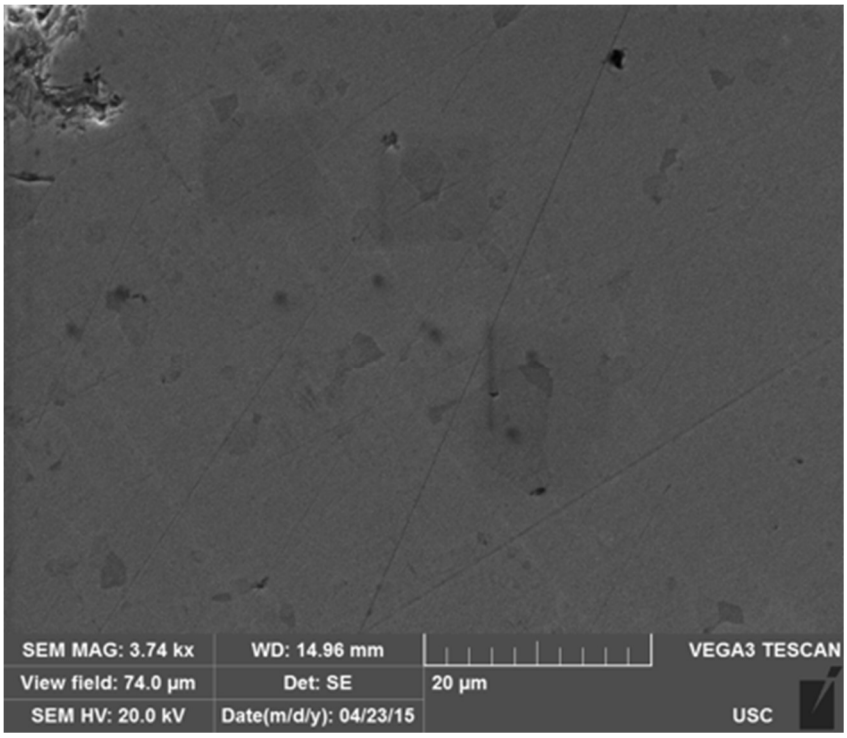

Figure 5.27: Pellet C--SE image of pellet (x3740 magnification)

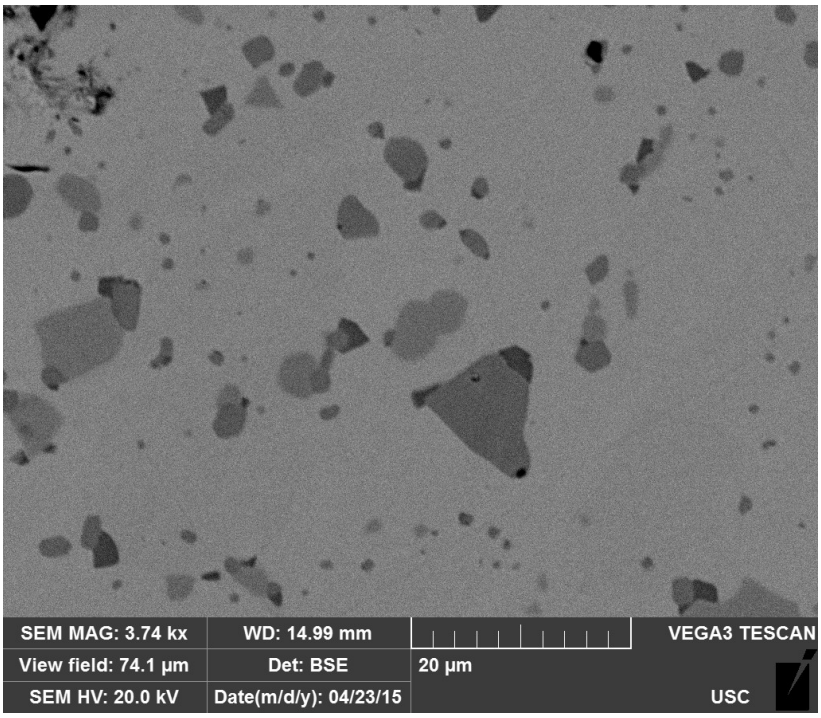

Figure 5.28: Pellet C--BSE image (x3740 magnification)

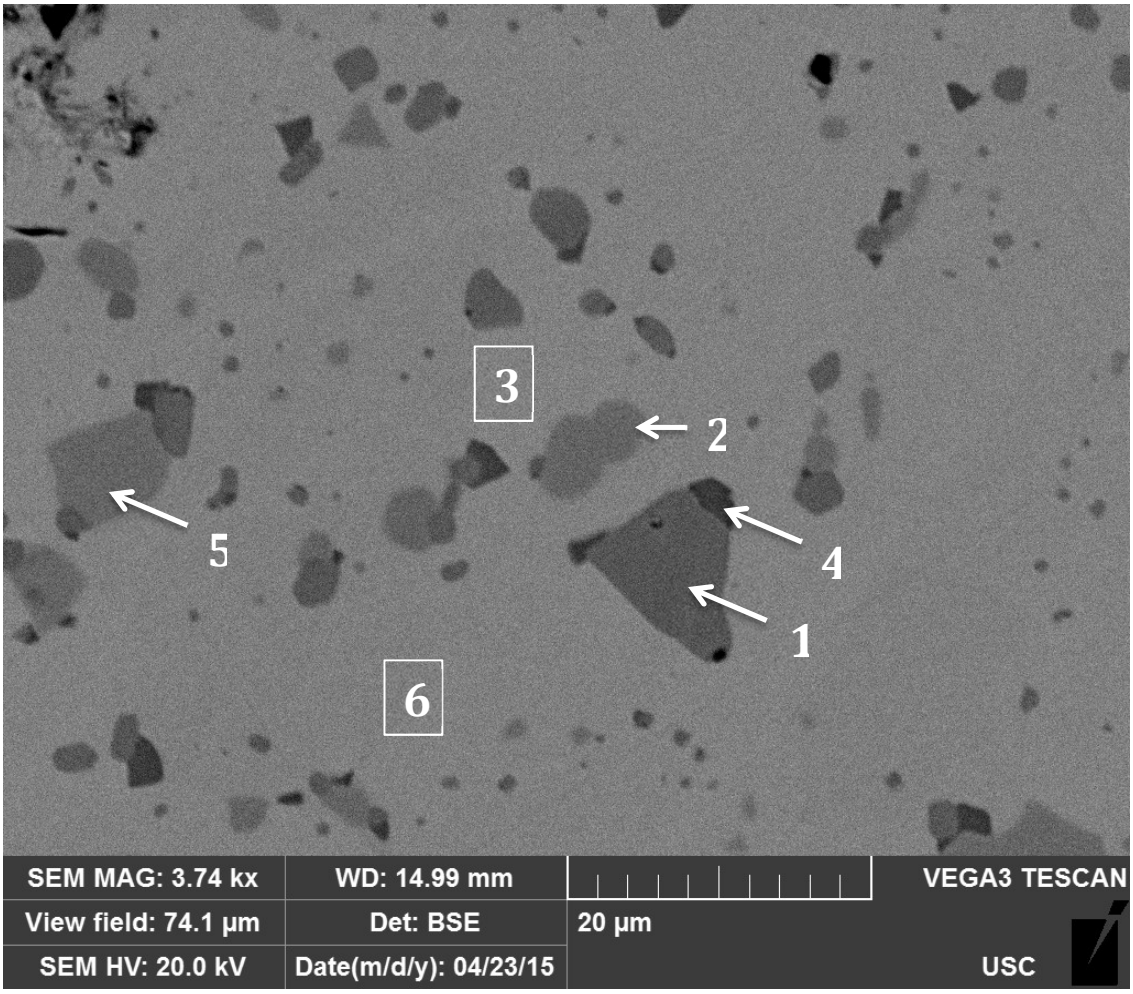

Figure 5.29: EDX was performed on six regions in Pellet C.

Table 5.28: EDX composition results for the three regions shown in Figure 5.29.

	Point 1	Point 2	Point 3	Point 4	Point 5	Point 6
Wt % U	93.25	75.92	92.04	91.23	76.06	91.86
Wt % Si	0	23.95	7.96	8.77	23.94	8.14
Wt % O	6.75	0.13	0	0	0	0
Composition	UO_2	USi_3	U_3Si_2	U_3Si_2	USi_3	U_3Si_2

The bulk material in pellet C was identified at U_3Si_2. The light grey precipitates at points 2 and 5 were identified as USi_3. Regions of USi_3 were also identified in pellet B. The dark precipitate at point 4 was too small for an accurate EDS analysis and instead picked up the

composition of the background material, U_3Si_2. Given the dark color relative to the other identified precipitates, the phase at point 4 is likely U_3Si_5. The large precipitate at point 1 was comprised of only uranium and oxygen. While not perfectly stoichiometric, the phase is likely UO_2.

Tile Sample:

An SE image of the Tile sample is shown in Figure 5.30, with the corresponding BSE image of the same region in Figure 5.31. EDX was performed on areas of the surface as shown in Figure 5.32.

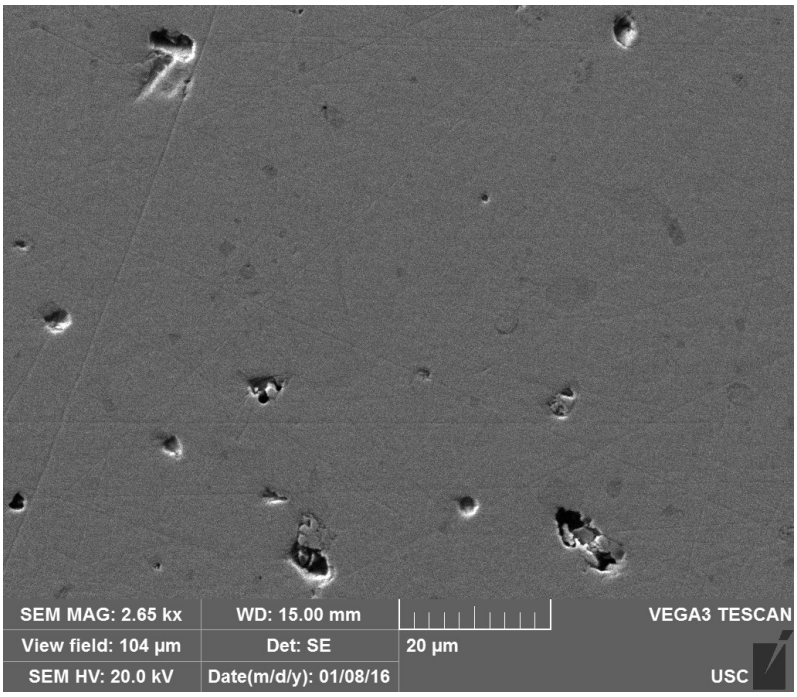

Figure 5.30: Tile--SE image (x2650 magnification)

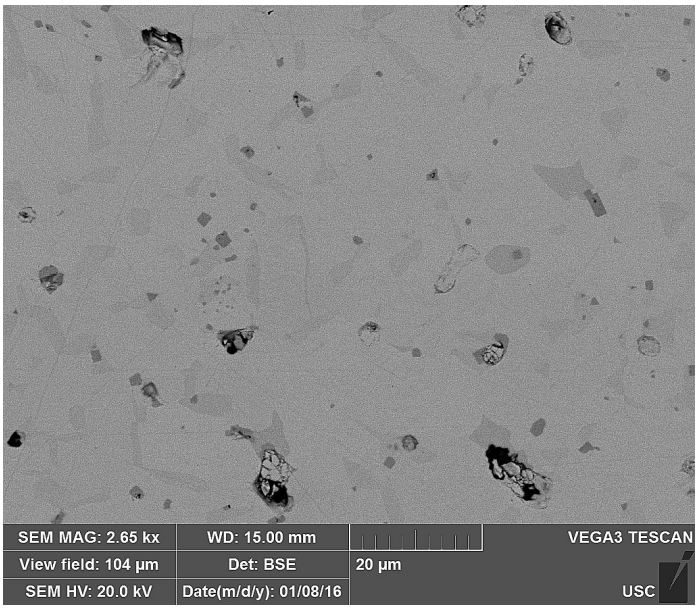

Figure 5.31: Tile--BSE image (x2650 magnification)

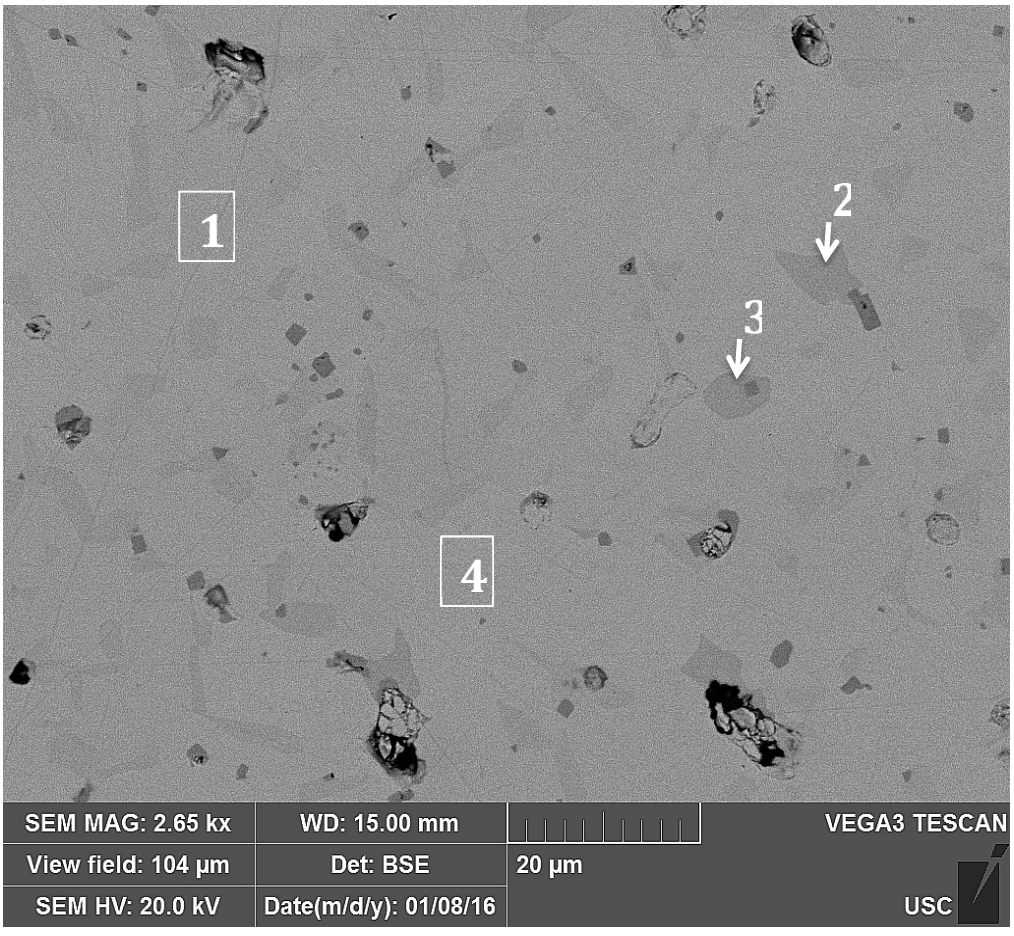

Figure 5.32: EDX was performed on four regions of the Tile sample.

Table 5.29: EDX composition results for the three regions shown in Figure 5.32.

	Area 1	Point 2	Point 3	Point 4
Wt % U	92.66	98.36	89.83	93.75
Wt % Si	7.35	0	10.16	6.27
Wt % O	0	0.13	0	0
Composition	U_3Si_2	UO_2	USi	U_3Si_2

The bulk material in the Tile was identified at U_3Si_2. Second phases in the Tile specimen appear to lie along grain boundaries. The light grey precipitate at point 2 was Uranium rich. It is unlikely that the phase is pure uranium metal; instead, UO_2 is the more likely the composition. Point 3 was identified as USi. Regions of UO_2 were also identified in pellets B and C. USi was identified in pellet A.

Conclusion:

EDX was performed on each sample and confirmed the base material was U_3Si_2. Each sample exhibited second phase precipitates, which are summarized in Table 5.30. The second phase precipitates in Figures 5.25 and 5.31 appear to lie along grain boundaries. If the second phase precipitates in U_3Si_2 do in fact lie along grain boundaries, they will pin them during diffusion processes. Most notably, grain boundary creep in the thermal regime would be hindered. The second phases would not inhibit creep in the irradiation regime since creep occurs within the grain itself, as defects are created and made mobile. With the exception of U_3Si_5, all of the U-Si second phases have a melting temperature lower than that of U_3Si_2. The U-Si second phases could degrade the fuel structure if a commercial U_3Si_2 fuel rod were to experience an unforeseen rise in temperature (LOCA, RIA, etc.).

Relative to pellets A and B, and the Tile sample, Pellet C shows better diffusion as noted by the high surface tension of it's precipitates (spherical shape). The spherical shape of the second phase precipitates also may imply that at the higher sintering temperature, the second

phase was molten. Overall, the high frequency of second phase precipitates shows that the fabrication process needs refinement. In order to consider this U_3Si_2 fuel "high quality" and high purity, the number of second phase precipitates need to be reduced. Sintering under vacuum, and reducing the excess silicon content used in producing the U_3Si_2 arc-melted buttons, should yield higher purity samples. The fact that such care is needed in the fabrication process to avoid formation of second USi_x and oxide phases presents a challenge when scaling up to commercial fabrication. Additional EDX analysis was performed on the areas surrounding Vickers indentations. These results are discussed in the upcoming section on hardness and toughness testing.

Table 5.30: Summary of Second Phases

Second Phase Precipitates	
Pellet A	USi, U_3Si_5
Pellet B	USi_3, UO_2, U_3Si_2O
Pellet C	UO_2, USi_3
Tile Sample	USi, UO_2

5.7 Elastic Properties:

Impulse excitation technique was used to determine the Young's and Shear Moduli of a tile specimen, which allowed for the determination of the Poisson ratio of U_3Si_2.

A U_3Si_2 tile specimen (shown in Figure 5.33) was used to determine elastic properties of U_3Si_2 at room temperature. The tile geometry is summarized in Table 5.31. Using ASTM E 1876, the flexural frequency can be related to the Young's modulus of a material if the density and geometry is known. Similarly, the torsional frequency is related to the Shear Modulus. Depending upon whether flexural frequency or torsional frequency was measured, the sample was positioned on support wires as in the configurations shown in Figures 5.34 and 5.35.

Although three U_3Si_2 specimens were shipped to USC from INL, only one survived transport intact. This limited the testing to a single sample. Given that the tile was fabricated using the same feed stock and sintering conditions as the tile used in grain size and pore size analysis, the microstructure is comparable. Thus, the specimen used for impulse excitation is expected to be around 96.5 % TD.

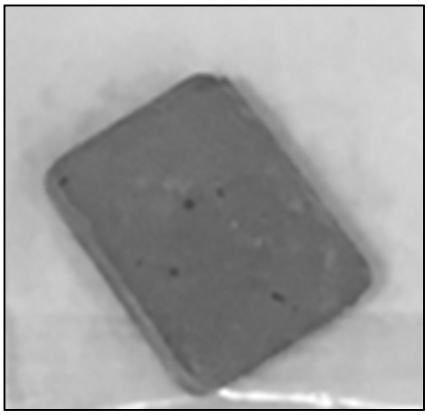

Figure 5.33: U_3Si_2 tile specimen

Table 5.31: U_3Si_2 tile specimen geometry

Sample	
Dimensions	
Length (mm)	20.5
Mass (g)	9.91073
Thickness (mm)	3.0
Width (mm)	15.7

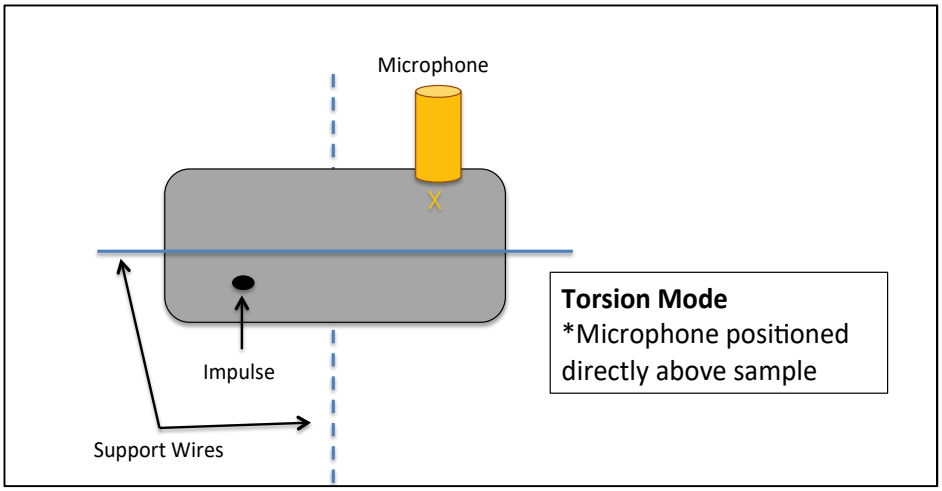

Figure 5.34: Position of tile sample relative to support wires, impulse (hammer tap), and microphone for measuring torsional frequency

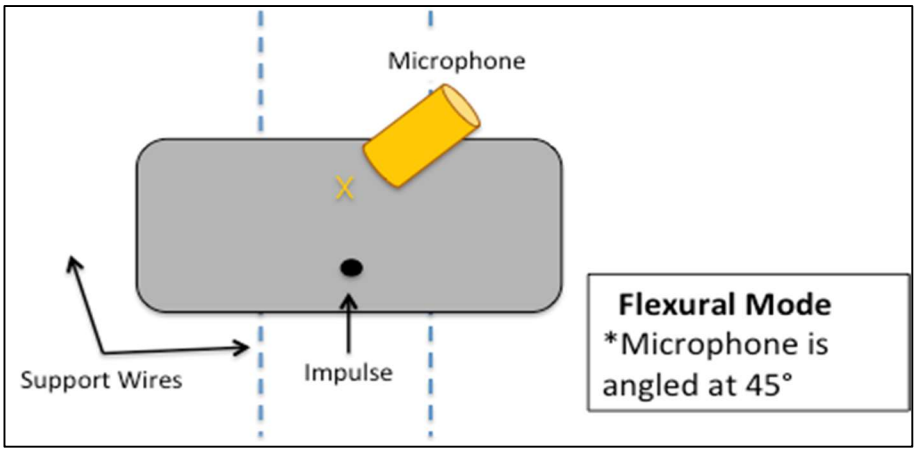

Figure 5.35: Position of tile sample relative to support wires, impulse (hammer tap), and microphone for measuring flexural frequency.

Eighty measurements were taken in both flexural and torsion modes. Additionally, the microphone and "hammer" were moved around the sample to check for repeatability throughout the sample at different nodes and antinodes. . After the resonant frequency was identified for flexural and torsion modes, ASTM E 1876 was used to calculate both Young's and Shear Moduli.

Elastic Modulus:

$$E = 0.9465 \cdot \left(\frac{m \cdot f_f^2}{b}\right) \cdot \left(\frac{L^3}{t^3}\right) \cdot T_1$$

E = Young's Modulus, Pa
m = Mass of the bar, g
L = length of the bar, mm
t = thickness of the bar, mm
f_f = Fundamental flexural resonant frequency of bar, Hz
T_1 = Correction factor for fundamental flexural mode to account for finite thickness of bar, Poisson's ration, etc.

$$T_1 = 1 + 6{,}585 \cdot (1 + 0.0752\nu^2) \cdot \left(\frac{t}{L}\right)^2 - 0.868\left(\frac{t}{L}\right)^4 - \left[\frac{8.340 \cdot (1 + 0.2032\nu) \cdot \left(\frac{t}{L}\right)^4}{1.000 + 6.338 \cdot (1 + 0.1408\nu + 1.53\nu^2) \cdot \left(\frac{t}{L}\right)^2}\right]$$

Where ν is Poisson ratio

Shear Modulus:

$$G = \frac{4 \cdot L \cdot f_t^2}{b \cdot t}\left[\frac{B}{1 + A}\right]$$

G = Shear Modulus, Pa
m = Mass of the bar, g
L = length of the bar, mm
b = width of the bar, mm
t = thickness of the bar, mm
f_t = Fundamental torsional resonant frequency of bar, Hz
B = Correction factor
A = Empirical correction factor based on the width-to-thickness ratio

$$B = \left[\frac{\frac{b}{t} + \frac{t}{b}}{4 \cdot \left(\frac{t}{b}\right) - 2.52 \cdot \left(\frac{t}{b}\right)^2 + 0.21\left(\frac{t}{b}\right)^6}\right]$$

$$A = \frac{\left[0.5062 - 0.8776 \cdot \left(\frac{b}{t}\right) + 0.3504 \cdot \left(\frac{b}{t}\right)^2 - 0.0078 \cdot \left(\frac{b}{t}\right)^3\right]}{\left[12.03 \cdot \left(\frac{b}{t}\right) + 9.892 \cdot \left(\frac{b}{t}\right)^2\right]}$$

The sample was first tested in torsion mode in order to determine the torsional frequency. Following testing in torsional mode, the sample was tested in flexural mode.

After approximately thirty tests in flexural mode, a small chip was noticed near the corner of the tile and removed. Testing was resumed. The results for Young's and Shear modulus based on all test results are shown in Figure 5.36.

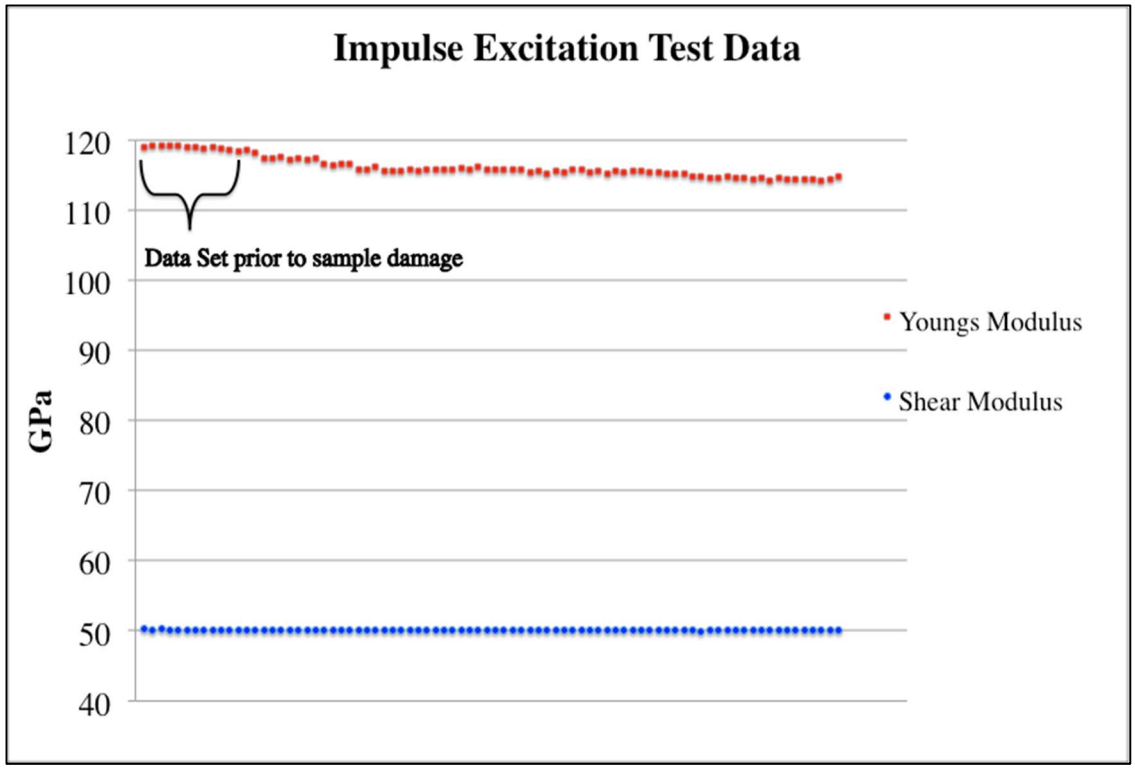

Figure 5.36: Young's Modulus and Shear Modulus as determined by impulse excitation technique. Data points are for 80 individual tests in both torsional and flexural modes.

The average Young's modulus and Shear modulus were used to calculate the Poisson ratio for U_3Si_2. Results of all test data are summarized in Table 5.32.

Table 5.32: Elastic Properties of U_3Si_2

All Test Data		
Average E (GPA)	Average G (Gpa)	Poisson Ratio
116.1 ± 1.5	50.2 ± 0.3	0.156 ± 0.002

It is likely that the visible chip in the sample was present before it was visible in the sample. The best estimation for Young's modulus data prior to damage or cracking is obtained if only the first fifteen tests are used. This data set is shown in Figure 5.36. An updated calculation for Young's modulus and Poisson ratio is summarized in Table 5.33.

Table 5.33: Elastic Properties of U_3Si_2 as determined from impulse excitation—updated Young's Modulus

Using Data Prior to Damage for Young's Modulus		
Average E (GPA)	Average G (Gpa)	Poisson Ratio
119.1 ± 0.1	50.2 ± 0.3	0.186 ± 0.001

Literature values for the room temperature elastic properties of U_3Si_2 are provided by [Shimizu 1965, Taylor 1961, and Bauer 1962]. Shimizu provides Young's modulus values of 52.4 GPa for arc cast samples and a range of 63-140 GPa for induction cast samples. Bauer provides a value of 138 GPa for the Young's modulus of arc cast samples. Only Taylor and McMurtry tested sintered samples. Whereas Shimizu and Bauer only provided a value of Young's modulus, Taylor provides Young's and Shear moduli, as well as Poisson ratio over a range of sample densities. Given the similar fabrication route, Taylor's data is most appropriate for comparison to USC results. Two graphs of Young's and Shear Modulus as a function of percent theoretical density have been reproduced from Taylor's annual report [Taylor 1961] and are provided in Figures 5.37 and 5.38. In each Figure a dashed black trend line was drawn through the data points. The lowest two points were considered outliers on the graph of Young's modulus and not used to construct the trend line. Red dashed lines illustrate the intersection of the trend line with the approximate density (97%) of the USC tile sample. The Taylor data suggests that a 97%TD sample would have a Young's modulus of approximately 17.5 x 10^6 PSI or 120 GPa. Similarly, the Taylor data suggests that a 96.5%TD sample would have a Shear

modulus of approximately 7.25 x 10^6 PSI or 49.98 GPa. These values agree very well with the results obtained at USC for both the Young's modulus and Shear modulus of U_3Si_2. The Poisson ratio obtained using the USC data is also within the range expected using the Taylor data. A reproduced Table of Poisson ratio as a function of % Theoretical density is given in Table 5.34.

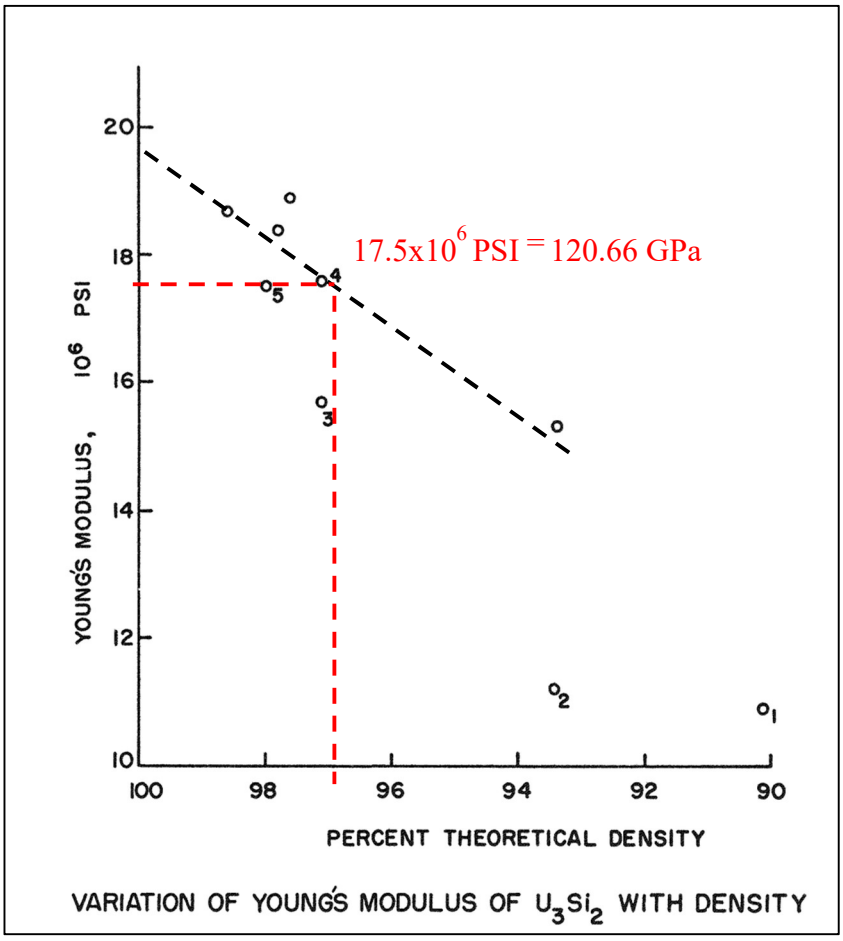

Figure 5.37: Variation of Young's Modulus with Density
Taken from Taylor-McMurtry annual report [Taylor 1961].

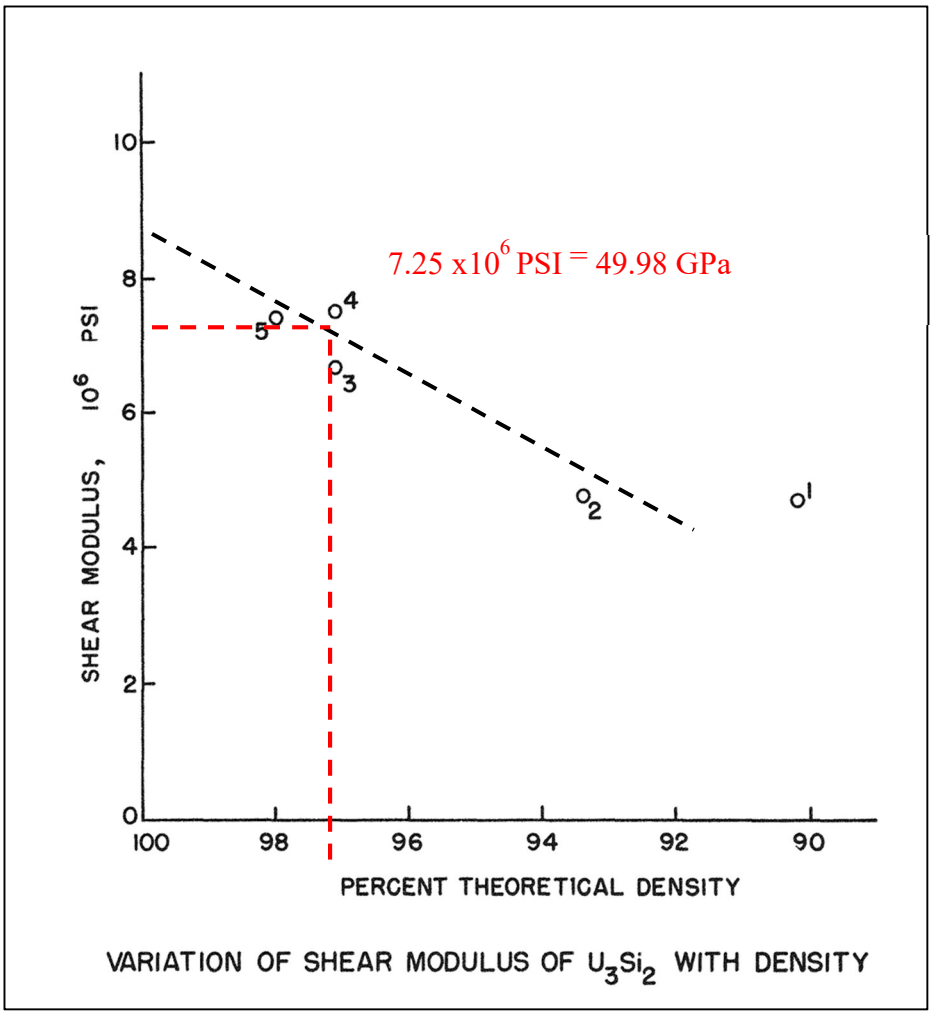

Figure 5.38: Variation of Shear Modulus with Density
Taken from Taylor-McMurtry annual report [Taylor 1961].

Table 5.34: Poisson Ratio for different density U3Si2 specimens.
Reproduced from Taylor-McMurtry annual report [Taylor 1961]

Bar Number	% Theoretical Density	Poisson Ratio
1	90.2	0.161
2	93.4	0.181
3	97.1	0.179
4	97.1	0.185
5	97.7	0.185

It should be noted that the ASTM standard is for a rectangular bar shaped specimen.

Chamfered edges and rounded corners of a tile can reduce the cross sectional moment of inertia

and slightly alter the relationship between density and the physical dimension of the bar. Quinn & Swab describe a correction factor for rounded edges in the calculation of Young's modulus by impulse excitation device [Quinn 2000]. The correction factor includes terms for the inertia of a perfect rectangular beam (I_b) and the inertia of rounded edge beam (I_t). This correction factor can be applied to the value of Young's Modulus previously calculated in order to see the effect of the rounded edges. In addition to the known sample geometry, the radius of the curved edge is required to calculate the correction factor. For the tile sample, the radius of the curved edge was found to be 1.0 mm. Using these values and the following equations for the inertia of a perfect rectangular beam (I_b) and inertia of rounded edge beam (I_t), it is possible to calculate the corrected Young's modulus (E_{cor}). For the following equations, *m* is the mass, *b* the length of the bar, *d* the width, *l* the thickness, and *r* is the radius of the curved edge.

Moment of Inertia for a rectangular beam: $I_b = \frac{bd^3}{12}$

Moment of Inertia for a rounded edge beam: $I_b = \frac{b(d-2r)^3}{12} + \frac{(b-2r)r^3}{6} + \frac{(b-2r)(d-r)^2 r}{2} + +4r^2\left(\frac{\pi}{16} - \frac{4}{9\pi}\right) + \pi r^2\left[\frac{d}{2} - r\left(1 - \frac{4}{3\pi}\right)\right]^2$

Corrected Young's Modulus: $E_{cor} = \left(\frac{I_b}{I_t}\right) E_{b,m}$

Using the values summarized in Table 5.35, the correction factor is found to be 1.0076. When 1.01 is multiplied to the Young's modulus given in Table 5.33 (119.1 GPa), the corrected Young's modulus becomes 120.01 GPa. This is a minimal increase in the value of Young's modulus and still agrees with Taylor's literature value of 120.66 GPa for a ~97%TD sample.

Table 5.35: Values used to calculate correction factor

Sample Description	
Length	20.5 mm
Mass	9.91073 g

Thickness	3.0 mm
Width	15.7 mm
Radius of edge	1 mm
I_b	6611.0681 mm^4
I_t	6561.1068 mm^4
I_b/I_t (Correction)	1.0076

There is a similar correction factor for treatment of chamfered edges when calculating Shear modulus described Morrell in a National Physical Laboratory report [Morrell, 2015]. While the previous correction factor for Young's modulus is based on first principles, the correction factor for Shear modulus is the result of a parametric fit of numerous data points. Additionally, the Shear modulus correction is valid only for chamfered edges. Given that the USC sample has rounded corners rather than chamfered edges, this correction factor should be taken as an estimate. Morrell's correction factor includes terms for the length, width, and chamfer size of the sample. Since the curved edge radius of the tile sample was found to be 1.0 mm, a chamfered edge of 1.0 mm is used in the calculation of chamfered edge. In reality, a comparable chamfer size would be less than 1.0 mm; however, since this correction factor is an estimate, the 1.0 mm value was carried over from the Young's modulus correction. For the following equations, *t* is the width, *b* the length of the bar, and *c* is the length of a 45° chamfer.

Shear Modulus Correction Factor: $\frac{G_c}{G_0} = \left(-3.861\left(\frac{t}{b}\right)^2 + 3.474\left(\frac{t}{b}\right) - 0.2623\right)\left(\frac{c}{t}\right)^2 + \left(0.194\left(\frac{t}{b}\right) - 0.001\right)\left(\frac{c}{t}\right) + 1$

Using the above equation, the Shear modulus correction factor for a chamfer size of 1.0 mm is found to be 1.0099. When 1.01 is multiplied to the Shear modulus given in Table 5.33 (50.2 GPa), the corrected Young's modulus becomes 50.69 GPa. This is a minimal increase in the value of Shear modulus and is an overestimate of Shear modulus since the correction factor is given for chamfered rather than rounded edges. It was mentioned previously that a comparable

chamfer size should be less than that of a rounded edge radius of 1.0mm. The actual chamfer size generated by a 1.0mm rounded edge is more likely on the order of 0.25-0.5 mm. This range would generate correction factors ranging from 1.0024 to 1.0048, respectively. Similarly, these correction factors increase the Shear modulus by 0.1 GPa and 0.2 GPa, respectively. These fall within the uncertainly of the Shear modulus measurement (50.2 ±0.3 GPa).

It should be noted that both [Quinn, 2000 and Morell, 2015] include two correction factors; one for correction of missing mass, and the other for correction of missing density. I have spoken with the authors of each report and they both stated that the correction for density is not valid; rather density effects are naturally included in the mass correction. Using both correction factors would be inherently flawed. Both authors advised me that their reports are currently being revised to reflect these recent changes.

Following the test on the tile sample, the sample was squared off to dimensions of 14.7 mm x 14.5 mm (see Figure 5.39). The sample was again tested using impulse excitation technique. However, after extensive testing it was determined that reducing the sample dimensions prevented the identification of the flexural or torsional frequency. Without determination of the flexural and torsional frequencies, it was impossible to determine the elastic properties.

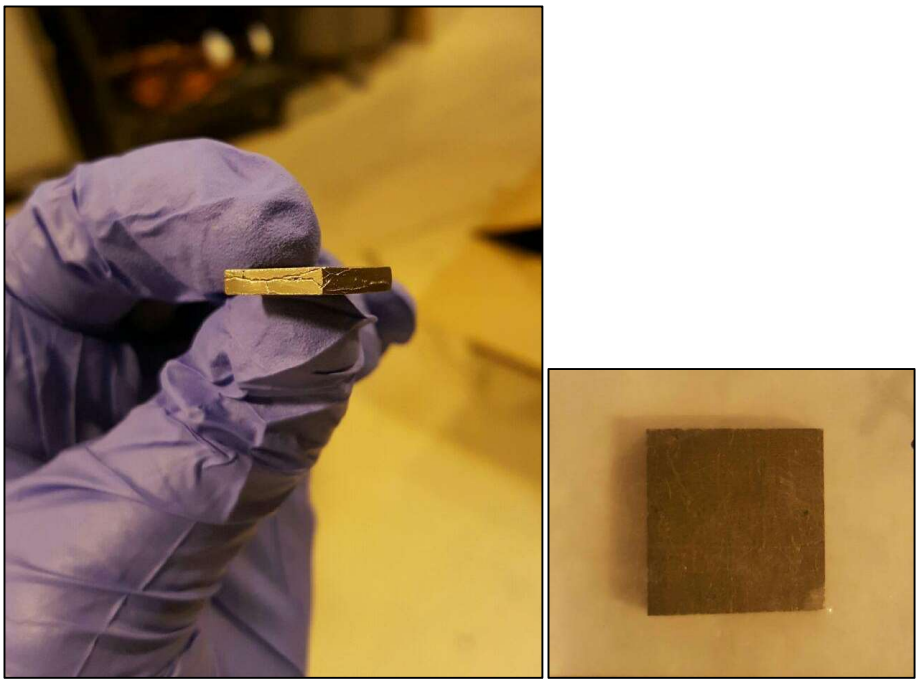

Figure 5.39: Tile sample after being squared off to 14.7 mm x 14.5 mm.

5.8 Electrical Resistivity Measurement:

Electrical resistivity of samples was measured using the four-point probe method. A Cascade Microtech C4S-47/0O four-point probe tip was used in conjunction with a Gamry 600 potentiostat. The C4S-47/0O four-point probe tip is made from Tungsten Carbide, has inner probe spacing of 1mm, and requires a loaded weight between 70-180g.

A fixture was built for the four-point probe tip and connected to a sample holder (see Figure 5.40). The sample holder featured an adjustable height stand for samples of varying height. The probe tip was fixed to an polycarbonate beam, which allowed for the addition of weight during testing. This fixture system ensured that the probe tip and sample remain perfectly level throughout testing. The U_3Si_2 samples were mounted in a nonconductive epoxy and polished prior to resistivity measurements. For all tests, 180g weights were added to the top of the probe. The addition of weight ensures proper contact between the probe tips and the sample surface.

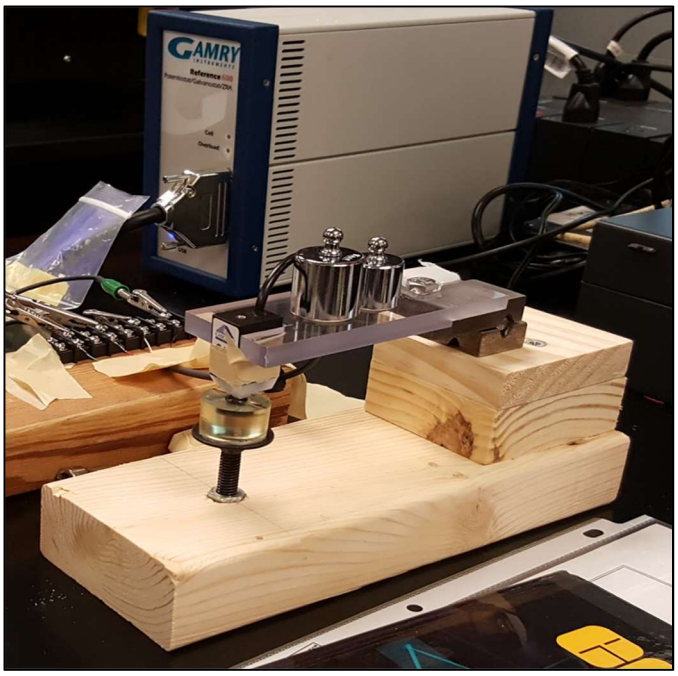

Figure 5.40: Four point probe setup.

A silicon wafer from University Wafers was used to perform a calibration. The wafer has dimensions of 24.85 mm x 23.37 mm x 0.47mm and quoted resistivity of 0.01-0.02 ohm-cm.

For an infinitely thin sheet (thickness much less than probe spacing), the sheet resistivity is related to the sheet thickness (t), measured voltage (V) and applied current (I) and by the following equation:

$$\rho = \frac{\pi}{\ln 2} \cdot t \cdot \frac{V}{I}.$$

For samples of finite width and non-negligible thickness, the above equation must be multiplied by correction factors F_1 and F_2.

$$\rho = \frac{\pi}{\ln 2} \cdot t \cdot \frac{V}{I} \cdot F_1 \cdot F_2$$

The thickness correction factor, F_1, is given by

$$F_1 = \frac{\ln(2)}{\ln\left[\frac{sinh\left(\frac{t}{s}\right)}{sinh\left(\frac{t}{2s}\right)}\right]}$$

where t is the thickness of the sample and s is the spacing between probe tips.

The finite width correction factor, F_2, is taken from Table 1 in [Smits 1958].

TABLE I — CORRECTION FACTOR C FOR THE MEASUREMENT OF SHEET RESISTIVITIES WITH THE FOUR-POINT PROBE

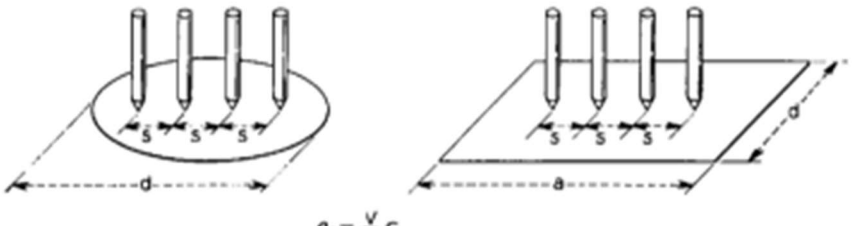

$\rho_s = \frac{V}{I} C$

d/s	circle diam d/s	a/d = 1	a/d = 2	a/d = 3	a/d ≥ 4
1.0				0.9988	0.9994
1.25				1.2467	1.2248
1.5			1.4788	1.4893	1.4893
1.75			1.7196	1.7238	1.7238
2.0			1.9454	1.9475	1.9475
2.5			2.3532	2.3541	2.3541
3.0	2.2662	2.4575	2.7000	2.7005	2.7005
4.0	2.9289	3.1137	3.2246	3.2248	3.2248
5.0	3.3625	3.5098	3.5749	3.5750	3.5750
7.5	3.9273	4.0095	4.0361	4.0362	4.0362
10.0	4.1716	4.2209	4.2357	4.2357	4.2357
15.0	4.3646	4.3882	4.3947	4.3947	4.3947
20.0	4.4364	4.4516	4.4553	4.4553	4.4553
40.0	4.5076	4.5120	4.5129	4.5129	4.5129
∞	4.5324	4.5324	4.5324	4.5325	4.5324

Figure 5.41: Table 1 from Smits 1958 "Measurement of Sheet Resistivities with the four-point probe."

Linear interpolation was used to determine the appropriate correction factors for U_3Si_2 and Silicon wafer samples. The Smits correction factor for finite width already includes the $\frac{\ln(2)}{\pi}$ term. Thus, the equation for resistivity is reduced to:

$$\rho = t \cdot \frac{V}{I} \cdot F_1 \cdot F_2 \ .$$

The thickness of the Silicon wafer was negligible and only a correction for finite width was required. The correction factor for a 24.85 mm x 23.37 mm rectangle of finite width and length is 4.4619. A current of 0.006A was applied for all measurements on the Silicon wafer. The measured voltage and associated resistivity is summarized in the following table. The average value of resistivity is 0.0144 ± 0.00007 ohm-cm, which agrees with the range quoted by University Wafers (0.01-0.02 ohm-cm).

Table 5.36: Voltage across Si Wafer

Silicon Wafer		
Test #	Voltage (μV)	Resistivity (ohm-cm)
1	0.4148	0.0145
2	0.4138	0.0145
3	0.4113	0.0144
4	0.4125	0.0144
5	0.4084	0.0143
6	0.4155	0.0145
7	0.4100	0.0143
8	0.4132	0.0144
9	0.4135	0.0145
10	0.4135	0.0145
Average:	0.4126 ± 0.0022	0.0144 ± 0.00007

The sample geometries used to calculate the correction factors for U_3Si_2 samples are summarized in Table 5.37. Correction factors are given in Table 5.38.

Table 5.37: Dimensions used to calculate resistivity correction factors in U_3Si_2 samples.

Dimensions (mm)

	A	B	C	Tile Y
Thickness (t)	4.20	3.20	3.50	2.80
Diameter (d)	8.20	8.40	8.10	-----
Length (parallel to probe line) (a)	-----	-----	-----	19.2
Width (d)	-----	-----	-----	15.5
Probe Spacing (s)	1.00	1.00	1.00	1.00

Table 5:38: Correction factors for sample thickness and finite width in U_3Si_2 samples.

Correction Factors:				
	A	B	C	Tile Y
Thickness correction (F1)	0.328	0.423	0.389	0.475
Finite width correction (Smits-Table 1) (F2)	3.996	4.015	3.986	4.396
Total Correction Factor (F1*F2)	1.310	1.697	1.552	2.088

Given the good results using the Silicon wafer, the same testing method was applied for U_3Si_2 samples. Testing consisted of applying a 0.6 A current to the outer two probes of the probe tip for twenty seconds. The voltage was measured each second across the two inner probes, for a total of twenty measurements. The twenty measurements were averaged for each test. Tests were repeated ten times per sample, which provided an average voltage reading across each sample. Voltage results are summarized in Table 5.39.

Table 5.39: Voltage across surface of samples

	Voltage (mV) (Each Test averaged over 20 seconds)			
Test #	Pellet A	Pellet B	Pellet C	Tile
1	0.1240	0.1314	0.1141	0.1250
2	0.1392	0.1310	0.1213	0.1228
3	0.1214	0.1400	0.1170	0.1160
4	0.1216	0.1397	0.1284	0.1067
5	0.1211	0.1408	0.1257	0.1065
6	0.1318	0.1304	0.1258	0.1201
7	0.1387	0.1257	0.1335	0.1169
8	0.1272	0.1260	0.1347	0.1153
9	0.1320	0.1502	0.1333	0.1248
10	0.1330	0.1408	0.1179	0.1133
Average:	0.1290 ± 0.0069	0.1356 ± 0.0078	0.1252 ± 0.0074	0.1167 ± 0.0067

Using the results of Table 5.39, it is possible to calculate the resistivity for each sample. The results are shown in Table 5.40 and Figure 5.42.

Table 5.40: U_3Si_2 Resistivity Results

	Resistivity ($x10^{-4}$ Ω-cm)
Pellet A	1.18 ± 0.06
Pellet B	1.23 ± 0.07
Pellet C	1.13 ± 0.07
Tile Sample	1.14 ± 0.07

The results fall within the bounds of the literature values. The values are above those quoted by Shimizu and below those of Taylor and McMurtry. Shimizu found the room temperature electrical resistivity of arc cast U_3Si_2 was 1.05 x 10^{-4} Ω-cm [Shimizu 1965]. Taylor and McMurtry reported a value of 1.50 x 10^{-4} Ω-cm for U_3Si_2 [Taylor 1961] for 91- 93% TD sintered samples.

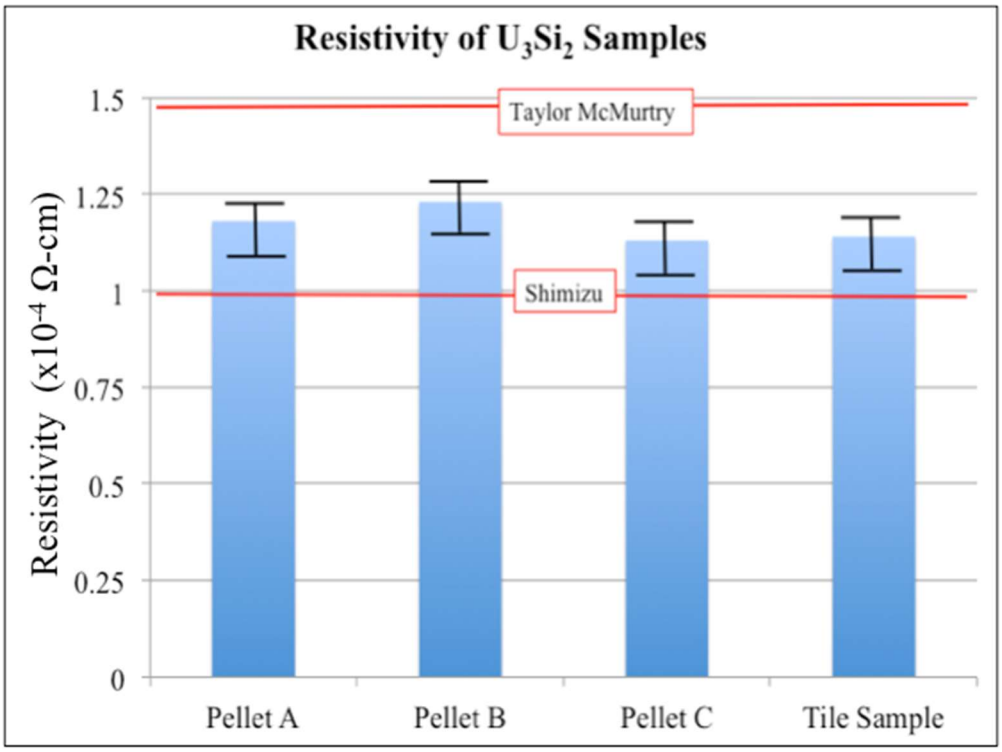

Figure 5.42: Resistivity of U_3Si_2 samples--Literature values shown in red.

Across the sample lot, there is slight a trend between resistivity and porosity. The resistivity increases with increasing porosity in the sample. This makes sense given the high resistivity of air within pores at the surface. These results are illustrated in Figure 5.43.

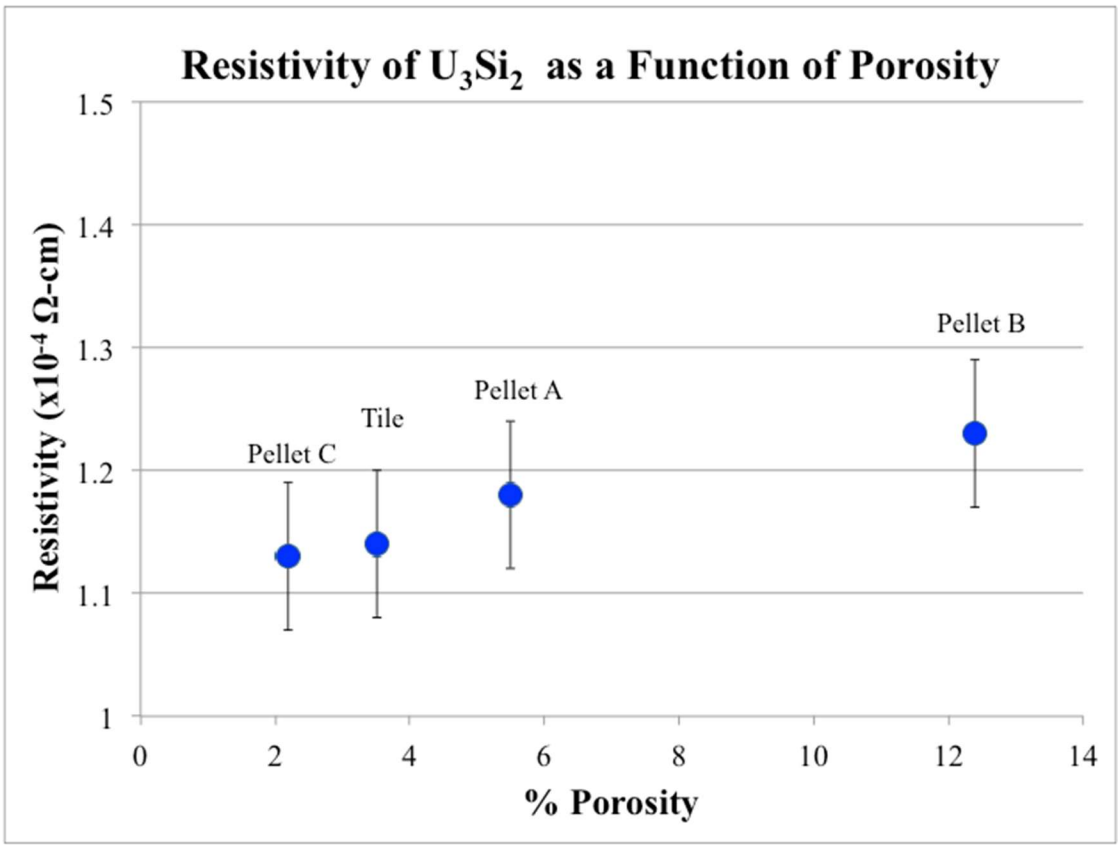

Figure 5.43: Resistivity of U_3Si_2 samples as a function of % porosity.

In addition to testing U_3Si_2, Shimizu also performed resistivity testing on U-Si samples of varying Si-content. His results are shown in Figure 5.43*. From the figure, it is clear that the electrical resistance increases with increasing silicon content. In reactor, as the uranium fissions, the percentage of silicon in the fuel will increase. The electrical resistivity will likely increase during irradiation in reactor.

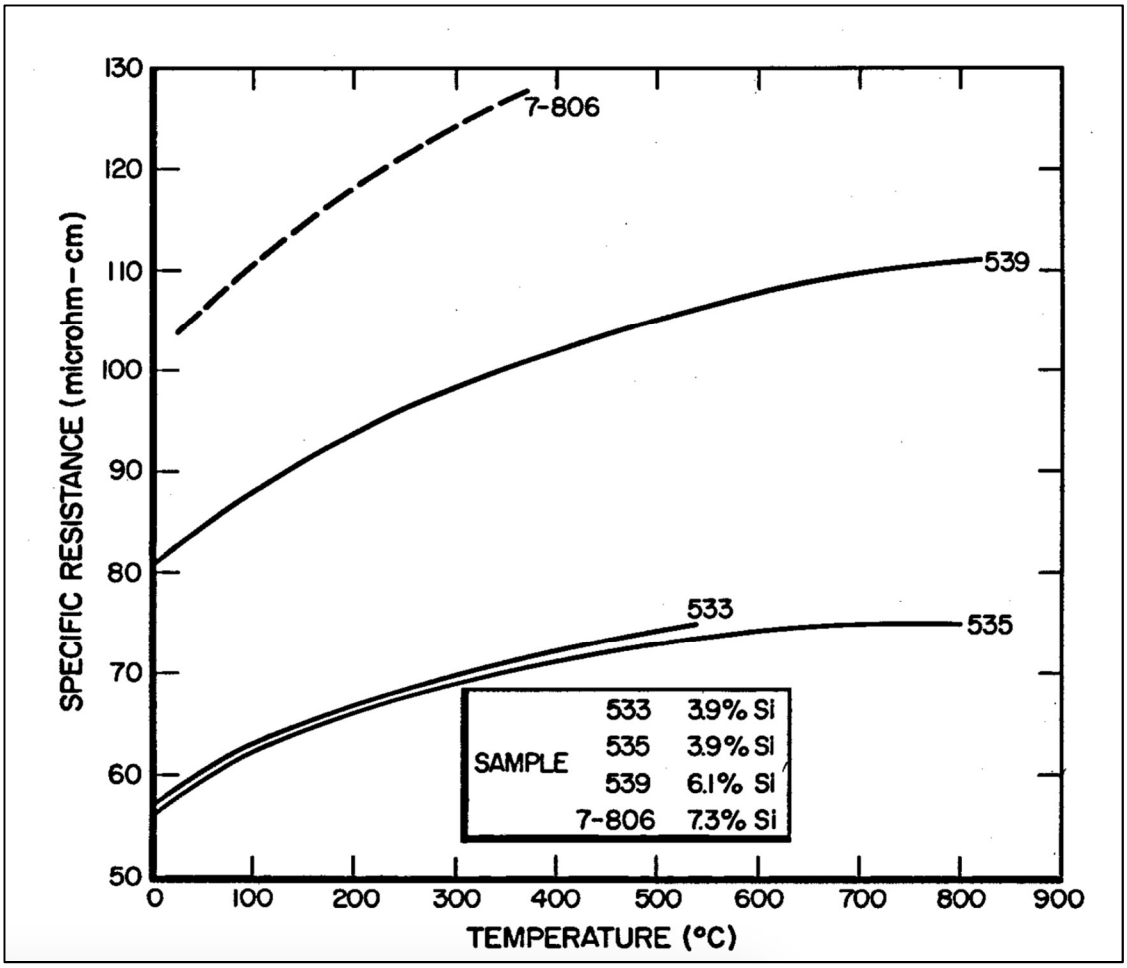

Figure 5.44: Resistivity of U-Si samples as a function of temperature. [Shimizu, 1965]

5.9 MECHANICAL PROPERTIES:

A Vickers microindentation characterization method was used to evaluate the mechanical properties of U_3Si_2. Specifically, indentation testing was performed on Pellets A, B, C, and the tile specimen. A calibration block was used to verify the operation of the microhardness tester. Preliminary indentation testing performed on SiC was compared to literature values to ensure reliability of results.

Vickers hardness testing across the sample was performed using a Beuhler Micromet-1 microhardness tester (Buehler Ltd, Lake Bluff, Illinois, USA) with loads of 2.9, 4.9, and 9.8 N and with a 10 s loading time. A total of 10 Vickers indentations were made in the prepared

sample at 3 load levels. Polarized light microscopy using a Keyence 5000x microscope was used to look at crack behavior through the surrounding microstructure in U_3Si_2. Additional SEM imaging was used to confirm indentation size. Indentation size and crack length were measured using ImageJ image processing software.

5.9.1 Hardness and Fracture Toughness:

The hardness of the material (Pa) is given by

$$H = \frac{P_{max}}{A_c}$$

where P_{max} is the peak indentation load in Newtons and A_c is the projected contact area in units of m^2. The Vickers hardness was also calculated using the expression

$$HV = 1.854 \times 10^6 \times \frac{F}{d^2}$$

where F is the force applied in units of kgf and d is the length of the indention diagonal in μm.

Fracture toughness (Pa√m) was calculated using the following relation [Li 1998, Li 2001, Venkaeswaran 2009]

$$K_{IC} = \alpha \left(\frac{E}{H}\right)^{1/2} \frac{P}{c^{3/2}}$$

where α is an empirical constant depending on the geometry of the indenter (0.016 for Vickers indenters), E is the elastic modulus (Pa), H is the Hardness (Pa), P is the peak indentation load (N), and c is the average length of all cracks emanating from the center of the indentation to the crack tip in meters.

A calibration block was used to verify the reliable operation of the Beuhler Micromet microhardness tester. The calibration standard stated that for a load of 1 kgf applied for 10

seconds, the Vickers Hardness should be 700 HV. Three indents were made in the sample and imaged using a Keyence microscope. The diagonals were then measured using ImageJ image processing software. The results confirmed the instruments operation. The average Vickers Hardness calculated for the 3 indentions was 702.01± 3.54.

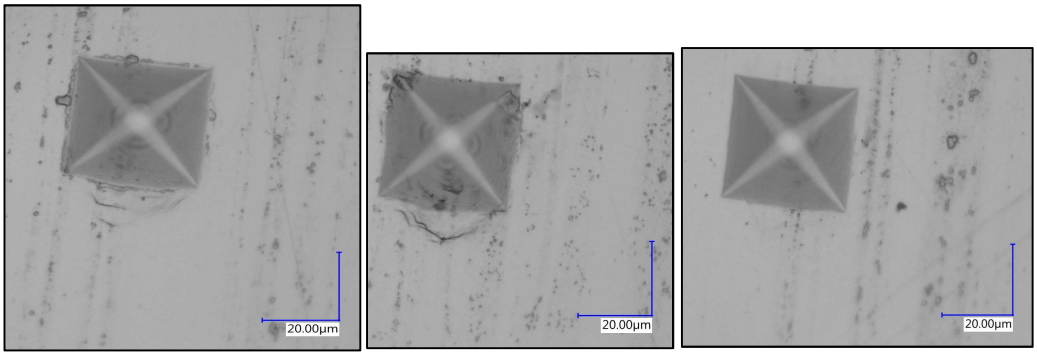

Figure 5.45: Calibration indentions 1, 2 and 3 (left to right).

Table 5.41: Hardness calibration using standard reference material

Hardness Calibration using Standard						
	D1 (µm)	D2 (µm)	Average D (µm)	F (kgf)	T (sec)	Vickers Hardness
Image 1	51.14	51.90	51.52	1	10	698.46
Image 2	51.65	51.13	51.39	1	10	702.01
Image 3	51.89	50.63	51.26	1	10	705.55
*Calibration Standard: Vickers Hardness should be 700HV at load of 1kgf applied for 10 sec						

Indentation Testing on SiC

An SiC sample was prepared for indentation testing by mounting the sample in epoxy and then grinding and polishing the sample to a mirror finish. A total of 8 indentations were made in the sample at 3 load levels. Indentation images in SiC were taken with a Keyence VHX-5000 series microscope. Figures 1-8 show Vickers indentations in SiC made using the load indicated in the Figure. The load time was 10 seconds for each indention.

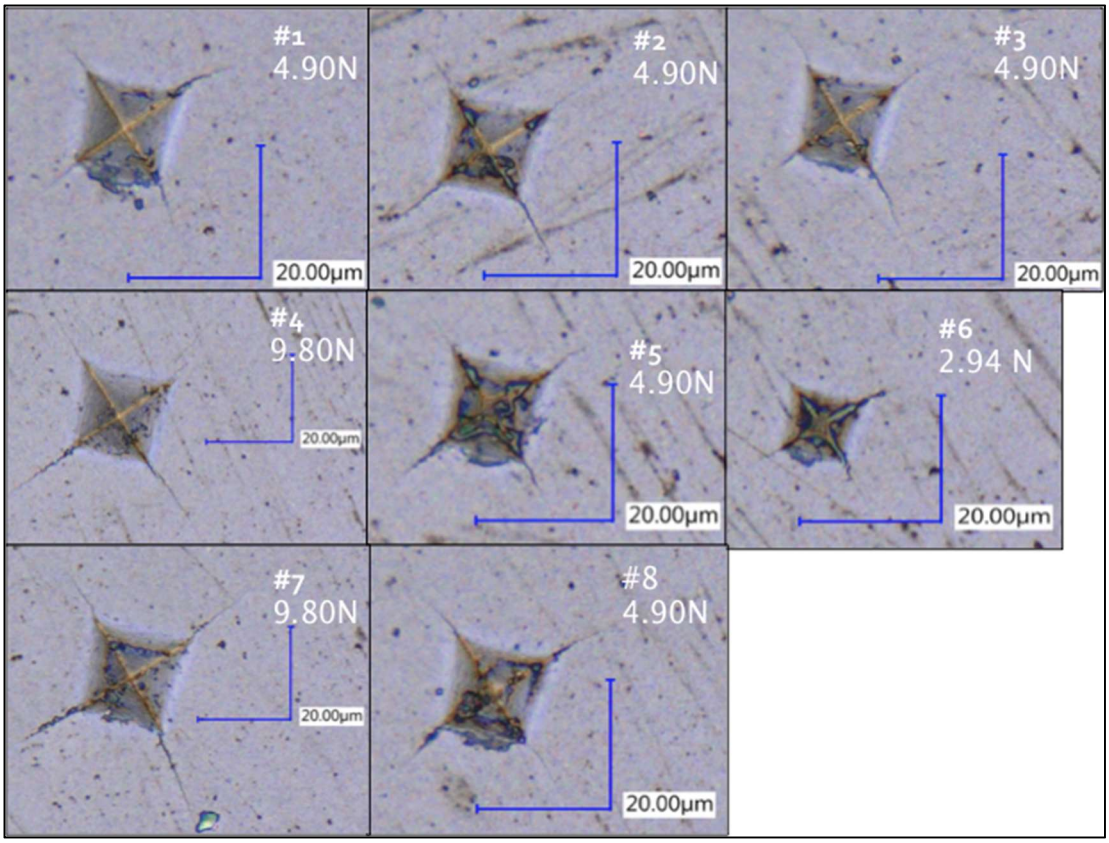

Figure 5.46: Indentions 1-8 in SiC sample

The area of the indentation, indentation diagonal lengths, and crack lengths were determined using ImageJ image processing software. The elastic modulus of SiC (415,000 MPa), required by the K_{IC} equation, was taken from [Munro 1997]. The results of SiC fracture toughness and hardness are summarized in the Table 5.42.

The average hardness for SiC was found to be 27.00 ± 1.75 GPa while the average toughness was found to be 4.10 ± 0.36 MPa √m. The hardness and toughness values compare well to literature values. The National Institute of Standards and Technology provides a hardness value of 26± 1 GPa at a testing load of 4.9 N (32 GPa at 9.8 N) and a toughness value of 3.1 MPa √m [Munro 1997]. The good agreement between results and literature values shows that the testing method is reliable.

Table 5.42: SiC Hardness and Toughness from Vickers Indentation (load held 10 sec)

	Force (kgf)	Load (N)	D 1 (μm)	D 2 (μm)	Indent Area (m^2)	Average Crack (m)	Hardness (MPa)	Vickers Hardness	Toughness (MPa √m)
1	0.5	4.90	19.50	19.10	1.98E-10	1.679E-05	24764	3288	4.67
2	0.5	4.90	19.61	18.82	1.76E-10	1.786E-05	27860	2905	4.01
3	0.5	4.90	18.93	19.78	1.68E-10	1.846E-05	29158	2722	3.73
4	1.0	9.81	27.40	27.20	3.79E-10	3.055E-05	25877	1986	3.72
5	0.5	4.90	18.70	19.26	1.75E-10	1.681E-05	28019	3279	4.38
6	0.3	2.94	14.00	13.90	1.01E-10	1.235E-05	29149	3650	4.09
7	1.0	9.81	27.32	29.09	3.89E-10	3.139E-05	25210	1882	3.62
8	0.5	4.90	19.68	19.50	1.89E-10	1.870E-05	25985	2652	3.88

5.9.2 Indentation Testing on U_3Si_2

Indentation testing was performed on Pellets A, B, C, and the tile specimen. Sample preparation required that all U_3Si_2 samples be mounted in epoxy and then ground and polished to a mirror finish. The polished samples were then chemically etched using a diluted Nitric acid wash (20 w/v%) to allow for grain imaging. A total of 12 indentations were made in each sample at 3 load levels. The following indentation images in U_3Si_2 were taken with a Tescan scanning electron microscope (SEM). The load time was 10 seconds for each indention.

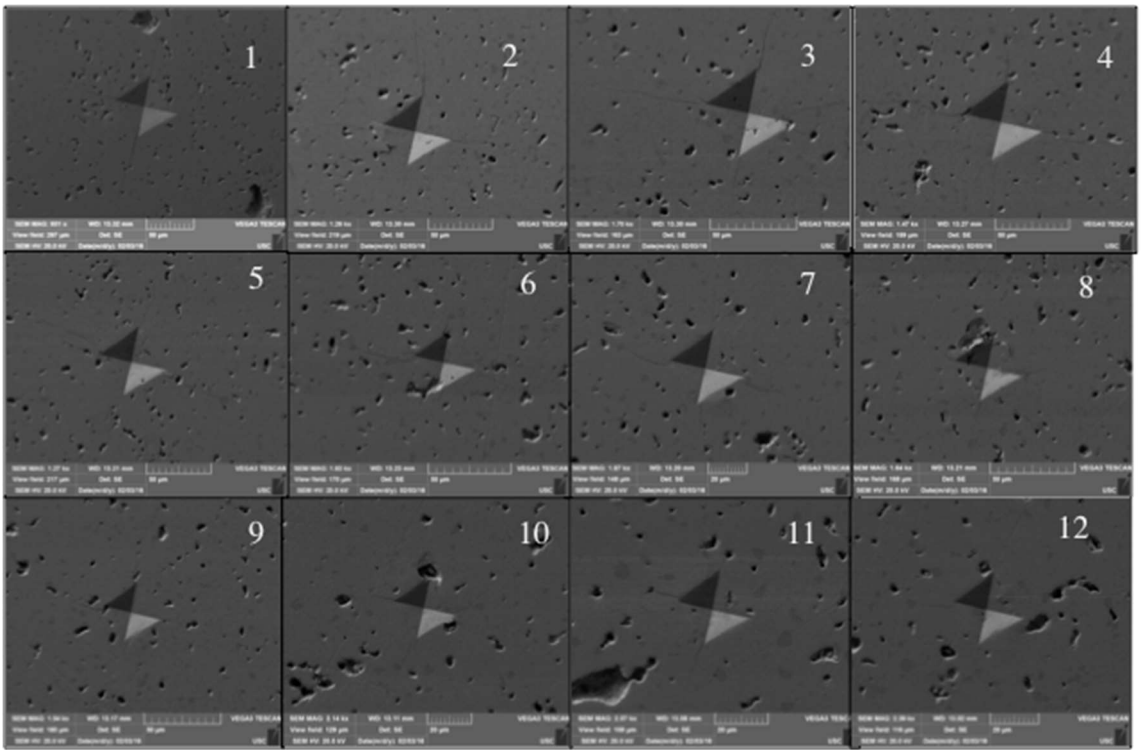

Figure 5.47: Indentations in Pellet A. Indents 1 through 4 (9.8 N); 5 through 8 (4.9 N); 9 through 12 (2.9 N)

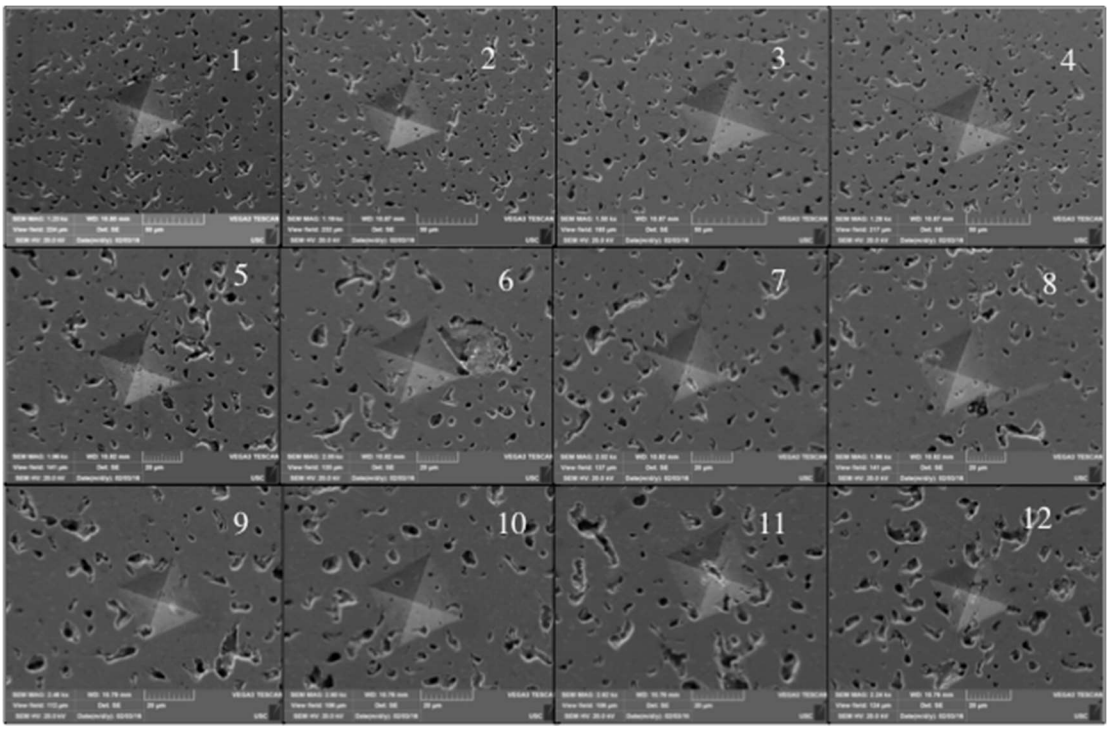

Figure 5.48: Indentations in Pellet B. Indents 1 through 4 (9.8 N); 5 through 8 (4.9 N); 9 through 12 (2.9 N)

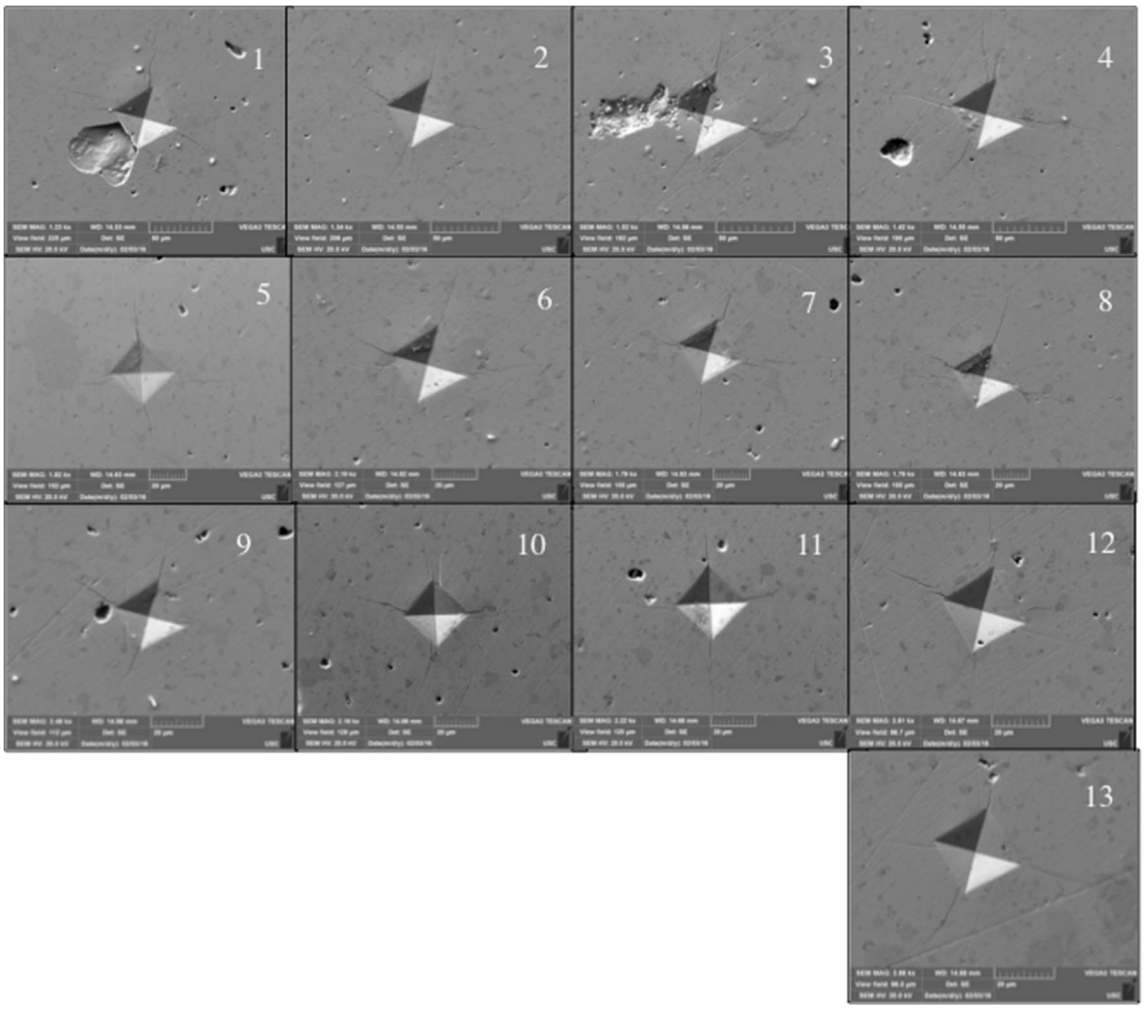

Figure 5.49: Indentations in Pellet C. Indents 1 through 4 (9.8 N); 5 through 8 (4.9 N); 9 through 13 (2.9 N)

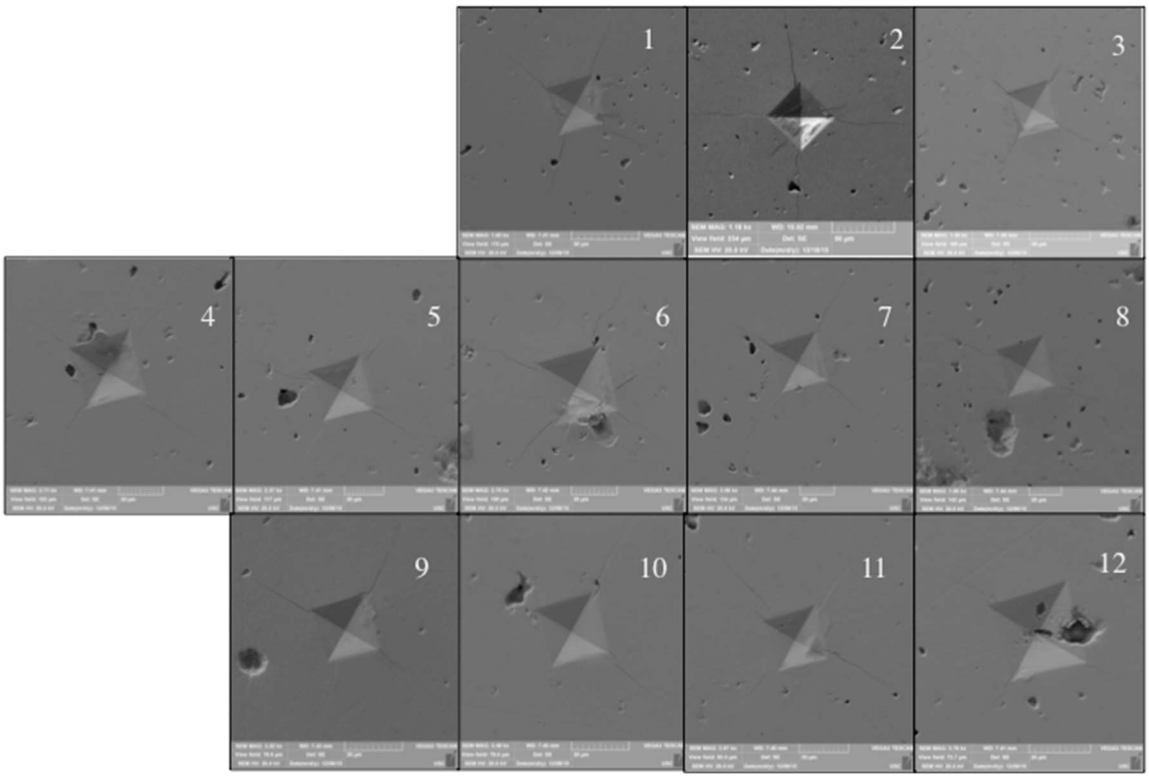

Figure 5.50: Indentations in Tile Sample. Indents 1 through 3 (9.8 N); 4 through 8 (4.9N); 9 through 12 (2.9 N)

The area of the indentation, indentation diagonal lengths, and crack lengths were determined using ImageJ post processing of SEM images. The elastic modulus of U_3Si_2, required by the K_{IC} equation, was taken from [Taylor 1961]. The Taylor data provides elastic modulus for various U_3Si_2 sample densities. Given that the density of the U_3Si_2 samples tested varied from one specimen to another, different values for Young's Modulus were used as well (See Table 5.43). The USC Young's Modulus data was only valid for the Tile specimen. However, since the USC value of Young's Modulus matches that of Taylor and McMurtry, there is no change in calculated toughness.

Table 5.43: U_3Si_2 Young's Modulus for %TD

Young's Modus using Taylor-McMurtry Data		
	% Theoretical Density	Young's Modulus (GPa)
Pellet A	94.5	105.14
Pellet B	87.6	74.12
Pellet C	97.8	120.66
Tile	96.5	113.76

The results of U_3Si_2 hardness and fracture toughness are shown in Figures 5.51 5.52, and 5.53 and are summarized in Table 5.44. There were several clear outliers within the toughness data sets, namely test numbers 7 and 10-13 for Pellet A, 10 for Pellet B, and 3 for Pellet C. Upon inspection of the SEM images, these indentions had interaction with neighboring pores, usually along the crack length. These data points were considered outliers and were removed from toughness analysis. The toughness is calculated using the density-dependent Young's Modulus values in Table 5.43. While the USC elastic modulus data is only valid for the Tile specimen, toughness is calculated for each sample using this value in order to show the variation in toughness across samples when Young's Modulus is held constant (Figure 5.53). A solid line shows the average value for each data set.

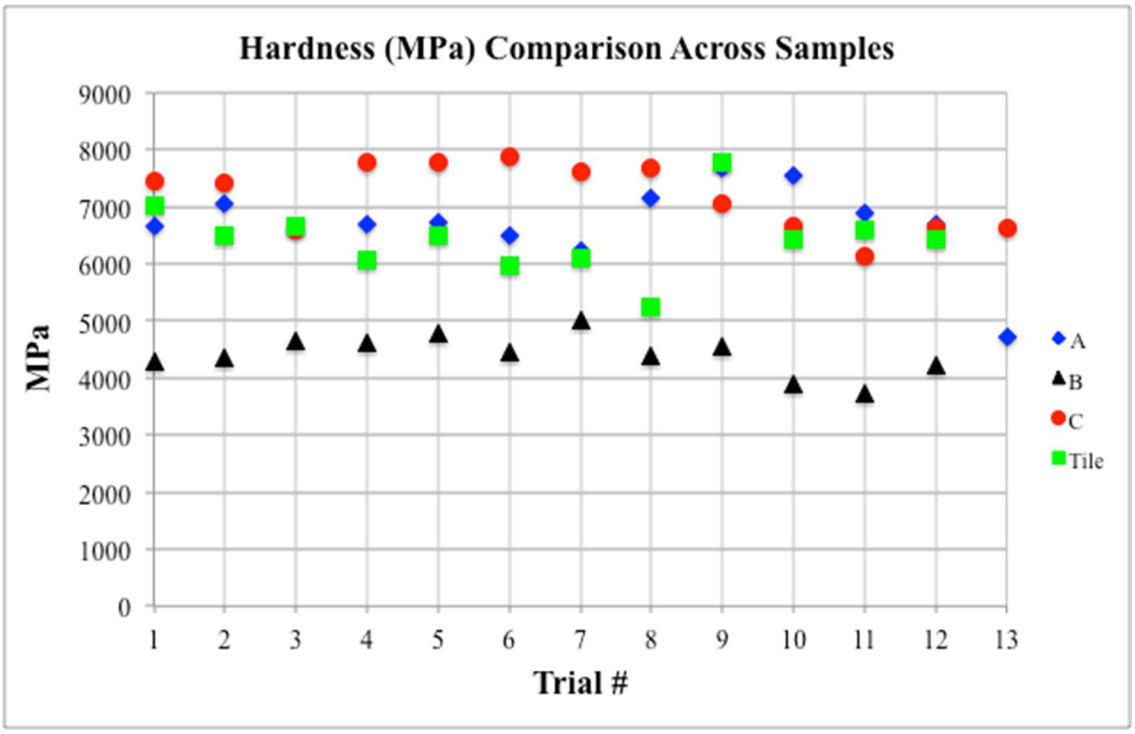

Figure 5.51: Hardness Results for U_3Si_2 (MPa)

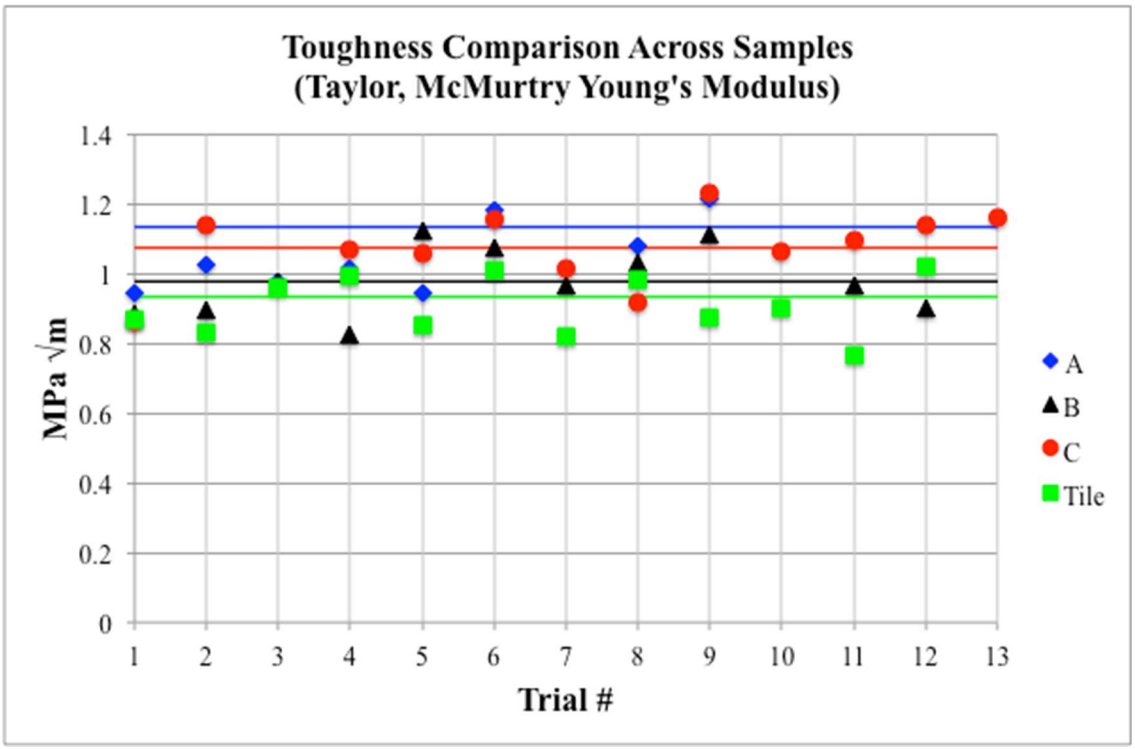

Figure 5.52: Toughness Results for U_3Si_2 (MPa√m) (Calculated using Taylor-McMurtry Young's Modulus Data)

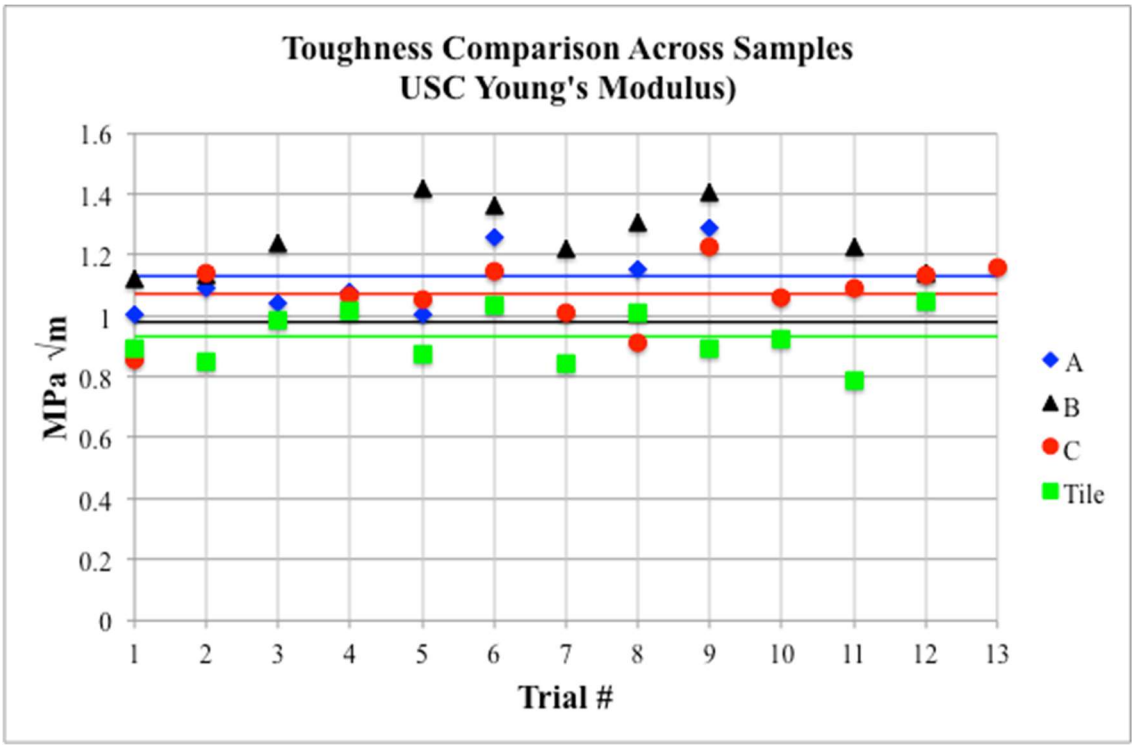

Figure 5.53: Toughness Results for U_3Si_2 (MPa√m) (Calculated using USC Young's Modulus Data)

Table 5.44: Data for U_3Si_2 Samples-Outliers Removed

	Toughness (Taylor McMurtry) (MPa √m)	Toughness-USC (MPa √m)	Hardness (MPa)	Vickers Hardness
A Averages:	1.110 ± 0.133	1.1668 ± 0.142	6710.30 ± 723. 38	652.147 ± 38.07
B Averages:	0.977 ± 0.098	1.238 ± 0.124	4411.78 ± 357.64	414.116 ± 34.00
C Averages:	1.075 ± 0.084	1.072 ± 0.084	7184.73 ± 587.07	678.311 ± 57.23
Tile Averages:	0.906 ± 0.084	0.930 ± 0.086	6443.90 ± 609.35	601.158 ± 85.34

U_3Si_2 hardness varies depending upon the sample. When comparing the three pellet samples, the hardness is observed to trend with porosity. Pellet B is the most porous, and least dense pellet and shows the lowest value of hardness at 4411.78 ± 357.64. Similarly, the most

dense pellet, C, exhibits the greatest hardness at 6710.30 ± 723. 38; this suggests that a high frequency of pores increases the indention size in the sample.

The USC Toughness values use Young's Modulus of the Tile sample for all calculations across samples. The Taylor McMurtry Toughness value uses a density dependent elastic modulus value, which varies for each sample. In either case, the toughness data suggest that U_3Si_2's toughness is ~1 MPa √m. It was expected that toughness would vary with porosity, given that pores can relieve stress and reduce crack propagation. This is clear in the USC toughness data because Pellet B had the most pores and also has the largest toughness value. Similarly, the least porous samples, Pellet C and the Tile, have the lowest values of toughness. This trend with porosity is not observed in the data if a density dependent Young's Modulus value is used for each sample (Taylor McMurtry data).

Additional polarized light microscopy was performed on the U_3Si_2 in order to examine crack behavior through the surrounding microstructure in U_3Si_2. Grains have been outlined in white and arrows drawn to highlight regions of interest.

It was observed that cracks in U_3Si_2 do not travel along grain boundaries but rather traverse across grains. This implies that grain boundaries are not weak in this material. This behavior was observed in all samples as shown in Figures 5.55-5.58. Cracks travel through grain boundaries without changing direction. Additionally, the cracks do not change direction when moving through second phases. Griffith's crack theory says that a crack will propagate whenever it is easier to do that compared to forming a dislocation. In these U_3Si_2 samples, the surface energy from fracture is low in proportion to that required for creating a dislocation.

The ease with which U_3Si_2 cracks is a significant barrier to commercial scale up. Some samples sent to USC from INL fractured during shipment despite careful packaging. Fuel rods

must be shipped to location without suffering cracking or damage to pellet surfaces. It is possible that the current manufacturing process introduces a number of cracks within the fuel and that improvements to the fabrication process could reduce the fuel's propensity to crack and fracture. However, in its current state, U_3Si_2 appears extremely brittle and presents a handling nightmare in terms of commercial scale up.

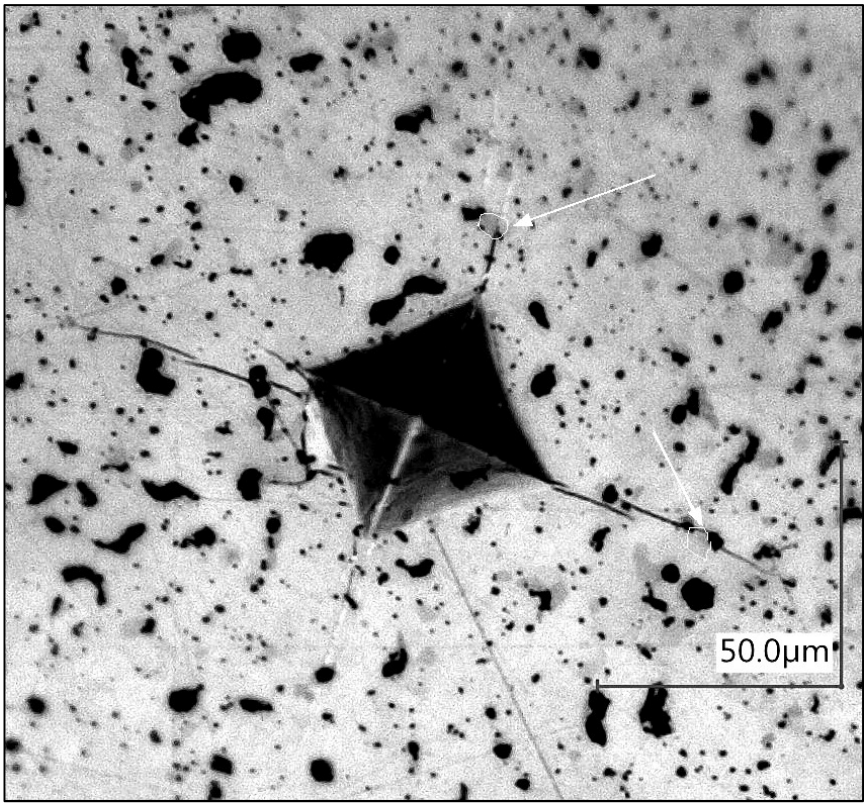

Figure 5.54: Polarized Light Image of Pellet A, indent #2
(9.8 N for 10 s)

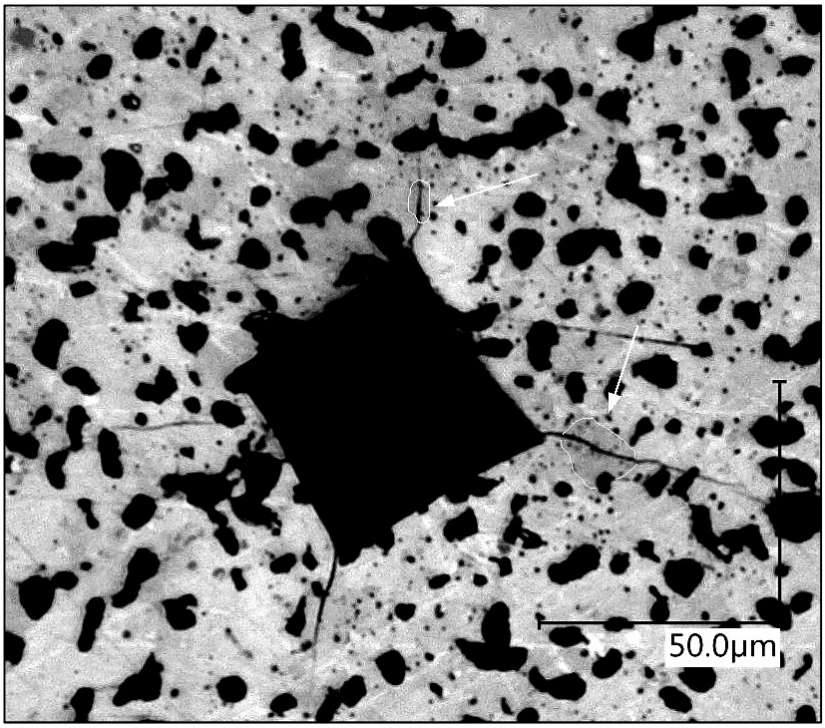

Figure 5.55: Polarized Light Image of Pellet B, indent #3
(9.8 N for 10 s)

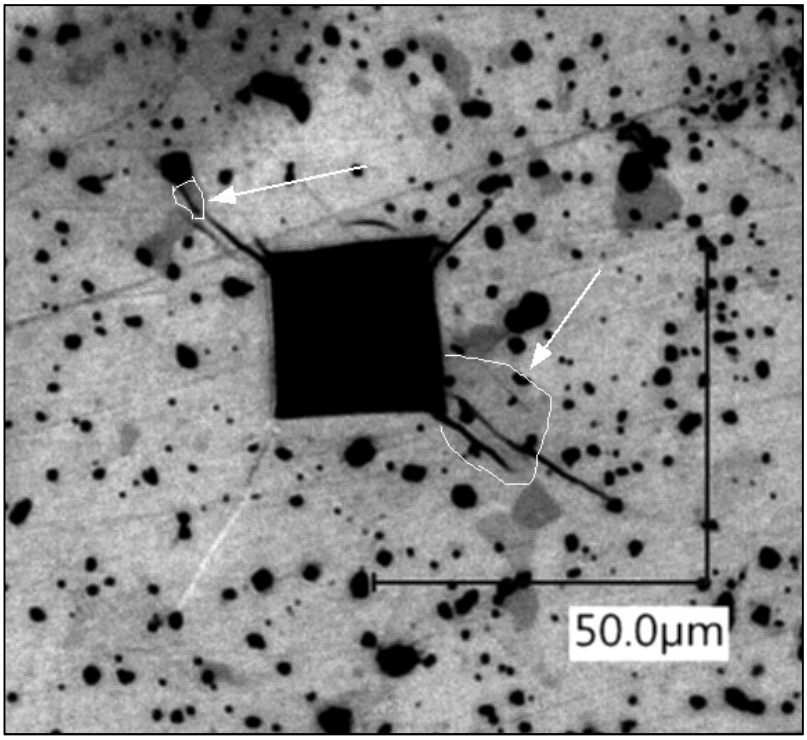

Figure 5.56: Polarized Light Image of Pellet C, indent #7
(4.9 N for 10 s)

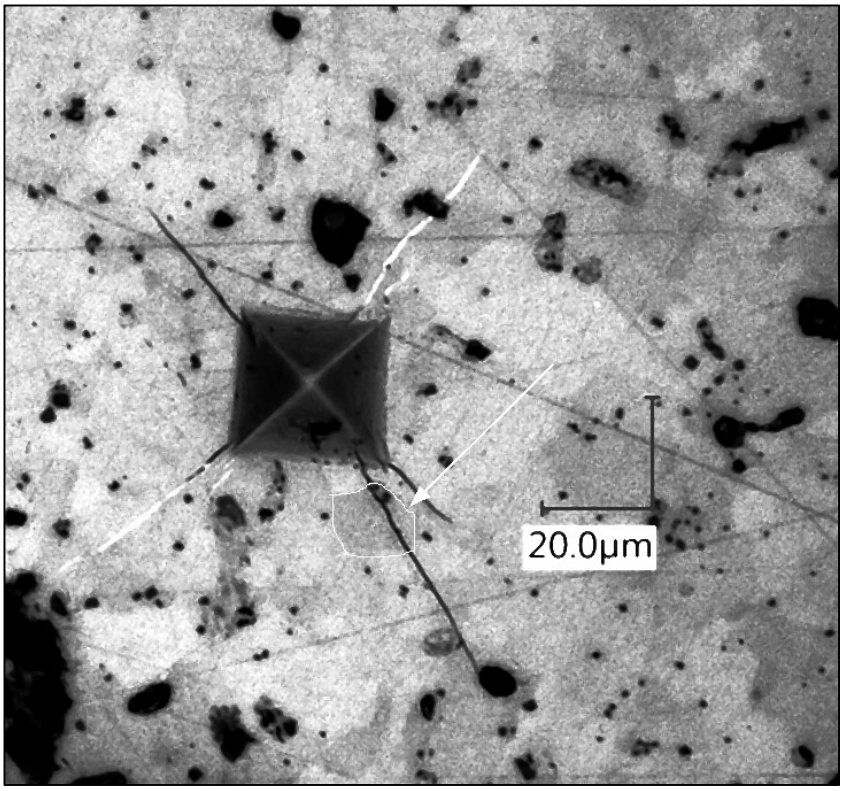

Figure 5.57: Polarized Light Image of Tile, indent #12 (2.9 N for 10 s)

5.9.3 EDX Compositional Analysis Around Indents:

During SEM imaging of indentations, EDX was performed on a few indents per sample. The purpose was to see if and how cracks propagated with second phases in U_3Si_2. While some interaction is noted, the EDX data is most useful in determining the occurrence and composition of second phases in the material.

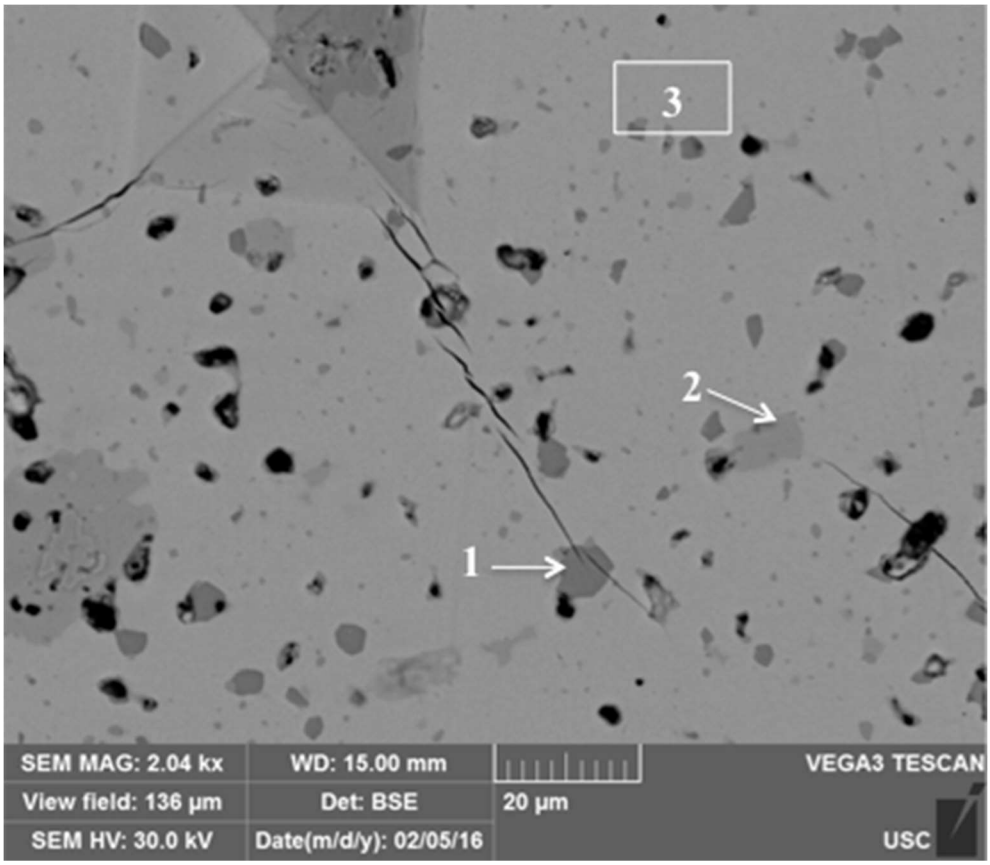

Figure 5.58: EDX was performed on 3 regions of Pellet A at Indent #1 (9.4 N, 10 s)

Table 5.45: EDX composition results for the three regions shown in Figure 5.58.

	Point 1	Point 2	Area 3
Wt % U	89.15	83.08	93.69
Wt % Si	10.84	16.92	6.31
Composition	USi	U_3Si_5	U_3Si_2

The background matrix material was identified as U_3Si_2. The precipitate at point 1 was identified as USi and the precipitate at point 2 was identified as U_3Si_5. U_3Si_5 has a higher melting point than U_3Si_2 so the effects of this second phase on the material are not necessarily negative. On the other hand, USi has a lower melting temperature than U_3Si_2 and is an undesirable second phase in the material. It appears as though the crack travels directly through the USi precipitate.

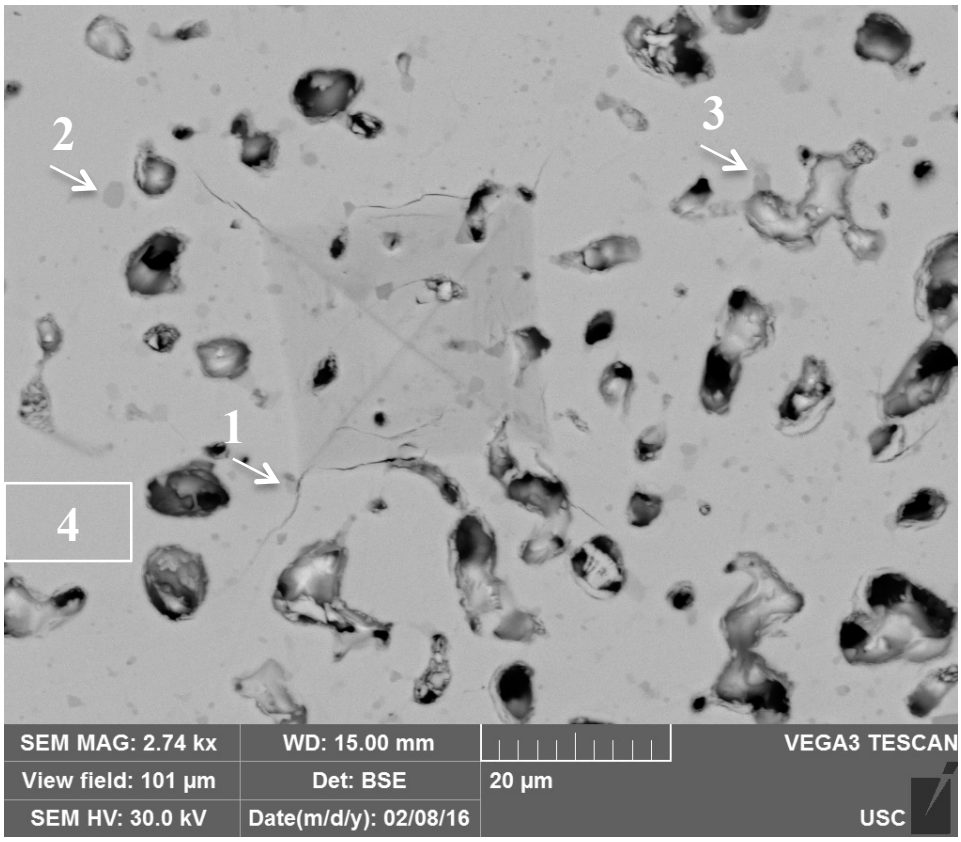

Figure 5.59: EDX was performed on 4 regions of Pellet B at Indent #10 (2.9 N for 10s)

Table 5.46: EDX composition results for the four regions shown in Figure 5.59.

	Point 1	Point 2	Point 3	Area 4
Wt % U	93.88	93.08	98.29	93.81
Wt % Si	6.12	6.92	1.71	6.19
Composition	U_3Si_2	U_3Si_2	U_3Si	U_3Si_2

The background matrix material in Pellet B was identified as U_3Si_2. The precipitates at point 1 and 2 were too small for identification and as a result the composition is that of the background U_3Si_2 matrix material. The precipitate at point 3 was identified as U_3Si. U_3Si has a substantially lower melting point than U_3Si_2 ($\Delta 735°$) and would cause damage to the pellet if it were present in reactor. Overall the precipitates in Pellet B are much smaller than those observed in Pellets A and C.

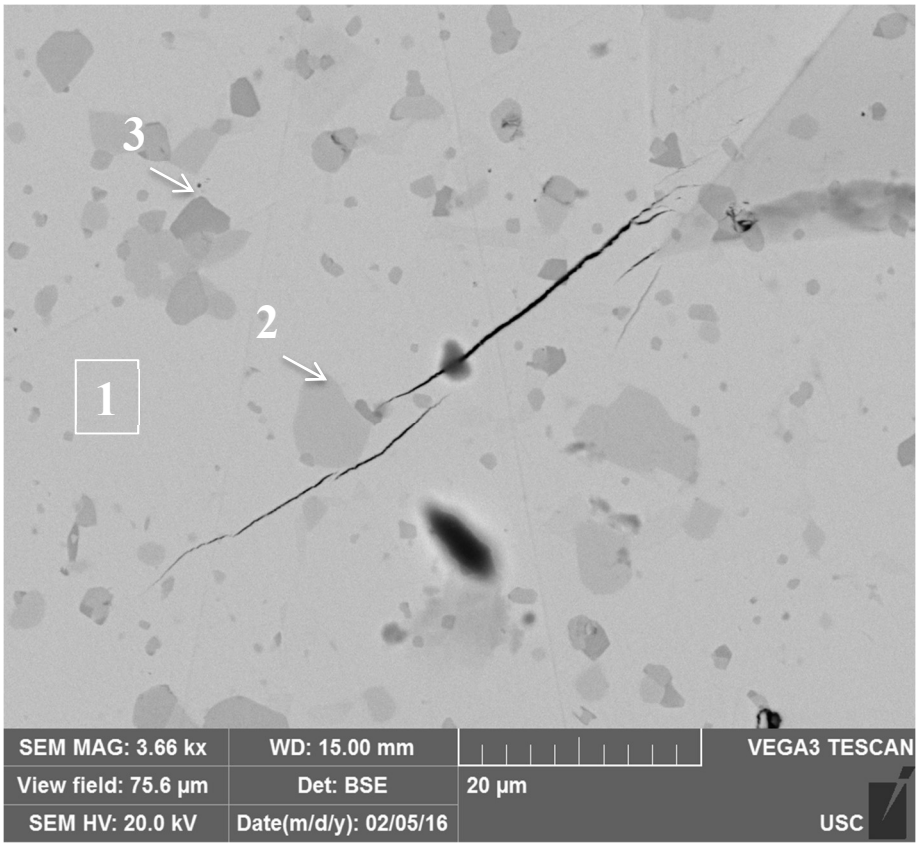

Figure 5.60: EDX was performed on 3 regions of Pellet C at Indent #1 (9.4 N for 10s)

Table 5.47: EDX composition results for the three regions shown in Figure 5.60.

	Area 1	Point 2	Point 3
Wt % U	92.45	90.08	87.06
Wt % Si	7.55	9.38	6.16
Wt % O	0	0.54	6.79
Composition	U_3Si2	USi	U-Si-O

Two precipitates were identified in Pellet C. The precipitate at point 2 has a composition very close to USi. This precipitate was also observed in Pellet A. The final precipitate at point 3 is close to USi but with the addition of oxygen in place of U and Si. UO_2 was identified in the pellets during the first round of SEM/EDX analysis. It is unlikely that these precipitates will be observed in future pellets because while Pellets A, B, and C were sintered in an Argon furnace with some oxygen present; subsequent samples have been sintered in a vacuum furnace.

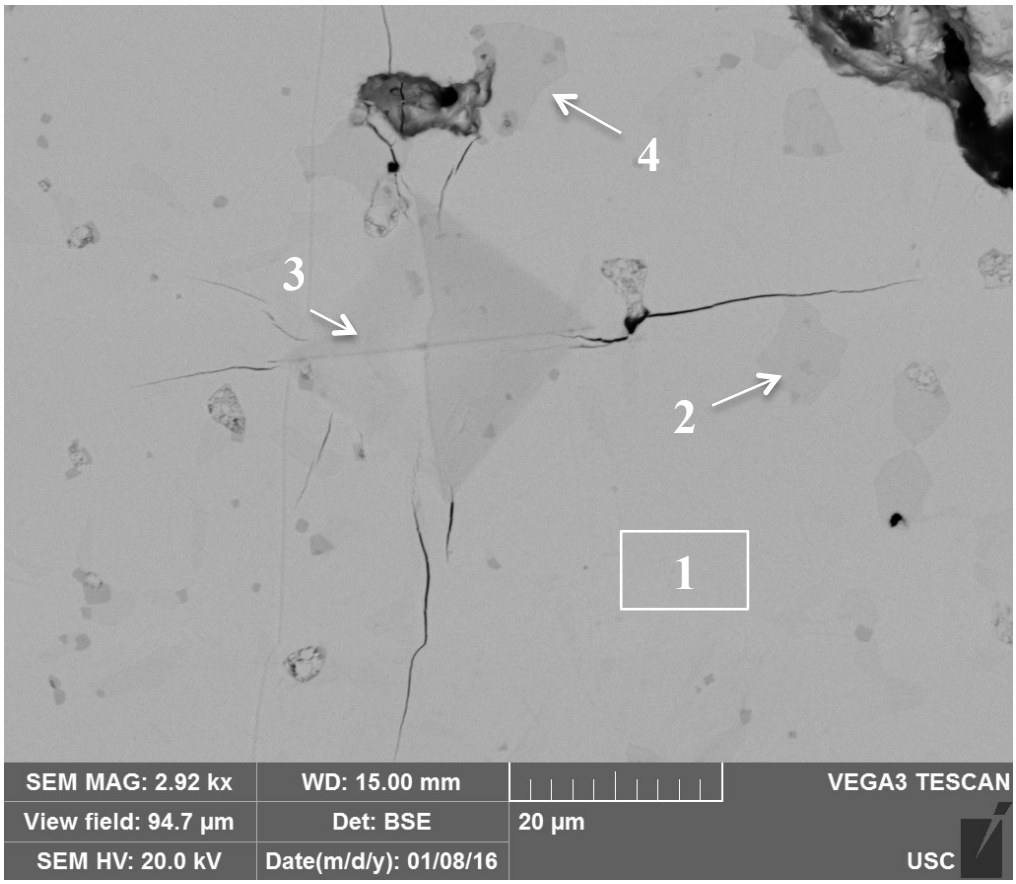

Figure 5.61: EDX was performed on 4 of the Tile Sample at Indent #10 (2,9 N for 10s)

Table 5.48: EDX composition results for the three regions shown in Figure 5.61.

	Area 1	Point 2	Point 3	Point 4
Wt % U	92.74	89.64	92.3	89.23
Wt % Si	7.26	10.36	7.7	10.77
Composition	U_3Si_2	USi	U_3Si_2	USi

Precipitates at point 2 and 4 were identified as USi. This phase was observed in all samples except Pellet B. The precipitates in the Tile sample are less round than those in Pellets A, B, and C. The rounded precipitates in Pellet C suggest that the second phases were molten during sintering. On the other hand, the lower sintering temperature used for the Tile (1400°C vs. 1500°C) produced precipitates with angular edges. No second phases with oxygen were

observed in the Tile sample. This is because the Tile sample was sintered in a vacuum furnace while Pellets A, B, and C were sintered in an Argon furnace with some O_2 present.

REFERENCES

ASTM E1876-09, Standard Test Method for Dynamic Young's Modulus, Shear Modulus, and Poisson's Ratio by Impulse Excitation of Vibration, ASTM International, West Conshohocken, PA, 2009, www.astm.org

Bauer. Reactor Materials, Volume 5, Number 1, Section 1 (page 1-24). February 1962.

Gale, W. & Totemeier T. Smithells metals reference book (Elsevier Butterworth-Heinemann, 2003).

Harp, J M, et al. Uranium silicide pellet fabrication by powder metallurgy for accident tolerant fuel evaluation and irradiation. Journal of Nuclear Materials. 466 (2015) 728-738.

Kurt, A., Hakan A., "Effect of porosity on thermal conductivity of powder metal materials", *Materials & Design*, 28, 230-233. (2007)

Li, XD, Bhushan B (1998) Thin solid Films 315:214.

Li, XD, Bhushan B (2001) Thin Solid Films 398:313.

Morrell, R., Kent, J. "The effect of test-piece chamfers on the determination of elastic moduli using the impact excitation method." National Physical Laboratory Report MAT 77. August 2015.

Munro, R.G. Material Properties of a α-sintered SiC. National Institute of Standards and Technology. 1997. http://www.nist.gov/srd/upload/jpcrd529.pdf

Quinn, G.D., Swab, J.J., 'Elastic modulus by resonance of rectangular prisms: corrections for edge treatments', *J. Amer. Ceram. Soc.*, 2000, 83 (2), 317-320, and US Army Report ARL-TN- 165, July 2000.

Shimizu, H. "The properties and irradiation behavior of U3Si2". Technical Report NAA-SR-10621, Atomics International (1965).

Smits, F. M. Measurement of Sheet Resistivities with the Four Point Probe. Bell System Technical Journal. May, 1958. 711-718.

Taylor, K.M. et al. Synthesis and Fabrication of Refractory Uranium Compounds. *Summary Report-May 1959 Through December 1960. February 1961.*

Taylor, K.M. et al. Synthesis and Fabrication of Refractory Uranium Compounds. *Monthly Progress Report No. 8 for April 1 through April 31, 1960*.

White, J.T., A. T. Nelson, J. T. Dunwoody, D. D. Byler, D. J. Safarik. K. J. McCllelan, "Thermophysical properties of U3Si2 to 1773 K,"Journal of Nuclear Materials, vol. 464, pp 275-280, 2015

Zachariasen, W.H. "Crystal Chemical Studies of the 5F-Series of Elements. VIII. Crystal Structure Studies of the Uranium Silicides and of $CeSi_2$, $NpSi_2$, and $PuSi_2$" Acta Cryst. , 2, 94 (1949).